NASA Technical Memorandum 104566, Vol. 19

SeaWiFS Technical Report Series

Stanford B. Hooker, Editor
NASA Goddard Space Flight Center
Greenbelt, Maryland

James G. Acker, Technical Editor
Hughes STX
Lanham, Maryland

Elaine R. Firestone, Technical Editor
General Sciences Corporation
Laurel, Maryland

Volume 19, Case Studies for SeaWiFS Calibration and Validation, Part 2

C.R. McClain, R.S. Fraser, and J.T. McLean
NASA Goddard Space Flight Center, Greenbelt, Maryland

M. Darzi, J.K. Firestone, F.S. Patt,
B.D. Schieber, R.H. Woodward, and E-n. Yeh
General Sciences Corporation, Laurel, Maryland

S. Mattoo
Applied Research Corporation, Landover, Maryland

S.F. Biggar, P.N. Slater, and K.J. Thome
University of Arizona, Tucson, Arizona

A.W. Holmes
Santa Barbara Research Center, Goleta, California

R.A. Barnes
ManTech Environmental Technology, Inc., Wallops Island, Virginia

K.J. Voss
University of Miami, Coral Gables, Florida

National Aeronautics and
Space Administration

Goddard Space Flight Center
Greenbelt, Maryland 20771

1994

Preface

The Calibration and Validation Program for the Sea-viewing Wide Field-of-view Sensor (SeaWiFS) instrument, as outlined in Volume 3 of the *SeaWiFS Technical Report Series* (McClain et al. 1992) encompasses four primary functions:

a) bio-optical algorithm development,

b) atmospheric correction algorithm development,

c) sensor calibration and characterization, and

d) product verification and quality control.

In the calibration and validation case studies volumes of the *SeaWiFS Technical Report Series*, investigations supported by the SeaWiFS Project that are related to these four categories are documented. Part 1, *Vol. 13*, provides an assortment of Coastal Zone Color Scanner (CZCS) algorithm comparisons and sensitivity analyses which serve as a basis for similar investigations and data processing requirements anticipated for SeaWiFS. Part 2, this volume, provides a more diverse suite of studies and includes contributions related to atmospheric correction methodologies, ancillary data sets required for level-2 processing of CZCS and SeaWiFS data, laboratory techniques for instrument calibration relevant to calibration round-robins, and field observations designed for transferring the prelaunch calibration to orbit and in interpreting the on-orbit lunar calibration data.

The data format chapter is included because the Calibration and Validation Program took the lead in the original format evaluation study. This study was very time consuming and outlines many of the important issues and criteria that must be considered in selecting a format. Ultimately, the Hierarchical Data Format (HDF) was selected in order to ensure compatibility with the Earth Observing System (EOS) and the EOS Project has provided much assistance to the SeaWiFS Project in the implementation of the HDF over the past two years. The Calibration and Validation Program has played a major role in the definition of SeaWiFS product and format specifications and in the development of the HDF input/output (I/O) routines for level-1 to level-3 calibration, browse and ancillary data products. These specifications and I/O routines will be published in a future volume of the *SeaWiFS Technical Report Series.*

Greenbelt, Maryland
May 1994

— C. R. McClain

Table of Contents

Prologue 1
1. Atmospheric and Glint Corrections 4
1.1 Introduction 4
1.2 Theory 4
1.3 Look-Up Tables 5
1.4 Validation 9
1.5 Discussion 20
2. Spectral Reflectance of the Moon 21
2.1 Introduction 21
2.2 Instrumentation 21
2.3 Data Acquisition 21
2.4 Results and Discussion 22
3. Preflight Solar-Based Calibration of SeaWiFS 25
3.1 Introduction 25
3.2 Concept 26
3.3 Method 26
3.4 Error Sources 29
3.5 Accuracy 30
3.6 Results 30
3.7 Conclusions 32
4. Spectral Radiance of the GSFC Integrating Sphere Using a Trap Detector 33
4.1 Introduction 33
4.2 Experiment Description 33
4.3 Conclusions 34
5. Evaluation of the Standard Data Formats HDF, netCDF, and CDF for SeaWiFS Operational Products 36
5.1 Introduction 36
5.2 Recommendations 37
5.3 Technical Considerations 37
5.4 Practical Considerations 40
6. The Generation of CZCS Ancillary Data Sets for Simulated SeaWiFS Processing 43
6.1 Introduction 43
6.2 Meteorological Data 43
6.3 Ozone Data Set 43
6.4 Data File Generation 43
7. The Generation of CZCS Near-Real Time Ancillary Data Files 47
7.1 Introduction 47
7.2 Meteorological Data 47
7.3 Ozone Data Set 47
7.4 Data File Generation 47

Table of Contents *cont.*

8. An Evaluation of Surface Wind Products for Use in SeaWiFS **50**
8.1 Introduction **50**
8.2 Data Sets **50**
8.3 Match Software **51**
8.4 Results **54**
GLOSSARY **65**
SYMBOLS **65**
REFERENCES **67**
THE SEAWIFS TECHNICAL REPORT SERIES **68**

ABSTRACT

This document provides brief reports, or case studies, on a number of investigations and data set development activities sponsored by the Calibration and Validation Team (CVT) within the Sea-viewing Wide Field-of-view Sensor (SeaWiFS) Project. Chapter 1 is a comparison the atmospheric correction of Coastal Zone Color Scanner (CZCS) data using two independent radiative transfer formulations. Chapter 2 is a study on lunar reflectance at the SeaWiFS wavelengths which was useful in establishing the SeaWiFS lunar gain. Chapter 3 reports the results of the first ground-based solar calibration of the SeaWiFS instrument. The experiment was repeated in the fall of 1993 after the instrument was modified to reduce stray light; the results from the second experiment will be provided in the next case studies volume. Chapter 4 is a laboratory experiment using trap detectors which may be useful tools in the calibration round-robin program. Chapter 5 is the original data format evaluation study conducted in 1992 which outlines the technical criteria used in considering three candidate formats, the Hierarchical Data Format (HDF), the Common Data Format (CDF) and the network CDF (netCDF). Chapter 6 summarizes the meteorological data sets accumulated during the first three years of CZCS operation which are being used for initial testing of the operational SeaWiFS algorithms and systems and would be used during a second global processing of the CZCS data set. Chapter 7 describes how near-real time surface meteorological and total ozone data required for the atmospheric correction algorithm will be retrieved and processed. Finally, Chapter 8 is a comparison of surface wind products from various operational meteorological centers and field observations. Surface winds are used in the atmospheric correction scheme to estimate glint and foam radiances.

Prologue

The purpose of the Sea-viewing Wide Field-of-view Sensor (SeaWiFS) Project is to obtain valid ocean color data of the world ocean for a five-year period, to process that data in conjunction with ancillary data to meaningful biological parameters, and to make that data readily available to researchers. The National Aeronautics and Space Administration's (NASA) Goddard Space Flight Center (GSFC) will develop a data processing and archiving system in conjunction with the Earth Observing System Data and Information System (EOSDIS), which includes a ground receiving system, and will oversee a calibration and validation effort to ensure the integrity of the final products.

The Calibration and Validation Team (CVT) has three main tasks: calibration of the SeaWiFS instrument; development and validation of the operational atmospheric correction algorithm; and development and validation of the derived product algorithms, such as chlorophyll *a* concentration. Some of this work will be done internally at GSFC while the remainder will be done externally at other institutions. NASA and the Project place the highest priority on assuring the accuracy of derived water-leaving radiances globally, and over the entire mission. If these criteria are met, development of global and regional biogeochemical algorithms can proceed on many fronts. These activities are discussed in detail in *The SeaWiFS Calibration and Validation Plan* (McClain et al. 1992a).

Because many of the studies and other works undertaken with the Calibration and Validation Program are not extensive enough to require dedicated volumes of the *SeaWiFS Technical Report Series*, the CVT has decided to publish volumes composed of brief, but topically specific, chapters. Volume 19 is the second in a set of such volumes. Volume 13 was the first, and consists primarily of contributions related to atmospheric correction methodologies, ancillary data sets required for level-2 processing of Coastal Zone Color Scanner (CZCS) and SeaWiFS data, laboratory techniques for instrument calibration relevant to calibration round-robins, and field observations designed for transferring the prelaunch calibration to orbit and in interpreting the on-orbit lunar calibration data. A short synopsis of each chapter is given below.

1. Atmospheric and Glint Corrections

This chapter explains an algorithm for correcting satellite measurements of ocean color for atmospheric and surface reflection effects. The algorithm depends on taking the difference between measured and tabulated radiances for deriving water-leaving radiances. The tabulated radiances are related to the measured radiance where the water-leaving radiance is negligible (670 nm). The tabulated radiances are calculated for rough surface reflection, polarization of the scattered light, and multiple scattering. The accuracy of the tables is discussed. The method is validated by simulating the effects of various wind speeds that differ from the single wind speed for which the look-up table was calculated. Another validation exercise employs aerosol models that are different from the maritime aerosol model for which the table was computed. The derived water-leaving radiances are accurate enough to compute the chlorophyll concentration with an error of less than or equal to 15% for light wind speeds, and an urban atmosphere with an aerosol optical thickness of 0.2. The

accuracy was unacceptably poor for a model with aeolian dust. On the other hand, this algorithm and the CZCS operational algorithm produced values of chlorophyll concentration that agreed closely.

2. Spectral Reflectance of the Moon

This report details the results of a field trip to Mauna Loa, Hawaii, the objective of which was to obtain data on the spectral reflectance of a full moon. The end use of this data was to determine the relative levels of spectral reflectance for use by the SeaWiFS instrument during its in-flight calibration. For the moon to be a good calibration device, the reflectance of the lunar surface needs to be consistently predicted. The Mauna Loa measurements indicate: a) lunar reflectance varies with day, and thus perhaps with the lunar phase; and b) the lunar surface might exhibit a so-called *back gloss*, that is, an enhancement of the reflectance in the direction of the illumination. Because of the latter, the reflectance of the moon may change rapidly during the course of a measurement, and it may be better to make use of the moon as a calibration source when the moon is not full.

3. Preflight Solar-Based Calibration of SeaWiFS

A new method for performing a preflight calibration of an optical remote sensing instrument with an onboard solar diffuser calibration system is presented. The rationale, method, advantages, disadvantages, error sources, and expected accuracies are discussed. The method was applied to the SeaWiFS instrument, which is to be flown on the SeaStar satellite.

4. Spectral Radiance of the GSFC Integrating Sphere Using a Trap Detector

The GSFC 42 in (107 cm) diameter spherical integrator source is used to provide traceability in the optical *in situ* measurements made by different researchers who support the SeaWiFS program. The sphere's spectral radiance calibration is based on the irradiance standard lamp scale. The purpose of this study is to verify the radiance calibration of the sphere by using an absolute detector based scale which would be independent of the irradiance lamp scale. The experiment described herein shows that filtered absolute silicon photodetectors in a trap configuration can be used to verify the scale of spectral radiance of an integration sphere source.

5. Evaluation of the Standard Data Formats HDF, netCDF, and CDF for SeaWiFS Operational Products

Three standard data formats have been evaluated for possible use in archiving and distributing SeaWiFS operational products. The three formats are the Hierarchical Data Format (HDF), the network Common Data Format (netCDF), and the Common Data Format (CDF). Major technical criteria that were considered include machine independence, platforms supported, self description, subsampling, high-level specification language, and computer language interfaces. Practical considerations included acceptance by the scientific community, user support, cost, available tools, and availability of SeaWiFS related data and software. Although each format has certain strengths and deficiencies, CDF was found to hold significant overall advantages over the other two formats for SeaWiFS. Specific reasons and tradeoffs are discussed in this report which was submitted to the SeaWiFS Project in September 1992.

6. The Generation of CZCS Ancillary Data Sets for Simulated SeaWiFS Processing

The SeaWiFS development effort includes simulated data processing using CZCS data files for the three-year time period of November 1978 through December 1981. Ancillary meteorological data products of total ozone, and surface values of zonal and meridional wind speed, atmospheric pressure, and relative humidity will be used for producing simulated level-2 CZCS (derived ocean color) products as a test of the SeaWiFS processing system. These data files are provided from the GSFC Distributed Active Archive Center (DAAC) and Total Ozone Mapping Spectrometer (TOMS) Project archives and converted to the SeaWiFS data format for subsequent processing. The calibration and validation element has developed procedures and software to process the CZCS ancillary data in a manner that simulates the processing that will occur once SeaWiFS is operational. The data are stored as HDF files for each of the ancillary parameters. This chapter describes the methods used for the generation of ancillary files from the CZCS era for use in simulating the SeaWiFS Data Processing System (SDPS).

7. The Generation of SeaWiFS Near-Real Time Ancillary Data Files

In the SDPS, near-real time (NRT) ancillary data files will be used for producing level-2, i.e., derived ocean color, products. In addition to a data file for total column ozone, separate files will contain surface value data for: zonal and meridional wind speeds, atmospheric pressure, and relative humidity. These ancillary data files are obtained from several sources, with additional backup sources identified for each data type should the primary data source become unavailable. The ancillary data files will be an integral part of the SDPS. The Calibration and Validation element for SeaWiFS has developed procedures and software to acquire and format the NRT data. The ancillary parameters will be stored as HDF files. This chapter describes the methods used for the generation of NRT files.

8. An Evaluation of Surface Wind Products for Use in SeaWiFS

This study statistically compared remotely sensed and modelled surface wind speeds from several sources with

available ground truth, in order to provide a recommendation for which source to use in the SDPS. Model wind field sources included the US Navy Fleet Numerical Oceanography Center (FNOC), the European Center for Medium Range Weather Forecasts (ECMWF), and the National Meteorological Center (NMC). Remotely sensed wind speed fields came from the Department of Defense (DoD) Special Sensor for Microwave/Imaging (SSM/I), and ground truth sources included seven fixed moorings provided by the National Oceanic and Atmospheric Administration (NOAA) National Data Buoy Center (NDBC), and the Tropical Ocean-Global Atmosphere (TOGA) Thermal Array for the Ocean (TAO) Project. A temporal and spatial match between the large scale and *in situ* winds was completed, using input data for the period 1982–90. An additional matchup was run to compare mooring winds with 1,000 mb and boundary layer winds from NMC, for 1990. A suite of software applications for reading and merging the various data sets used in the analysis was developed as part of the Laboratory for Hydrospheric Processes' VAX SEAPAK package. Scatterplots comparing each of the large scale wind sources to the seven moorings were generated, using commercial personal computer (PC) software, and square of the correlation coefficient (R^2) values, slopes and number of points for each plot were noted. This analysis indicated that SSM/I had the highest R^2 values of any of the large scale wind fields. Since they are gridded products, NMC and FNOC are the suggested wind field sources, and mechanisms are in place to transfer them to GSFC automatically. The new versions of these models incorporate SSM/I data in their production.

Chapter 1

Atmospheric and Glint Corrections

ROBERT S. FRASER
Goddard Space Flight Center
Greenbelt, Maryland

SHANA MATTOO
Applied Research Corporation, Landover, Maryland

ABSTRACT

This document explains an algorithm for correcting satellite measurements of ocean color for atmospheric and surface reflection effects. The algorithm depends on taking the difference between measured and tabulated radiances for deriving water-leaving radiances. The tabulated radiances are related to the measured radiance where the water-leaving radiance is negligible (670 nm). The tabulated radiances are calculated for rough surface reflection, polarization of the scattered light, and multiple scattering. The accuracy of the tables is discussed. The method is validated by simulating the effects of various wind speeds that differ from the single wind speed for which the look-up table was calculated. Another validation exercise employs aerosol models that are different from the maritime aerosol model for which the table was computed. The derived water-leaving radiances are accurate enough to compute the chlorophyll concentration with an error of less than or equal to 15% for light wind speeds, and an urban atmosphere with an aerosol optical thickness of 0.2. The accuracy was unacceptably poor for a model with aeolian dust. On the other hand, this algorithm and the CZCS operational algorithm produced values of chlorophyll concentration that agreed closely.

1.1 INTRODUCTION

The current CZCS algorithm for making atmospheric corrections is not generally applied when the aerosol optical thickness exceeds 0.2, or when near the sun glint. The aerosol optical thickness frequently exceeds 0.2 off the east coasts of Asia and the United States due to either urban pollution, outflows of dust from desert regions in Asia and Africa, and smoke from biomass (forest) burning. Evans and Gordon (1994) eliminate regions of surface glint for estimates of chlorophyll concentration where L_g/F_0 is greater than 0.005. L_g is the radiance of the surface glint at a sea surface and F_0 is the solar spectral irradiance above the Earth's atmosphere. If the wind speed were $10\,\mathrm{m\,s^{-1}}$, for example, a region within 40° of the nadir would be excluded when the sun is at the zenith; and for a scan azimuth of 90° between vectors from a pixel to the sun and to the satellite, glint regions would be excluded until the solar zenith angle reached 40°.

C. McClain suggested developing an algorithm to overcome these difficulties. A method had been developed for making atmospheric corrections over land utilizing look-up tables (Fraser et al. 1992). Also, a radiative transfer code already existed for ocean-atmosphere models that accounted for rough surface reflection, an arbitrary atmosphere, degree of polarization of the light, and multiple scattering (Ahmad and Fraser 1982). In this report, the theory, the ocean-atmosphere model, and the formulation and use of the look-up tables are described. Simulations are made to derive the water-leaving radiance in the glint region, and when dust or urban aerosols are present. Finally, a comparison is made of water-leaving radiances and chlorophyll concentrations derived with the look-up tables and the CZCS algorithm.

1.2 THEORY

The radiance of the ocean-atmosphere system measured at a satellite (L_m) can be expressed as

$$\begin{aligned} L_m &= L_0(\lambda;\theta,\phi;\theta_0,\phi_0;\tau_a) \\ &\quad + L_{\mathrm{sfc}}(\lambda;\theta,\phi;\theta_0,\phi_0;v;\tau_a)t(\lambda;\theta;\tau_a) \\ &\quad + L_W(\lambda;\theta,\phi;\theta_0,\phi_0;W;\tau_a;C)t'(\lambda;\theta;\tau_a), \end{aligned} \tag{1}$$

where L_0 is the radiance of the atmosphere, if the radiance just above the sea surface were zero; L_{sfc} is the radiance of the light reflected from the surface; and L_W is the water-leaving radiance of light scattered from beneath the

surface and penetrating it. All four radiances are vectors representing the four Stokes parameters, in order to account for the polarization properties of the scattered light. L_W contains the information about the sea particles and absorbing species, e.g., chlorophyll and pigments; t and t' are the transmissions through the atmosphere of $L_{\rm sfc}$ and L_W, respectively. The independent parameters in (1) are defined as follows:

- λ wavelength,
- θ, ϕ polar and azimuth angles of the line-of-sight at a spacecraft,
- θ_0,ϕ_0 polar and azimuth angles of the direct sunlight,
- W surface wind speed,
- τ_a aerosol optical thickness, and
- C chlorophyll concentration.

It is convenient to express the measured radiance by

$$L_m = L_{sa} + t' L_W, \tag{2}$$

where L_{sa} is the sum of the first two terms on the right side of (1).

The water-leaving radiance is:

$$L_W = \frac{L_m - L_{sa}}{t'}. \tag{3}$$

A normalized water-leaving radiance, $L_{WN}(\lambda)$, is used in the algorithm and is defined by

$$\frac{L_{WN}(\lambda)}{F_0} = \frac{L_W}{F_d/(1-s\rho)} = \frac{L_W}{F'_d}, \tag{4}$$

and

$$F_d = t_0 F_0 \cos\theta_0, \tag{5}$$

where s is the reflectance of the atmosphere for isotropic radiance incident at its base; ρ is the average reflectance of the sea; F_d is the total flux incident on the surface if it did not reflect light; F_0 is the solar spectral irradiance at the top of the atmosphere; $F'_d = F_d/(1-s\rho)$; and t_0 is the sum of the direct and diffuse transmission of sunlight through the atmosphere. Note (4) is slightly different than the expression given by Gordon and Castaño (1987).

The water-leaving radiance (actually L_W divided by F_0) transmitted to the top of the atmosphere is given by rearranging the factors in (4) and multiplying by t/F_0:

$$\begin{aligned} \frac{tL_W}{F_0} &= \frac{L_{WN}(\lambda)}{F_0} \\ &= \frac{tF_d}{(1-s\rho)F_0}. \end{aligned} \tag{6}$$

Equation (6) is computed by the subroutine `CLWTAU`, where the equivalencies between the four variables in (4) and `CLWTAU` are as follows: $L_{WN}(\lambda)$ is represented by `CONLW`, t by `TVALUE`, F_d by `TFLUX`, and F_0 by `FFLUX`.

The radiance calculated for the look-up tables (LU), L_{LU}, has the same equation as L_{sa}; by comparing (1) and (2),

$$L_{LU} = L_{sa} = L_0 + tL_{\rm sfc}. \tag{7}$$

In (2), it may be assumed that the transmission t' is approximately equal to t with negligible error. The atmospheric correction depends on computing the radiation parameters in (7), and subtracting L_{LU} from the measured radiance, as in (4). L_{LU} is calculated as a Stokes vector, but only the scalar radiance is stored in the look-up tables: $L_{LU}(\lambda;\theta,\phi;\theta_0,\phi_0=0;W=6;\tau_a)$. The transmission $t(\lambda;\theta;\tau_a)$ is computed by a scalar radiative transfer code D, SPD (Dave 1972b).

1.3 LOOK-UP TABLES

The radiances in the look-up tables are computed for a fine mesh of angles $(\theta, \phi-\phi_0; \theta_0)$, a surface wind speed ($W$) equal to $6\,\mathrm{m\,s^{-1}}$, and 8 aerosol optical thicknesses. The radiative properties requiring correction are those for the atmospheric gas, aerosols, and surface reflection. The radiative properties of the atmospheric gases can be calculated accurately. The surface reflectance and aerosol properties are variable. The radiance due to them is either comparable, or larger, than the water-leaving radiance. The aerosol optical thicknesses for the four spectral bands of the CZCS are the only parameters that determine the correction to the measured radiance to estimate the water-leaving radiance.

The estimated aerosol optical thickness is generally not the actual value of the optical thickness. It accounts not only for the optical thickness (τ_a), but also for the surface reflection and the aerosol albedo of single scattering (ω_a) and the aerosol albedo of the scattering phase function ($p_a/4\pi$). To show how the optical thickness represents the aerosol optical properties, consider the equation for the radiance, L_a, caused by single scattering of direct sunlight from just the aerosols:

$$\frac{L_a}{F_0} = \frac{\omega_a p_a \tau_a}{4\pi\cos\theta}, \tag{8}$$

An aerosol optical thickness in the algorithm accounts for $\omega_a p_a/4\pi\tau_a$, plus other effects of surface reflection, and multiple scattering. The albedo of single scattering and scattering phase function are also unknown. Due to these factors, the choice of an accurate aerosol model is difficult, if not impossible, but the aerosol model chosen is not critical to the look-up table computation. For this reason, a maritime aerosol model is chosen, since it is believed that it would be most representative of prevailing aerosols.

1.3.1 Aerosol Model

Aerosol optical properties over the world ocean vary considerably. These properties mostly depend on the relative concentrations of continental, dust, and oceanic aerosols (Weller and Leiterer 1988). The model adopted here

is based on a generalized maritime aerosol model given by Jursa (1985). The size distribution is given by

$$\frac{d}{dr}N(r) = \sum_{i=1}^{2} \frac{N_i}{\ln(10) r \sigma_i \sqrt{2\pi}} e^{\frac{-1}{2\sigma_i^2}\left[\log r - \log r_i\right]^2} \quad (9)$$

where N is the total number density, N_i is the number density of either the first or second aerosol model, r_i is the geometric mean radii, and $\sigma_i^2 = \langle(\log r - \log r_i)^2\rangle$. Equation (9) in terms of natural logarithms becomes

$$\frac{d}{dr}N(r) = \sum_{i=1}^{2} \frac{N_i}{\ln(10) r \sigma_i \sqrt{2\pi}} e^{\frac{-1}{2\sigma_i^2}\left[\frac{\ln r - \ln r_i}{\ln(10)}\right]^2}. \quad (10)$$

The geometric mean radii and standard deviations are given for the two models in Table 1. The albedo of single scattering is 0.99 for a maritime aerosol in the spectral range $0.4 \leq l \leq 0.7$ μm (Jursa 1985).

Table 1. Log-normal maritime aerosol model (Jursa 1985).

Aerosol	N_i	r_i [μm]	σ_i Decadic	$\log_{10}(\sigma_i)$ Natural
Continental	0.99	0.03	0.35	0.8059
Oceanic	0.01	0.30	0.40	0.9210

The optical properties of this aerosol model are calculated with the Mie equations in scalar radiative transfer code *B*, SPB (Dave 1972b). The calculations are made separately for each log-normal size distribution. The extinction coefficient (β) and phase function for the combined distribution are combined additively. The extinction (or scattering) cross section is given by

$$N\beta = N_1\beta_1 + N_2\beta_2; \quad (11)$$

and the scattering phase function by

$$N\beta\rho = N_1\beta_1\rho_1 + N_2\beta_2\rho_2 \quad (12)$$

where $N = N_1 + N_2$. The extinction coefficient and radiance of scattered light (L_a) have an approximate power law dependence on wavelength where a and α are numerical values:

$$\beta = \beta_0\lambda^{-\alpha}, \quad (13)$$

and

$$L_a = L_{ao}\lambda^{-a}. \quad (14)$$

These model optical data can be compared with measured data. This maritime aerosol model has a very large number of accumulation mode particles ($N_1 = 0.99$) compared to the number of coarse particles (0.01). For this model, the extinction is nearly independent of wavelength ($\alpha = 0.19$). The measured values are somewhat larger: $0.7 < \alpha < 1.7$ (Hoppel et al. 1990). The measured and model wavelength dependence of the radiance can be compared at a scattering angle of 120°, which is in the range of measurement angles. The dependence of the radiance of light scattered by the model aerosol is somewhat smaller ($a = 0.3$) than the function derived from CZCS observations.

An aerosol model that almost satisfies these measured constraints has the relative number of accumulation mode particles ($N_1 = 0.998$ and $N = 1.00 = N_1 + N_2$). The aerosol albedo of single scattering for this new model (with an index of refraction expressed by $1.43 - 0.0035i$) is smaller, however, ($\omega_a = 0.93$) than that given by Jursa (1985). Even when $N_1 = 0.998$, the radiance of light scattered is dominated by the coarse particles, and is 1.4 to 2.7 times as strong as if the model contained only accumulation mode particles. Hence, the index of refraction should be adjusted to represent that of the coarse particles ($n = 1.38 - 0.001i$). Optical data are computed for the same aerosol model that has just been discussed, with the index of refraction $n = 1.38 - 0.001i$, and are given in Table 2.

Table 2. Optical data for the same bimodal maritime aerosol model that is specified in Table 1, except for a different number of particles in the two modes. The index of refraction $n = 1.38 - 0.001i$.

N_1	2	3	4	5	6	7	8
1.000	1.76	0.92	0.99	0.99	1.0	1.0	1.0
0.999	0.97	0.65	0.98	0.98	1.3	2.0	2.5
0.998	0.72	0.46	0.98	0.98	1.6	3.0	4.0
0.996	0.46	0.22	0.97	0.97	2.2	5.1	7.0
0.994	0.32	0.07	0.96	0.97	2.8	7.1	10.0
0.992	0.24	−0.04	0.96	0.97	3.4	9.1	13.0
0.990	0.18	−0.11	0.96	0.97	4.1	11.2	16.0

The number of particles in the accumulation mode, N_1, is given in column 1. The number in the coarse particle mode, N_2, is equal to $1 - N_1$. Columns 2 and 3 give the wavelength dependence of extinction and radiance at a scattering angle of 120°, (α and a), respectively. Columns 4 and 5 give the aerosol albedo of single scattering for $\lambda = 441$ and 670 nm, respectively. Columns 6, 7, and 8 give the ratio of radiance to that of just the accumulation mode alone, for scattering angles of 120°, 160°, and 180°, but only for $\lambda = 670$ nm. An aerosol model in Table 2 that almost satisfies the measured constraints has the relative number of accumulation mode particles $N_1 = 0.998$, and $n = 1.38 - 0.001i$.

The wavelength dependence of the extinction and radiance at a scattering angle of 120° is 0.7 and 0.5, respectively, which is close to measured values. The aerosol albedo of single scattering ($\omega_a = 0.98$, columns 4 and 5) is the same as that given by Jursa (1985). If $N_1 = 0.998$, the radiance of light scattered is dominated by the coarse particles. Columns 6, 7, and 8 of Table 2 show that the

radiance scattered by this model is 1.6–4.0 times as strong as if this model contained only accumulation mode particles. The aerosol model in Table 2 with $N_1 = 0.998$ and $n = 1.38 - 0.001i$ is used to construct the look-up tables.

1.3.2 Gaseous Optical Properties

The optical thickness due to scattering by the standard molecular atmosphere (τ_r) and for a surface pressure of 1,013 mb is given in Table 3. The optical thickness refers to attenuation expressed in terms of base e rather than base 10. The Rayleigh scattering phase matrix is used for computing the molecular scattering.

Table 3. The scattering optical thickness, τ_r, of the standard atmospheric gases and absorption optical thickness of water vapor, τ_{wv} (Kneizys et al. 1983).

λ [nm]	τ_r	τ_{wv}
443	0.2394	0.000
520	0.1240	0.000
550	0.0986	0.000
670	0.0442	0.0043

The optical thickness of ozone, τ_{oz}, is defined as

$$\tau_{oz}(\lambda) = \delta(\lambda)\Omega, \tag{15}$$

where δ is the absorption coefficient and the amount of ozone, Ω, is given in Dobson units (DU). The optical thickness for an average amount of ozone (313 DU) is given in Table 4.

Table 4. Ozone optical thickness for an average amount of ozone (313 DU).

λ [nm]	α	Source	Average τ_{oz}
443	3×10^{-6}	1	0.00094
520	51×10^{-6}	2	0.016
550	85×10^{-6}	2	0.027
670	46×10^{-6}	2	0.014

Source 1: Inn and Tanaka (1953).
Source 2: Griggs (1968).

1.3.3 Surface Reflection

The sea surface is assumed to be rough. The probability distribution of surface slopes is given by Cox and Munk (1955). The radiative transfer code is described by Ahmad and Fraser (1982). This code accounted for the polarization characteristics of light reflected from the surface and scattered by the atmosphere, plus multiple scattering. The water-leaving radiance (L_W) is assumed to be isotropic and unpolarized. The radiances outside of the glint pattern computed by this algorithm, and SPD, developed by Dave (1972b), generally agree within 1%.

The index of refraction of sea water is less than 0.01 greater than that of pure water (Jerlov 1976). Because the reflection coefficient of sea water exceeds that of pure water by only 0.004, the index of refraction of pure water ($n = 1.331 - 1.1 \times 10^{-8}i$) is used in the computations of the look-up tables.

1.3.4 Computations

The tables are computed for the following values of the independent variables:

- λ 443, 520, 550, 670 nm;
- θ 0–84° in 6° increments;
- ϕ 0–180° in 4° increments (ϕ is measured from the direction of the solar beam and the radiances are symmetric with respect to principal plane through the sun);
- θ_0 0–66° in 6° increments;
- ϕ_0 0°;
- W 6 m s^{-1}; and
- τ_a 0–0.7 in increments of 0.01 for $\lambda = 443$ nm.

A model computation is made for each combination of the 4 wavelengths, 12 solar zenith angles, and 8 aerosol optical thicknesses, for a total of 384 models. As a result, 265,000 numerical values are stored in the look-up tables.

1.3.4.1 Interpolations

The ultimate accuracy required for CZCS atmospheric corrections is limited by the digitization of the radiance voltages. The radiances, L, are digitized to 8 bits. The radiances per count for the lowest and highest gains are given in the next to last column of Table 5. The reflectance per count is given in the last column. [The reflectance equals L/F_0, where F_0 is the solar spectral irradiance when the distance between the Earth and sun is 1 astronomical unit (AU).] The error in the look-up table radiances is 1%, which at saturation is $0.01 \times 255 = 3$ counts. If the radiances are only one-third of the saturation values, then the look-up table error is only 1 count. The goal is to make the error in the atmospheric corrections less than 1 count.

1.3.4.2 Radiance Gradients

Additional errors occur because of interpolations in the look-up tables. In order to match the measured and look-up table radiances, the measured radiance has to be interpolated for 4 parameters: the look-up radiance and three geometry parameters, i.e., the solar and observation zenith angles and the azimuth difference ($\phi - \phi_0$). The largest interpolation errors are sought in the tests made here. These are expected to occur where the magnitude of the radiance gradient is largest or nonlinear. Since the radiance, as a function of aerosol optical thickness, is nearly linear for each of the CZCS channels, the largest nonlinear radiance gradients occur near the horizon and near the glint pattern.

In order to determine the maximum radiance gradients, they are computed with the RADMAIN2 code, which accounts for rough ocean reflection. The approximate CZCS

Table 5. CZCS saturation radiances, radiance increment per count, and reflectance increment per count. The radiances are digitized to 8 bits. The irradiance units are $\mathrm{mW\,cm^{-2}\,\mu m^{-1}}$ and the radiance units are $\mathrm{mW\,cm^{-2}\,\mu m^{-1}\,sr^{-1}}$. Data are taken from Hovis et al. (1980).

Wavelength [nm]	Solar Irradiance (F_0)	Gain	Saturation Radiance ($L_{\max}$)	Radiance per Count	Reflectance per Count ($\frac{L}{F_0}$/ count)
443	187.0	3	5.41	0.021	1.1×10^{-4}
443	187.0	0	11.46	0.045	2.4×10^{-4}
520	187.0	3	3.50	0.014	0.7×10^{-4}
520	187.0	0	7.64	0.030	1.6×10^{-4}
550	186.8	3	2.86	0.011	0.6×10^{-4}
550	186.8	0	6.21	0.024	1.3×10^{-4}
670	153.1	3	1.34	0.005	0.4×10^{-4}
670	153.1	0	2.88	0.011	0.7×10^{-4}

geometry is used. Its scan through the nadir occurs between azimuths of 80° and 100° from the principal plane through the sun for most of the CZCS orbit; the exact azimuth is not important, since the radiance gradients are similar for nearby azimuths. It is assumed that useful measurements can be made only when the zenith angle of the radiance is less than 60°. At still larger zenith angles, the atmospheric correction rapidly increases and becomes less accurate. Also, the horizontal extent of the instantaneous field-of-view (IFOV) becomes larger, increasing the probability of clouds being present.

The maximum radiance gradients occur when scanning through the ocean glint and near the horizon. The maximum glint encountered by the CZCS scans occurred when the solar zenith angle was near 20°. The reflectance gradient, with respect to viewing nadir angle, is computed for channel one (443 nm) and is given in Table 6.

Table 6. Reflectance gradients with respect to the zenith angle at the top of the atmosphere for a rough ocean surface, where $W = 6\,\mathrm{m\,s^{-1}}$; aerosol optical thickness $\tau_a = 0.2$; $\lambda = 443\,\mathrm{nm}$; solar zenith angle equals 18°; azimuth from the principal plane is $\phi = 80°$; and the gain is 0.

θ	L/F_0 ($\phi = 80°$)	θ	$\frac{d}{d\theta}\left(\frac{L}{F_0}\right)$ ($\phi = 80°$)	Counts per Deg.
0	0.046	3	-3.3×10^{-5}	−0.1
6	0.046	9	-3.0×10^{-4}	−1.3
12	0.044	15	-4.5×10^{-4}	−1.9
18	0.041	21	-4.7×10^{-4}	−1.9
24	0.038	27	-3.7×10^{-4}	−1.5
30	0.036	33	-1.8×10^{-4}	−0.8
36	0.035	39	0.0	0.0
42	0.035	45	2.0×10^{-4}	0.8
48	0.036	51	3.7×10^{-4}	1.5
54	0.038	57	6.0×10^{-4}	2.5
60	0.042	63	8.6×10^{-4}	3.6
66	0.047	69	1.2×10^{-3}	5.1
72	0.054			

If the observation zenith angle θ is less than 60°, then the absolute gradient of reflectance is less than 0.0006 per degree, or 2.5 counts per degree. In order for the atmospheric correction error to be less than 1 count, the CZCS scan angle would have to be specified to tenths of a degree.

The reflectance gradient with respect to azimuth is given in Table 7. The maximum absolute gradient is less than 0.00015 per degree, or 0.2 counts per degree. The azimuth gradients are very weak. The reflectance gradients are similar for the other CZCS wavelengths.

Table 7. Reflectance gradients with respect to azimuth for the same conditions as for Table 6.

θ	L/F_0 ($\phi = 80°$)	L/F_0 ($\phi = 84°$)	$\frac{d}{d\phi}\left(\frac{L}{F_0}\right)$ ($\phi = 82°$)	Counts per Deg.
0	0.046	0.046	0.0	0.00
6	0.046	0.045	-1.0×10^{-4}	−0.06
12	0.044	0.043	-1.5×10^{-4}	−0.09
18	0.041	0.041	-1.5×10^{-4}	−0.09

1.3.4.3 Interpolation Errors

To find the atmospheric correction, a one-dimensional cubic spline is used to interpolate for the radiance, first for the azimuth between a vector from the sun to a pixel, and a vector from the pixel to CZCS, second for the zenith angle of that vector (θ), third for the zenith angle of the sun (θ_0), and finally for the total radiance. A severe test is made with $\lambda = 443\,\mathrm{nm}$ and a model with a large aerosol optical thickness ($\tau_a = 0.65$) and a large solar zenith angle (56°). The interpolations are made for four variables:

- the observation azimuth angle is 82°;
- the zenith angles of the line-of-sight are 4, 16, 28, 40, 52, and 64°;
- the sun zenith angle is (56°); and
- the aerosol optical thickness is 0.65.

The simulated look-up tables are computed for τ_a equals 0.6 and 0.7; θ_0 equals 54, 60, and 66°; θ from 0–90° in 6°increments; and ϕ from 0–180° in 4° increments. The

interpolation errors for radiance at the top of an atmosphere are given in Table 8, columns 7 and 8. The errors are only a fraction of a count, even for a large scan angle where the radiances approach the saturation value of 0.06.

Radiances emerging from the base of the model atmosphere, where the gradients are strong in the aureole, are given in Table 9 for another test of the interpolation accuracy. The errors are less than one count. The interpolation errors are also small for an azimuth of 78°.

Interpolation errors for a model with a smaller optical thickness where the reflectance gradients are different, are given in Table 10. The interpolation errors are negligible, as are the errors for the downward reflectance at the base of the atmosphere (not shown).

The interpolated reflectances at the top of the atmosphere are less than 0.3% or 0.3 counts, when the aerosol optical thickness is still smaller ($\tau_a = 0.05$) and also for a smaller solar zenith angle (θ_0=20°). The errors increase to 2 counts for the downward reflectances at the base of the atmosphere (Table 11), because the interpolation is infringing on the bright aureole where the reflectance gradients are larger. Also, the θ_0 interval was mistakenly made twice as large, namely 12°.

All the tests made for interpolation of the upward reflectance at the top of the atmosphere show errors less than 1 count in Tables 6 and 7, where the mesh size of θ and θ_0 is 6°, for the azimuth 4°, and aerosol optical thickness is varied in increments of 0.1 from 0.0 to 0.7. The tests attain 2 counts of error for the downward reflectance at the base of the atmosphere near the bright aureole region (Table 11) where the reflectance gradients are stronger. Hence, the interpolation errors for the reflectances at the top of the atmosphere may attain errors of a few counts where the reflectance gradients are strong in the solar glint region. A method does not exist for making such interpolation tests without using hours of computer time.

1.3.4.4 Application of Look-Up Tables

The look-up tables that are described for deriving the water-leaving radiance are based on some of the procedures developed for the operational CZCS algorithm. The variable reflectance from the ocean and atmosphere is parameterized by only the aerosol optical thickness. The flow chart (Fig. 1) indicates that a clear, cloud-free region with chlorophyll concentration less than 0.25 mg m^{-3} is selected for pixels where the water-leaving radiance is assumed for the three longest wavelengths. The radiation parameters in the table are interpolated with a one-dimensional spline algorithm for the geometrical independent variables, which are the solar zenith angle, the solar azimuth, the view nadir angle, and the view azimuth.

The aerosol optical thickness for each of the three longest wavelengths (520, 550, and 670 nm) is chosen where the look-up table radiance (L/F_0) matches the measured radiance. These optical thicknesses are assumed to be proportional to the wavelength raised to a power; the logarithm of the optical thickness, as a function of the logarithm of the wavelength, is extrapolated to the shortest wavelength (443 nm). A gamma function for each of the three shortest wavelengths is computed as the ratio of the corresponding optical thickness to the optical thickness at 670 nm:

$$\gamma(\lambda) = \frac{\tau_a(\lambda)}{\tau_a(670)}. \tag{16}$$

This gamma function is applied elsewhere in an image until a new gamma function can be computed. At other pixels, the aerosol optical thickness at 670 nm is computed by assuming the water-leaving radiance, $L_W(670)$, equals zero.

The optical thickness at 670 nm is derived, whereas, the optical thicknesses at the three shorter wavelengths are computed from the gamma function. The optical thicknesses specify the ocean-atmosphere model and the corresponding look-up table radiances for comparison with the measured radiances, to obtain the water-leaving radiances for the three shortest wavelengths (3). Finally, the chlorophyll concentration is computed by means of the following equation (Gordon et al. 1983):

$$C = 1.053\left[\frac{L_W(550)}{L_W(443)}\right]^{1.71} \tag{17}$$

1.4 VALIDATION

The algorithm is tested for accuracy in deriving L_W/F_0 and chlorophyll concentration by simulating the radiances of sunlight scattered from the ocean-atmosphere system. The simulations account for foam. The look-up tables for the surface radiance accounts only for the Cox-Munk reflection (Cox and Munk 1955) from a rough sea surface:

$$\mathbb{L}_{\text{sfc}}(\theta,\phi) = \int_0^{2\pi}\int_0^{\frac{\pi}{2}} \mathbb{R}(\theta,\phi;\theta',\phi')\,\mathbb{L}_d(\theta',\phi')\sin\theta' d\theta' d\phi' \tag{18}$$

where $\mathbb{R}$ is the reflection matrix†, $\mathbb{L}_{\text{sfc}}$ and $\mathbb{L}_d$ are columnar matrices of the four Stokes parameters, and $\mathbb{L}_d$ is the radiance of light incident on the surface. In the simulations, the upward radiance ($\mathbb{L}_u$) just above the surface is modified to account for foam reflection and underwater light:

$$\mathbb{L}_{up} = (1-f)\mathbb{L}_{\text{sfc}} + \frac{1}{\pi} f A_f \mathbb{F}'_d + (1-fA_f)\mathbb{L}_w, \tag{19}$$

where f is the fraction of the surface covered by foam; $(1-f)\mathbb{L}_{\text{sfc}}$ is the matrix of the radiance of light reflected from a rough surface, but minus the coverage by foam; A_f is the foam reflectance; $\mathbb{F}'_d$ is the total downward flux; and $(1-f)\mathbb{L}_w$ is the water-leaving radiance. Both $\mathbb{L}_w$

† $\mathbb{R}$, $\mathbb{L}$, and $\mathbb{F}$ designate matrices; more detailed variable definitions appear in the SYMBOLS list at the end of this document.

Table 8. Interpolation accuracy for upward radiance (L/F_0) at the top of an atmosphere with no surface reflection, where $\lambda = 443$ nm.

τ_a	θ_0	θ	ϕ	Interpolated L/F_0	Validation L/F_0	Percent Error	Error in Counts
0.65	56	4	82	0.0267	0.0266	0.1	0.1
0.65	56	16	82	0.0273	0.0278	0.0	0.0
0.65	56	28	82	0.0294	0.0294	0.0	0.0
0.65	56	40	82	0.0335	0.0335	0.0	0.0
0.65	56	52	82	0.0406	0.0406	0.0	−0.1
0.65	56	64	82	0.0526	0.0526	−0.1	−0.2

Table 9. Errors for downward L/F_0 at the base of the atmosphere.

τ_a	θ_0	θ	ϕ	Interpolated L/F_0	Validation L/F_0	Percent Error	Error in Counts
0.65	56	4	82	0.0446	0.0444	0.4	0.7
0.65	56	16	82	0.0463	0.0463	0.2	0.3
0.65	56	28	82	0.0484	0.0484	0.1	0.1
0.65	56	40	82	0.0511	0.0511	0.0	−0.1
0.65	56	52	82	0.0550	0.0551	−0.1	−0.2
0.65	56	64	82	0.0602	0.0603	−0.2	−0.4

Table 10. Same as Table 8 except that the aerosol optical thickness is reduced to 0.25.

τ_a	θ_0	θ	ϕ	Interpolated L/F_0	Validation L/F_0	Percent Error	Error in Counts
0.25	56	4	82	0.0216	0.0216	0.01	0.1
0.25	56	16	82	0.0220	0.0220	0.0	0.0
0.25	56	28	82	0.0233	0.0233	0.0	0.0
0.25	56	40	82	0.0260	0.0260	0.0	0.0
0.25	56	52	82	0.0312	0.0312	0.0	0.0
0.25	56	64	82	0.0408	0.0408	−0.1	−0.1

Table 11. The downward L/F_0 at the base of the atmosphere for the following parameters: $\lambda = 443$ nm; $\theta_0 = 14°$, 26°, 32°; $\theta = 0°$ to 90° in 6° increments; $\phi = 0°$ to 180° in 4° increments; and $\tau_a = 0.0, 0.1, 0.2$.

τ_a	θ_0	θ	ϕ	Interpolated L/F_0	Validation L/F_0	Percent Error	Error in Counts
0.05	20	4	82	0.0454	0.0448	1.1	2.1
0.05	20	10	82	0.0441	0.0439	0.4	0.8
0.05	20	16	82	0.0417	0.0419	−0.3	−0.6
0.05	20	22	82	0.0393	0.0395	−0.5	−0.9
0.05	20	28	82	0.0373	0.0375	−0.5	−0.8
0.05	20	34	82	0.0359	0.0361	−0.4	−0.6
0.05	20	40	82	0.0352	0.0354	−0.3	−0.5
0.05	20	46	82	0.0353	0.0354	−0.2	−0.4
0.05	20	52	82	0.0361	0.0362	−0.2	−0.3
0.05	20	64	82	0.0410	0.0411	−0.2	−0.3

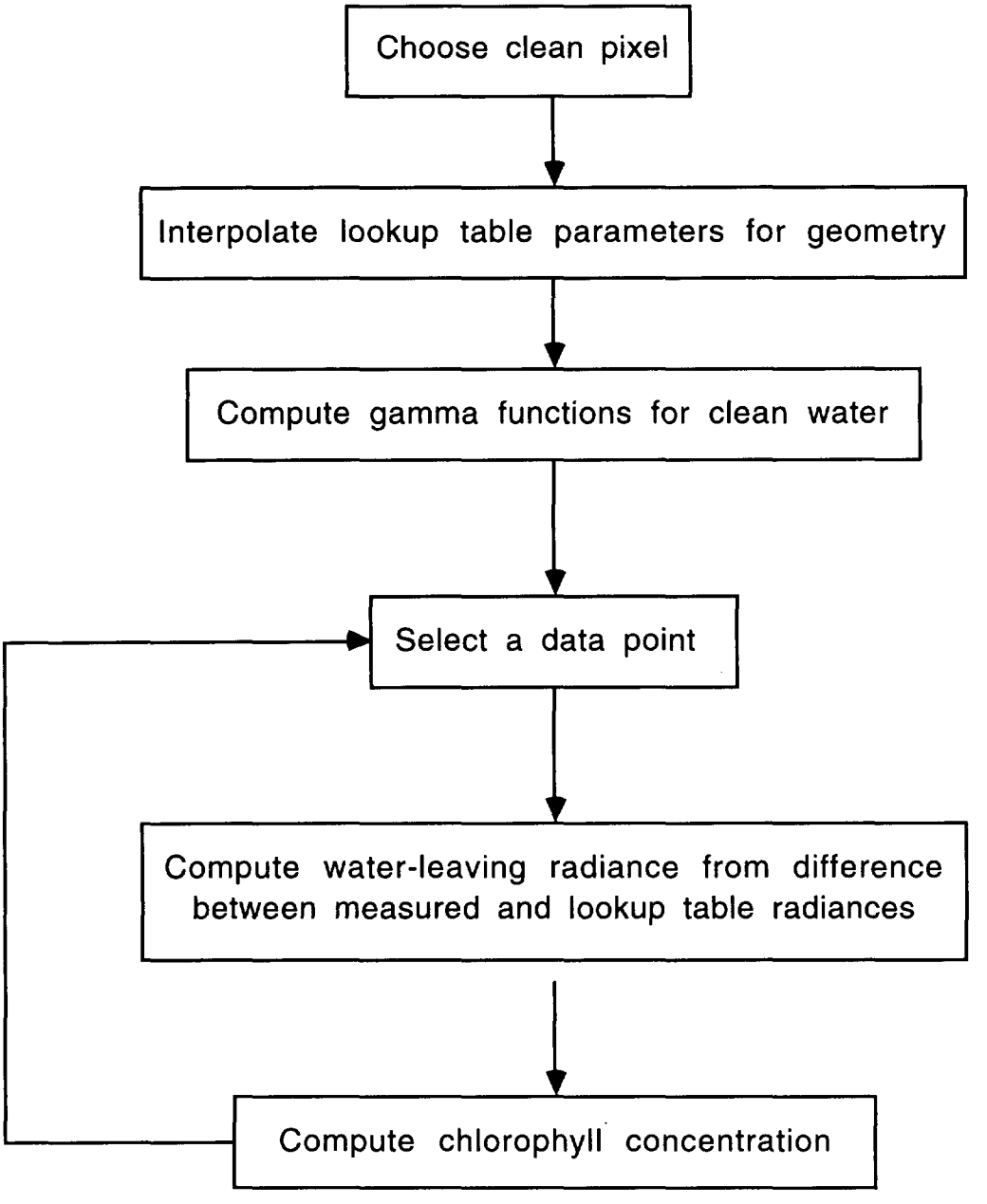

Fig. 1. Flow chart for making sun glint and atmospheric corrections to satellite measurements of ocean color.

and the foam reflectance are assumed to be isotropic and unpolarized.

All radiances and fluxes are normalized to $\mathbb{F}_0$ ($\mathbb{L}_{\rm up}$, $\mathbb{L}_d$, $\mathbb{F}_d$, and $\mathbb{L}_w$.) The RADTRAN radiance parameters are modified as follows:

$$L_{\rm up,1} = \left[\frac{(1-f)L_{u,1} + \frac{fA_f F_d'}{\pi} + (1-fA_f)L_W}{2}\right], \quad (20)$$

$$L_{\rm up,2} = \left[\frac{(1-f)L_{u,2} + \frac{fA_f F_d'}{\pi} + (1-fA_f)L_W}{2}\right], \quad (21)$$

$$L_{\rm up,3} = \left[(1-f)L_{u,3}\right], \quad (22)$$

and

$$L_{\rm up,4} = \left[(1-f)L_{u,4}\right]. \quad (23)$$

The fractional coverage by foam and its reflectance are given by Koepke (1985):

$$f = 2.95 \times 10^{-6}\, W^{3.52}, \quad (24)$$

where W is in units of $\mathrm{m\,s^{-1}}$, and A_f=0.22.

The simulations are made for moderate operational conditions. The algorithm is first tested with the same maritime aerosol used for calculating the look-up tables. Then the wind speed is increased from $6\,\mathrm{m\,s^{-1}}$ for the look-up tables to $10\,\mathrm{m\,s^{-1}}$ for a simulation. The simulations continue for an urban atmosphere that would appear off the US east coast, and Saharan dust off the west coast of Africa. Finally, a comparison is made of the chlorophyll concentrations derived with this algorithm and the CZCS operational algorithm by applying it to measured radiances.

1.4.1 Sea Glint

The effectiveness of the algorithm in retrieving water-leaving radiances is tested for a case where they are important but cannot be retrieved from CZCS measurements with the operational atmospheric correction algorithm because of sea glint. The strongest glint that can occur where useful ocean color data might be retrieved occurs at 30° N latitude (M. Darzi pers. comm.). On such occurrences, the solar zenith angle at a pixel is assumed to be 30°. The sensor tilt is 20°, but a somewhat more severe test will be made by neglecting the tilt, and by having the simulated scan pass through a brighter part of the glint pattern.

The accuracy of the derived water-leaving radiance in the presence of glint is computed first. The model atmosphere (maritime) and wind speed ($6\,\mathrm{m\,s^{-1}}$) for the simulation are the same as those used for the look-up tables. The surface reflectance in the simulation is modified slightly by adding foam to the water, whose radiance is only 0.0001. The aerosol optical thickness at 443 nm equals 0.2. A maritime atmosphere with large optical thickness will not be tested, since such conditions are not common.

The water-leaving radiances are those observed where the chlorophyll concentration equals $0.12\,\mathrm{mg\,m^{-3}}$ (Morel 1980). The values of the water-leaving radiances (L_W/F_0) are 0.00668, 0.00315, 0.00180, and 0.00000 for the respective wavelengths: 443, 520, 550, and 670 nm. No noise is added to the simulated radiances. The observation zenith angles range from 0–60° at an azimuth angle equal to 88°, which is nearly orthogonal to the principal plane through the sun. Interpolations are not made for the geometric variables, because a code is not available for simulating geometries that differ from those of the look-up tables. The derived water-leaving radiances are quite accurate, being within 2% of the simulated values. The assumption that the water-leaving radiance, $L_W(670)$, is negligible leads to errors in the derived water-leaving radiances at the shorter wavelengths. The look-up table itself can be used to estimate this error.

To simplify the notation, a reflectance, ρ, is defined as

$$\rho_i(\lambda) = \frac{L_i(\lambda)}{F_0(\lambda)}, \quad (25)$$

where i may represent any of the following:

- m for measured,
- LU for look-up table,
- 0 for light scattered by the atmosphere,
- sfc for reflection from the sea surface, and
- w for water-leaving radiance.

The measured and look-up table ρ_i are:

$$\rho_m = \rho_0 + t\rho_{\rm sfc} + t'\rho_w, \quad (26)$$

$$\rho_{LU} = \rho_0 + t\rho_{\rm sfc}, \quad (27)$$

$$\rho_w = \frac{\rho_m - \rho_{LU}}{t'}, \quad (28)$$

and

$$\Delta\rho_w(\lambda) = \frac{-\Delta\rho_{LU}(\lambda)}{t'}. \quad (29)$$

Assuming the only error in the algorithm derives from error in the water-leaving radiance (L_W) or in the reflectance (ρ_w) for the red channel, $\Delta L_W(670)$ or $\Delta\rho_w(670)$, respectively, then the error in the look-up radiance is

$$\Delta\rho_{LU}(670) = t'(670)\Delta\rho_w(670). \quad (30)$$

This error shall be traced to the water-leaving radiance errors at the shorter wavelengths.

The water-leaving radiance error causes errors in identifying the correction model by means of the aerosol optical thickness. The aerosol optical thickness after substitution of (30) is

$$\Delta\tau_a(\lambda) = \frac{\partial\tau_a(\lambda)}{\partial\rho_{LU}}\Delta\rho_{LU}(\lambda) = \frac{\partial\tau_a(\lambda)}{\partial\rho_{LU}}t'\Delta\rho_w(\lambda), \quad (31)$$

and after substitution of (16) is

$$\Delta\tau_a(\lambda) = \gamma(\lambda, 670)\frac{\partial\tau_a(670)}{\partial\rho_{LU}}t'\Delta\rho_w(670). \quad (32)$$

The error in the water-leaving radiance, (33), is found by substituting (32) in (29):

$$\begin{aligned}\Delta\rho_w(\lambda) &= \frac{-1}{t'}\frac{\partial\rho_{LU}(\lambda)}{\partial\tau_a}\Delta\tau_a(\lambda) \\ &= \frac{-1}{t'(\lambda)}\frac{\partial\rho_{LU}(\lambda)}{\partial\tau_a}\gamma(\lambda,670)\frac{\partial\tau_a(670)}{\partial\rho_{LU}}t'(670)\Delta\rho_w(670).\end{aligned} \tag{33}$$

The look-up table can be used to estimate the errors in the water-leaving radiances. Table 12 shows that for a modest water-leaving radiance error of $\Delta(L_W/F_0(670))$ equal to -0.00015, the error in the water-leaving radiances for the other wavelengths are acceptably small.

A simulation is made with the wind speed increased to $10\,\mathrm{m\,s^{-1}}$, but with the same maritime model atmosphere. Figure 2 compares the radiances at the top of the atmosphere for models with wind speeds of 6 and $10\,\mathrm{m\,s^{-1}}$. The higher wind speed causes the glint pattern to expand. The algorithm estimates nearly the correct aerosol optical thickness at nadir of 0.21 (443 nm), compared with a simulation value of 0.2. The derived water-leaving radiances (L_W) are compared with the simulated values of L_W = 0.00688, 0.00315, and 0.00180 for the respective wavelengths of 443, 520, and 550 nm. Figure 3 shows the deviation or error in digital counts.

The errors lie within the range of ± 2 counts for a nadir angle less than 45°. It is important that the errors are well correlated for the channels, since the chlorophyll concentration is computed by a ratio of the water-leaving radiances at 443 and 550 nm (17). The deviation in the estimated chlorophyll concentration from the model value of 0.12, lies within the range of $\pm 10\%$.

1.4.2 Urban Atmosphere

The westerly winds of middle latitudes carry continental and urban aerosols over the western Atlantic and Pacific Oceans. Representative physical characteristics of such an aerosol can be described by a log-normal size distribution with a geometric mean radius of 40 nm and a standard deviation of $\ln r = 0.69$. Their index of refraction is assumed to be $1.43 - 0.0035i$, which results in an albedo of single scattering of 0.98. This model with an aerosol optical thickness of 0.4 (443 nm), combined with surface winds of $10\,\mathrm{m\,s^{-1}}$, results in radiances saturating, even though the look-up optical thicknesses extend to 0.7. In this simulation, the wavelength dependence of the aerosol optical thickness is approximated by $\lambda^{-1.7}$. In contrast, for the maritime aerosol used to compute the look-up tables, the aerosol optical thickness is nearly independent of wavelength. Figure 4 shows that the radiances of the urban and maritime models of the look-up tables do not differ strongly. As a result, the error in the derived water-leaving radiances is less than one count.

Another simulation is considered using the same urban aerosol, but the wind speed is increased to $10\,\mathrm{m\,s^{-1}}$. Figure 5 shows that the total radiance of this model differs more strongly from that of the look-up tables than in the previous simulation with a wind speed of $6\,\mathrm{m\,s^{-1}}$. The water-leaving radiance error is rather large: ± 3 counts for nadir angles less than 42° (Fig. 6). Because of the strong correlation of the errors with respect to wavelength, the relative error in the chlorophyll concentration is within an acceptable range of $\pm 15\%$ when the nadir angle is less than 48° (Fig. 7). These errors are small enough to expect satisfactory estimates of chlorophyll concentration from CZCS measurements off of the eastern coasts of mid-latitude continents, assuming moderate amounts of haze and wind speed.

1.4.3 Aeolian Dust

The following simulation is made for a dust aerosol. The dust size distribution is log-normal with the standard deviation ($\ln r$) equals 0.875 and the geometric mean radius r_m equals $0.176\,\mu$m. The total aerosol optical thickness equals 0.5, and the optical properties of the dust aerosol are given in Table 13. The geometric conditions for the simulation set the solar zenith angle equal to 60°. The scattering angle varies between 100° and 120°, where the relative azimuth angle between the principal and scan planes equals 88°. The difference between the dust and look-up phase functions is small for scattering angles less than 145°, but the ratio of the dust to the look-up phase functions increases to 3 for a scattering angle equal to 180°. The surface wind speed equals $6\,\mathrm{m\,s^{-1}}$.

The simulation of the water-leaving radiance, L_W, is equal to zero in all spectral bands. Figure 8 shows the ratio of the derived water-leaving radiance to the total radiance. The errors are acceptably small for 520 and 550 nm, but not for the shortest wavelength. The reason for the large error is the moderate aerosol absorption at the shortest wavelength. Optical thicknesses derived for the three longest wavelengths, when extrapolated to a wavelength of 443 nm, overestimate the optical thickness at the shortest wavelength. As a consequence, the look-up table radiance is too large—even larger than the simulated measured radiance. This algorithm, as it stands, fails for this particular aerosol model. This problem for dust may possibly be overcome by using a separate look-up table computed for dust.

1.4.4 Comparison with CZCS Algorithm

In order to gain additional confidence in the algorithm, values of water-leaving radiances are compared with values

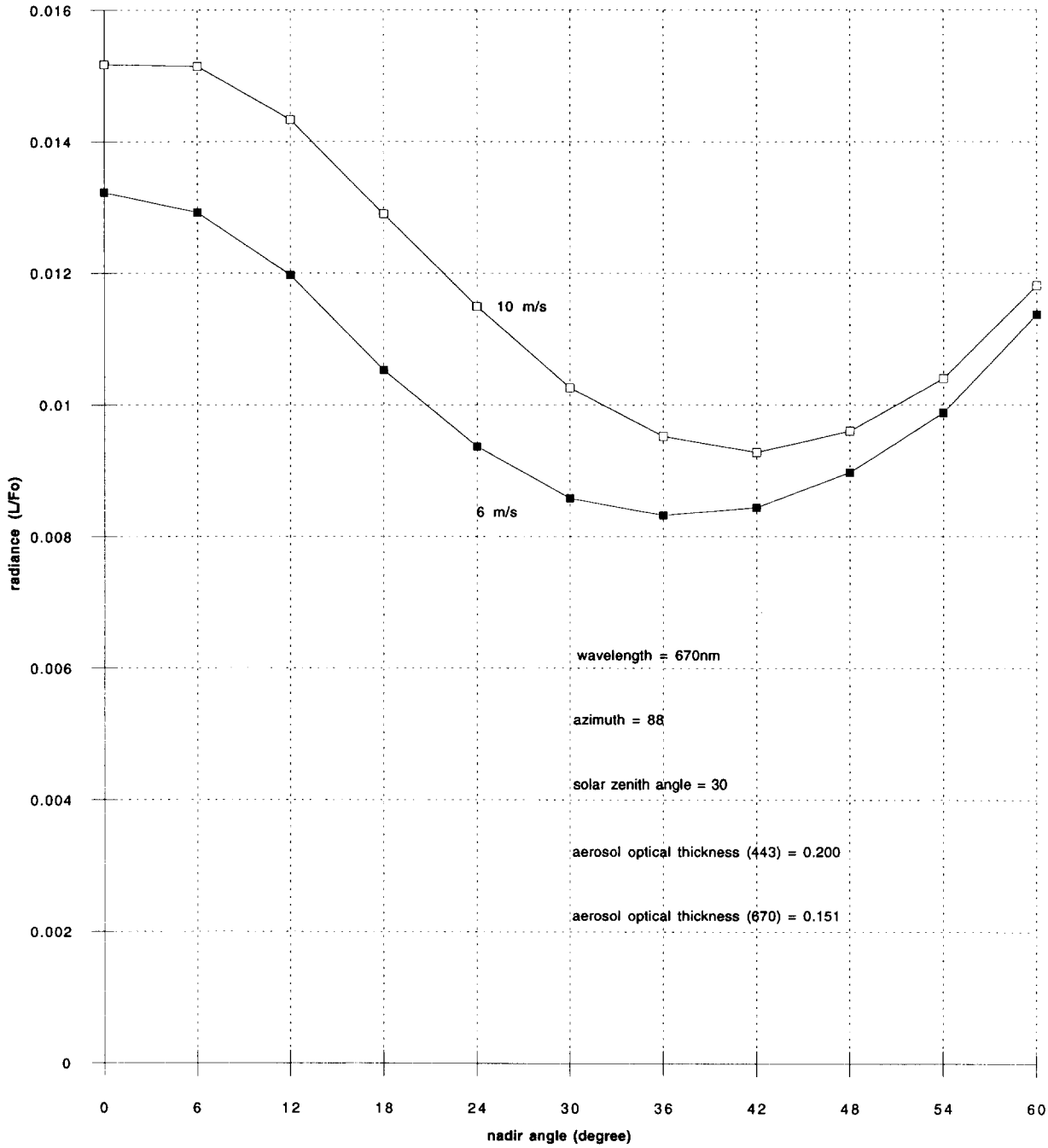

Fig. 2. Comparison of the radiances at the top of the atmosphere for two models with wind speeds of 6 and $10\,\mathrm{m\,s^{-1}}$. The atmospheric model is the same as the maritime model used to compute the look-up tables. The solar zenith angle equals 30°.

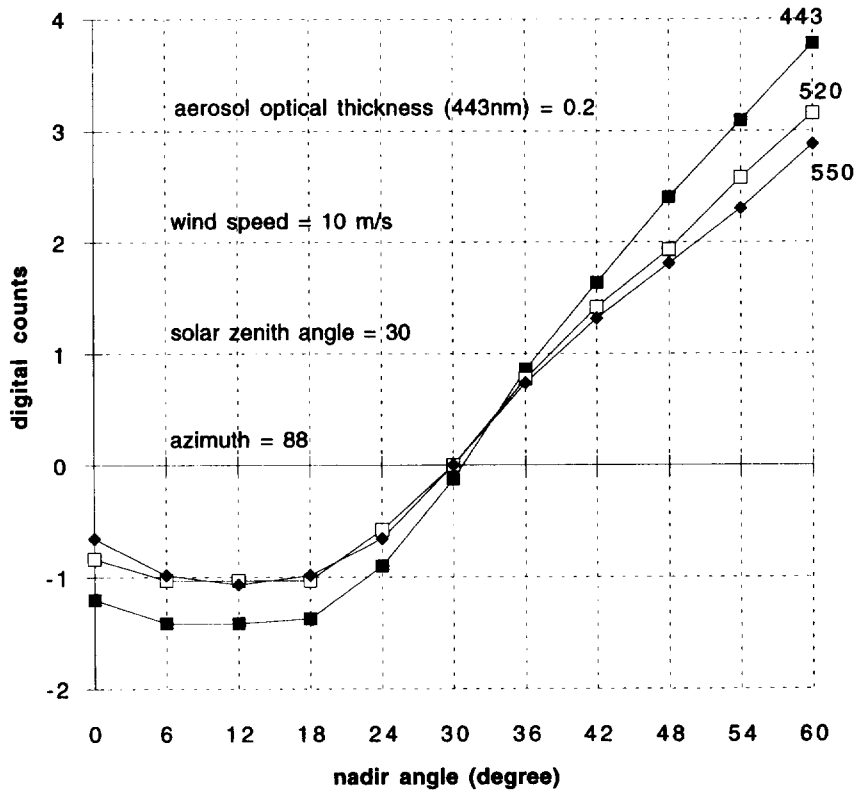

Fig. 3. Water-leaving radiance error for a model with the same atmosphere as the look-up tables, but with a higher wind speed of $10\,\mathrm{m\,s^{-1}}$.

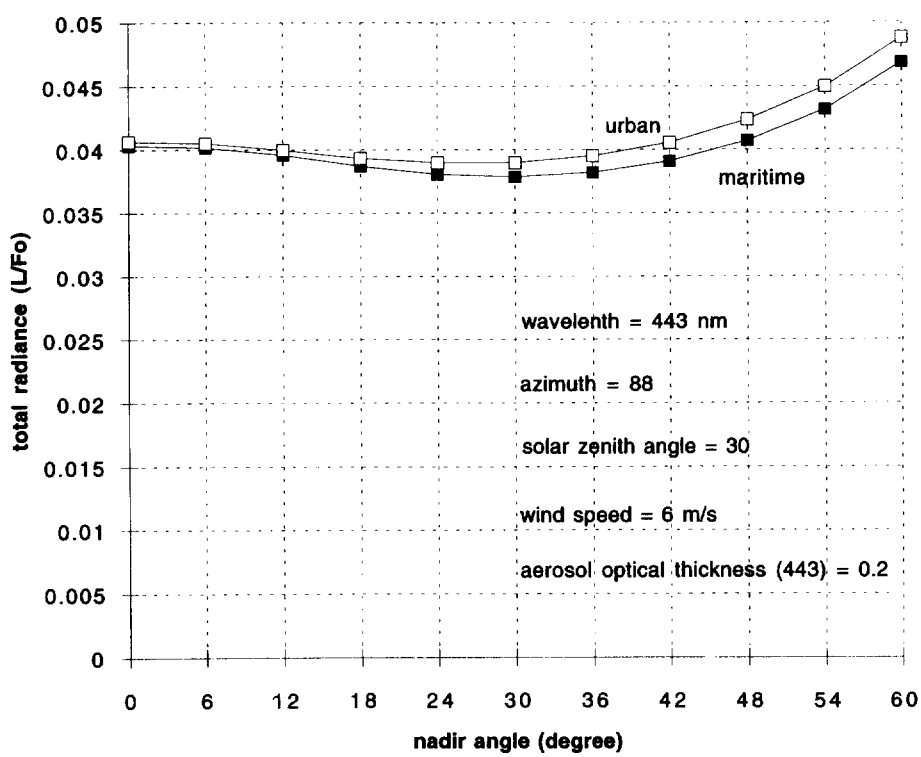

Fig. 4. Comparison of the total radiance at the top of the atmosphere with that of the look-up tables.

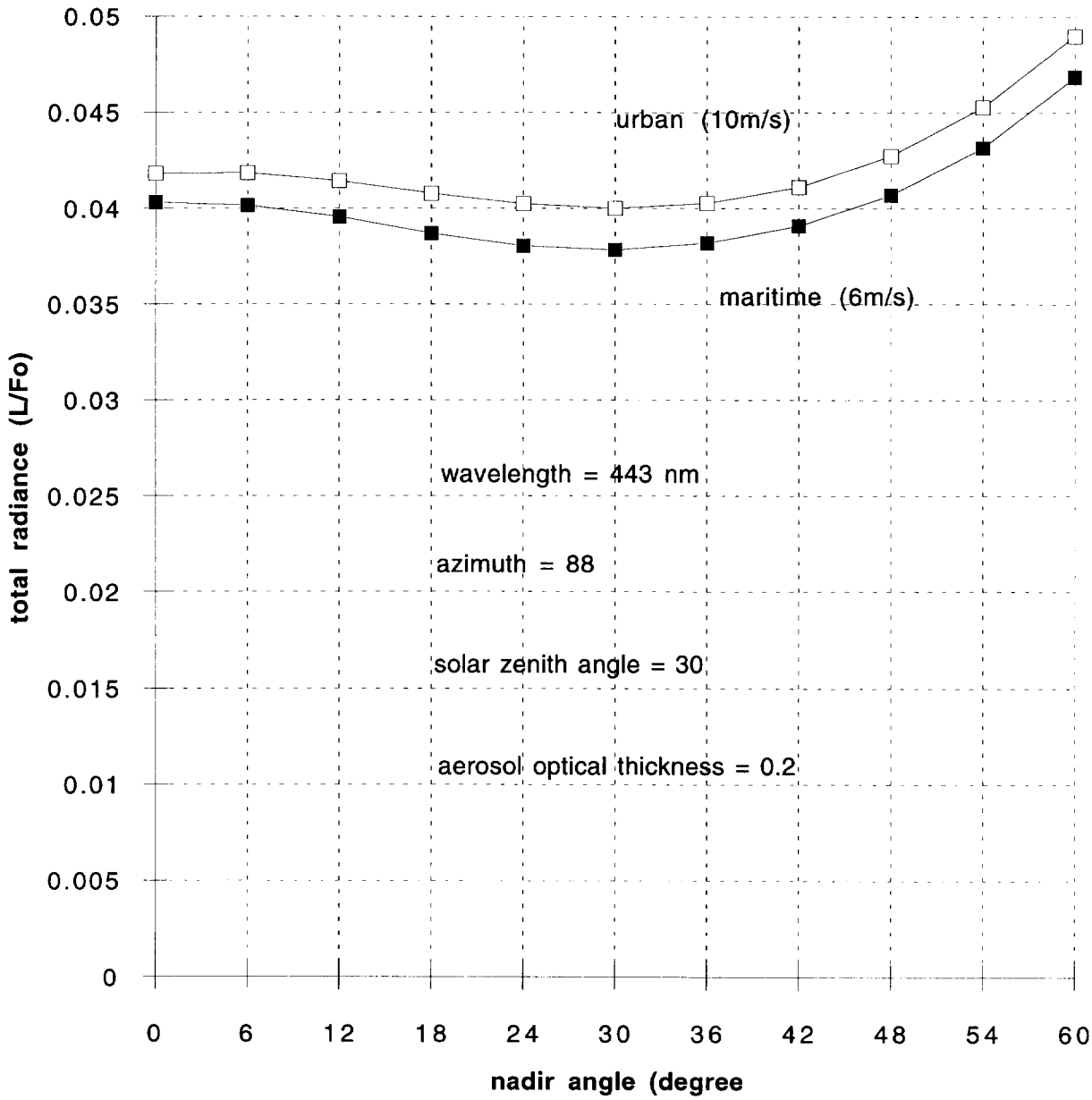

Fig. 5. Total radiance at the top of the atmosphere of an urban model atmosphere and wind speed of $10\,\mathrm{m\,s^{-1}}$ with the look-up table radiance.

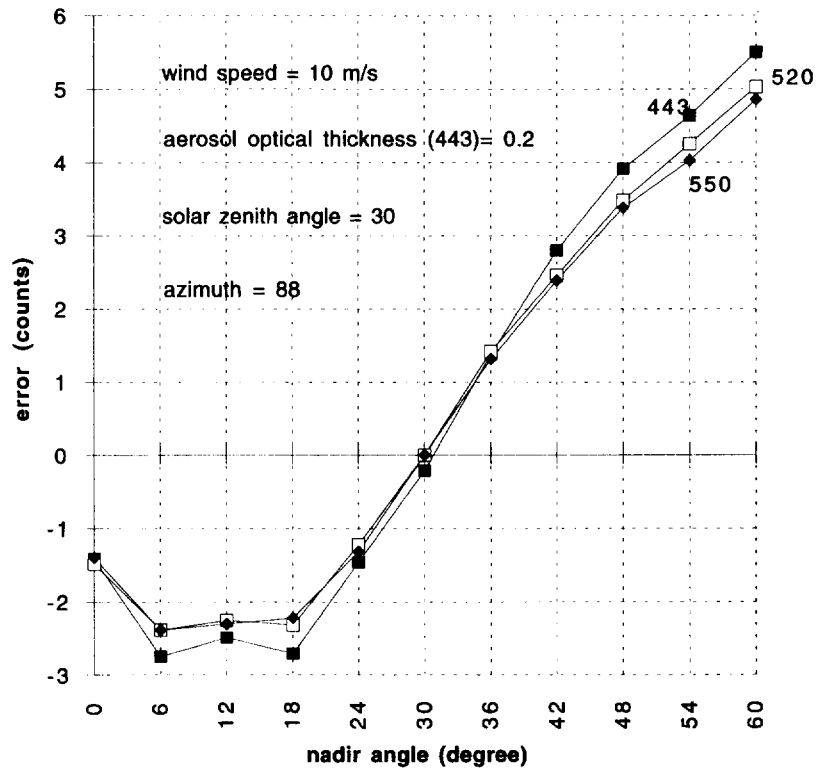

Fig. 6. Water-leaving radiance error for urban model aerosol and wind speed of $10\,\mathrm{m\,s^{-1}}$—Gain 0.

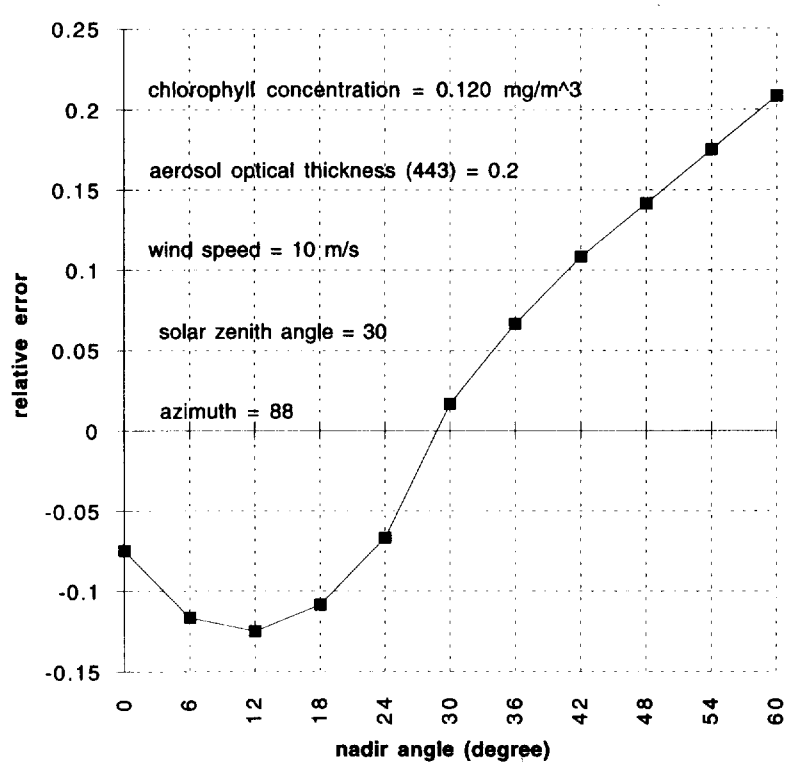

Fig. 7. Relative error in chlorophyll concentration for a model with an urban aerosol and wind speed equalling $10\,\mathrm{m\,s^{-1}}$.

Table 12. The water-leaving radiance relative error is calculated by utilizing the look-up table. The relative error, $\Delta\rho_w(\lambda)/\rho_w(\lambda)$, is given in the last column for a value of the water-leaving radiance error in channel 4, $\Delta\rho_w(670)$, equal to -1.5×10^-4. The relative error is computed with (25). The solar zenith angle equals 30°; view zenith angle equals 42°; the azimuth angle is 88°; and the aerosol optical thickness is $\tau_a(443) = 0.2$.

λ [nm]	Transmission (t')	$\Delta\rho_{LU}/\Delta\tau_a$	γ	$\rho_w(\lambda)/F_0$	$\Delta(\rho_w(\lambda)/F_0)$	Relative Error
443	0.832	0.0205	1.426	6.70×10^{-3}	-2.28×10^{-4}	−0.034
550	0.875	0.0205	1.184	1.80×10^{-3}	-1.79×10^{-4}	−0.100
670	0.921	0.0214	1.000	1.50×10^{-4}	-1.50×10^{-4}	−1.000

Table 13. Optical properties of dust (Fraser 1993). The real and imaginary indices of refraction are given in the second and third columns. The last column gives the average total extinction cross section of a dust particle.

λ [nm]	Real	Imaginary	Albedo of Single Scattering	C_{ext} [cm^2/particle]
443	1.575	0.011	0.80	1.113×10^{-8}
520	1.561	0.0062	0.86	1.136×10^{-8}
550	1.559	0.0050	0.88	1.131×10^{-8}
670	1.548	0.0032	0.94	1.163×10^{-8}

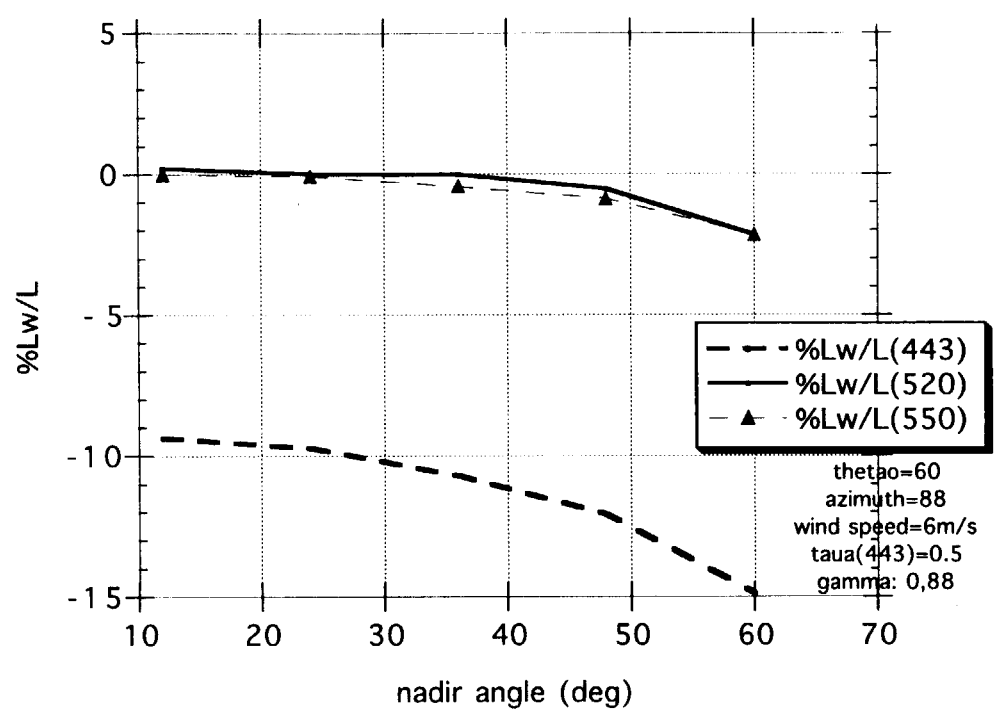

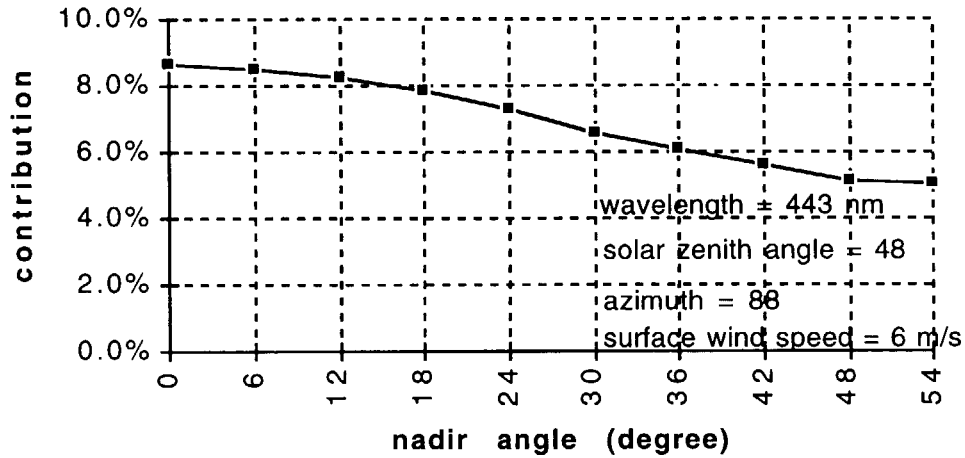

Fig. 9. Relative contribution of the radiance of light reflected from the surface to total radiance at the top of the atmosphere.

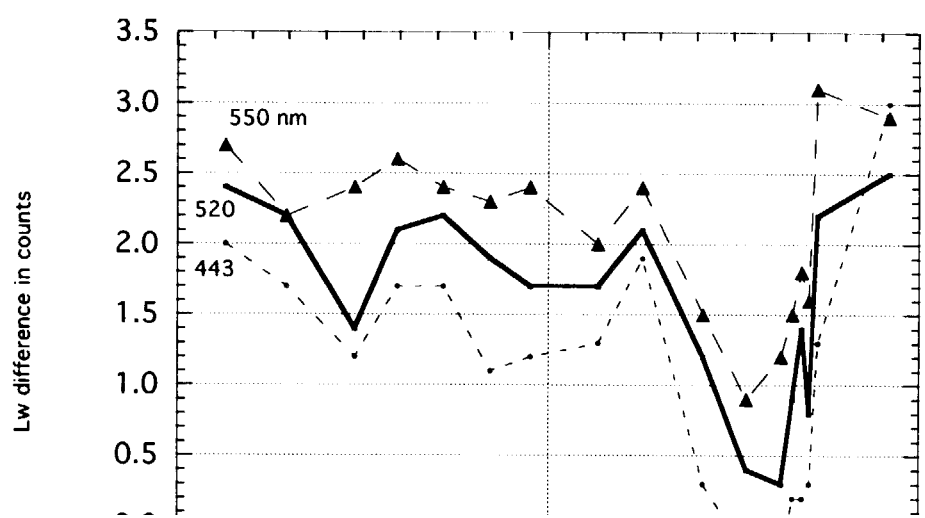

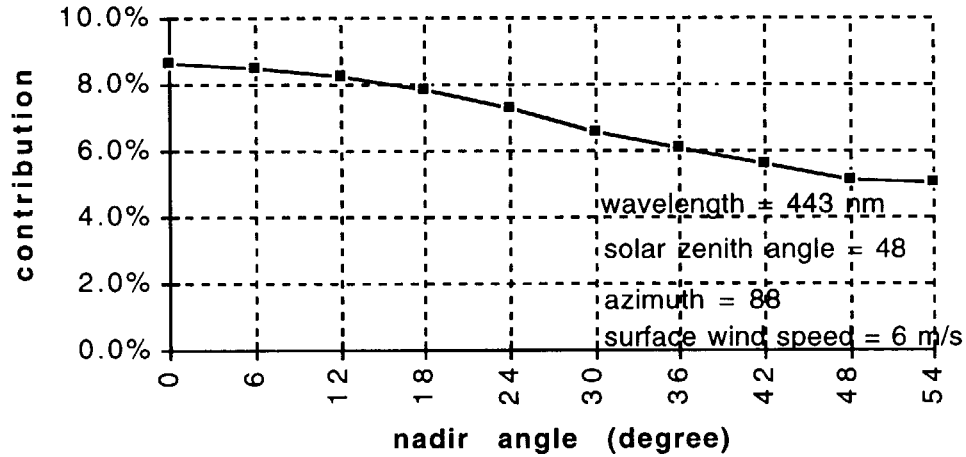

Fig. 9. Relative contribution of the radiance of light reflected from the surface to total radiance at the top of the atmosphere.

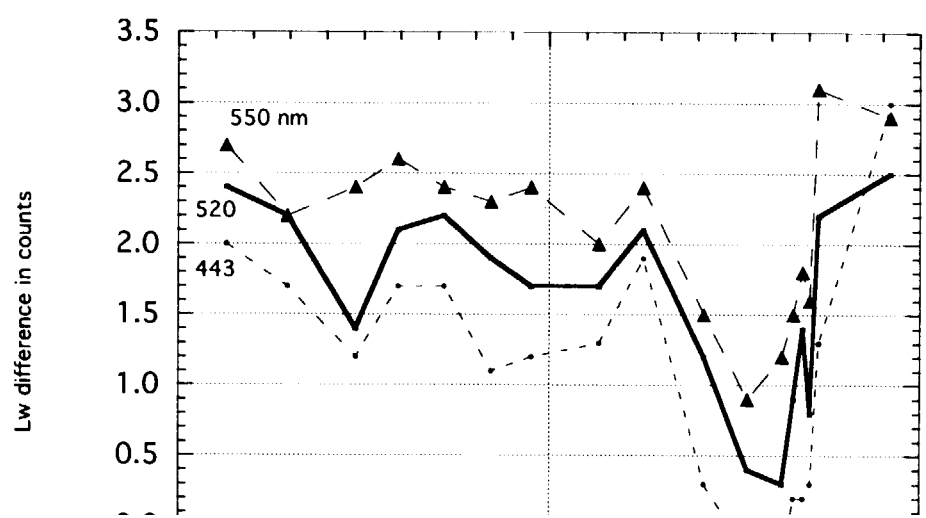

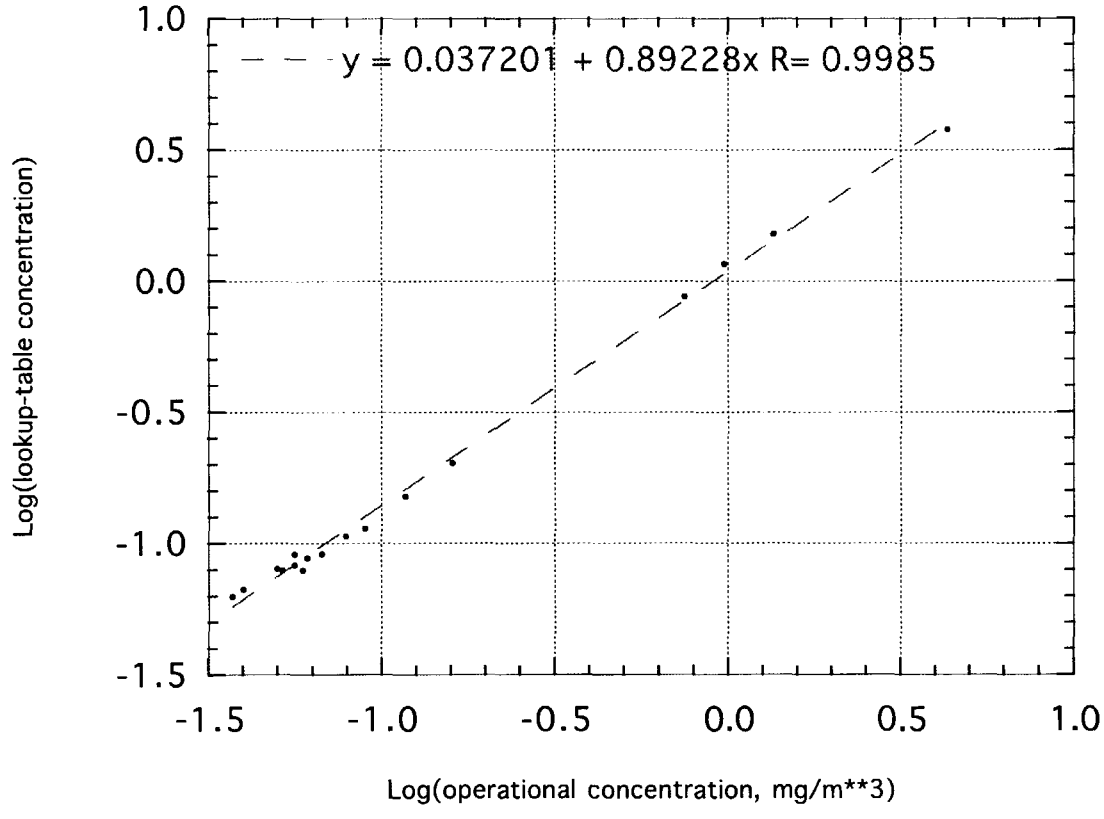

Fig. 11. Comparison of chlorophyll concentrations ($mg\,m^{-3}$) as derived from the look-up tables a the CZCS operational algorithm.

are generally a few counts higher than the CZCS water-leaving radiances (Fig. 10). A generally positive difference of two counts and increasing difference with decreasing wavelength suggests the possibility of calibration errors in the CZCS data. The goal is to get the water-leaving radiances derived from the two methods to differ by less than one count. Because the differences are well correlated among the three wavelengths, the errors tend to cancel when the chlorophyll concentration is computed with a ratio of radiances (17).

The chlorophyll concentrations for both the look-up table and operational algorithms are in good agreement (see Fig. 11). The look-up and operational concentrations are strongly correlated; but there is a bias in the line, since the slope is not equal to one. The look-up tables overestimate

chlorophyll concentrations, could be derived wit in the range of ±15%, because of the strong cor the water-leaving radiance errors for 443 and 550 ulations for stronger perturbation produced radi exceeded the look-up table values and are not herein. Before the stronger perturbations can lated, the look-up tables have to be extended f optical thicknesses of 0.8, 0.9, and 1.0. Still high thicknesses are not required, since the look-up t ances would exceed the CZCS saturation radia errors for an urban aerosol are small, but are una large for aeolian dust. In principal, a separate l ble for dust could be calculated, but its reliabil be uncertain because the optical properties of ae are poorly known. There are at least three di search efforts to determine the optical propertie

Chapter 2

Spectral Reflectance of the Moon

KENNETH J. VOSS
University of Miami, Coral Gables, Florida

ABSTRACT

This report details the results of a field trip to Mauna Loa, Hawaii, the objective of which was to obtain data on the spectral reflectance of a full moon. The end use of this data was to determine the relative levels of spectral reflectance for use by SeaWiFS during its in-flight calibration. For the moon to be a good calibration source, the reflectance of the lunar surface needs to be consistently predicted. The Mauna Loa measurements indicate: 1) lunar reflectance varies with day, and thus perhaps with the lunar phase; and 2) the lunar surface might exhibit a so-called *back gloss*, that is, an enhancement of the reflectance in the direction of the illumination. Because of the latter, the reflectance of the moon may change rapidly during the course of a measurement, and it may be better to make use of the moon as a calibration source when the moon is not full.

2.1 INTRODUCTION

The following is a short report detailing the results of a field trip to Mauna Loa, Hawaii. The objective of the trip was to obtain data on the spectral reflectance of a full moon. The end use of this data was to determine the relative levels of spectral reflectance for use by SeaWiFS during its in-flight calibration.

2.2 INSTRUMENTATION

There were two instruments used in this study. The first was a 10 channel solar photometer designed to measure both the solar transmittance and the sky radiance. Because of its use in measuring the sky radiance, it was designed and built using a photomultiplier as the photodetector. Most sun photometers are built with silicon photodetectors, which while more stable for their primary use, would not be sensitive enough for measurement of the lunar irradiance. The drawback of the photomultiplier is the temperature sensitivity, which is wavelength dependent. The instrument is temperature stabilized for its primary use as a sun photometer, which entails cooling the instrument with thermoelectric peltier pads. On Mauna Loa, however, temperatures were often down to 40° F; hence, heating, not cooling, was required. It was known previously that this might be a problem, but due to the short lead time and other factors, the steps taken to alleviate this problem were insufficient. Thus, upon return from the field, a special calibration was performed to determine the temperature sensitivity of the instrument.

For all but one of the channels, temperature sensitivity was on the order of a few percent. For channel 10 (at 861 nm), however, the temperature sensitivity was not correctable. Since this wavelength is near the long wavelength cutoff of the photomultiplier tube, the temperature sensitivity is extreme. In fact, the sensitivity of the tube at this wavelength varies by a factor of 2 in the range of 40–70° F. Thus, measurements at this wavelength were not obtained. For the other channels, data were reduced using both the raw data and data corrected for the temperature sensitivity, and the difference between the results was less than 5%.

The temperature corrected data are used throughout this report. The second instrument used was an electro-optic camera system originally designed for use in measuring the point spread function in the ocean. The only modification was removal of the housing window and replacement of the wide angle lens (28 mm) with a zoom telephoto lens (185 mm). This allowed images of the moon to be obtained at more than 13 times the resolution expected by SeaWiFS (1.56 mrad). This system was outfitted with a 20 nm interference filter at 500 nm. This allowed measurement of the lunar features in a relatively small spectral bandwidth. These measurements were combined with Hand Held Contrast Reduction Meter (HHCRM) data to obtain reflectance values expected in the SeaWiFS pixels.

2.3 DATA ACQUISITION

The technique of a Langley plot, normally used to measure solar radiance through the atmosphere, was employed to determine the lunar radiance in the presence of the Earth's atmosphere. This technique consists of multiple measurements of the moon (or sun) through varied air

masses, i.e., as the moon (or sun) rises or sets. The logarithm of the moon irradiance values measured is then regressed against 1/cos(zenith angle). The y intercept obtained in this manner is the extraterrestrial value of the lunar (or solar) irradiance. This method depends on a stable, clear atmosphere. For this reason, the Mauna Loa observatory on the island of Hawaii was chosen as a suitable location.

The Mauna Loa observatory is located at an altitude of 11,500 ft and is usually above the marine boundary layer. Its location in the middle of the Pacific Ocean also removes it from most anthropogenic sources of atmospheric particulates. Thus, it should be ideal for these types of measurements. However, the technique does depend on the absence of high level cirrus or other clouds.

Since measurements during the full moon were desired, it was decided to attempt measurements on the two days *before* the full moon, *during* the full moon, and if necessary, on the day *after* the full moon. Fortunately, this last day was unnecessary. On the days before the measurements were to begin, there was a fair amount of cirrus present. On 25 May, the weather was quite clear until approximately 2130 Hawaii Standard Time (HST), when an upslope event caused low level clouds to obscure the observatory. On 26 May, there was significant high level cirrus throughout the day. The cirrus cleared at approximately 1700 HST, which allowed a solar Langley measurement to take place. Skies remained clear until approximately 2030 HST, when the return of light cirrus was recognized by the formation of a halo around the moon. At approximately 2057 HST, the weather cleared for a final lunar observation. Soon after, an upslope event obscured the observatory with low level clouds. On the night of the full moon, high level cirrus obscured the moon during moonrise.

During moonset on the night of the full moon, the momentary occurrence of a clear lunar view allowed lunar measurements to take place. If it were not for the importance of obtaining measurements during the full moon, these measurements may not have been attempted. (When the weather bureau was consulted, full cirrus coverage for the island of Hawaii throughout the night was predicted.) However, as will be shown in the next section, the results obtained appear to be acceptable. No measurements were performed on 28 May, the night after the full moon in Hawaii, as the weather showed no sign of improvement.

2.4 RESULTS AND DISCUSSION

The desired quantity is reflectance, ρ, which is defined as:

$$\rho = \pi \frac{L_M}{E_S}, \tag{34}$$

where E_S is the irradiance of the sun and L_M is the radiance of the moon. In terms of experimentally measured quantities, the latter is:

$$\begin{aligned} L_M &= \frac{H_M}{\Phi_M} \\ &= C_F \frac{\Phi_D}{\Phi_M V_M}, \end{aligned} \tag{35}$$

where C_F is a calibration factor, H_M is the measured moon irradiance, Φ_M is the solid angle subtended by the moon at the measuring instrument, Φ_D is the detector solid angle, and V_M is the voltage read on the detector. The extraterrestrial solar irradiance, E_S, can be determined from a table (Neckel and Labs 1984), or it can be determined with a technique similar to that used in measuring the moon. For the latter, E_S is given by:

$$E_S = C_F \Phi_D V_S N_D, \tag{36}$$

where the N_D factor compensates for the approximately 4 log neutral density filter, which is inserted in the detector for solar measurements but not lunar measurements. This neutral density filter was previously measured in two different ways to derive a consistent spectral dependence of the true density factor.

When written out as above, L_M and E_S can be combined to give:

$$\begin{aligned} \rho &= \pi \frac{L_M}{E_S} \\ &= \pi \frac{V_M}{N_D V_S \Phi_M}. \end{aligned} \tag{37}$$

Note that in (36) the calibration factor, C_F, and Φ_D cancel and the measurement only depends on N_D, the ratio of the voltages measured, and the solid angle of the moon (a factor which is well known). This is the equation used in this report to obtain ρ.

Two factors which enter into the above equation are neglected in this presentation. The first factor is the distance variation between the sun and the moon, and the second is the distance variation between the Earth and the sun. The first factor is important when measuring the L_M, as this distance determines the solar irradiance falling on the moon. The second factor is important when measuring the E_S, as this distance determines the solar irradiance measured on the surface of the Earth. Both of these factors varied by only 0.05% during the measurement period. Also, these factors were approximately equal (to within 0.3%). In this case, they were assumed to cancel. If the lunar measurements and solar measurements were to take place at different periods in the year, these factors would become important.

The Earth-moon distance varied during the measurement period and this affects the above equations through the Φ_M factor. The mean angular subtense of the moon is 0.518°. The distance from the moon to the Earth, normalized by the mean Earth-moon distance, varied from 1.0326

Table 14. Lunar and solar radiances as a function of wavelength (units of $\mathrm{mW\,cm^{-2}\,\mu m^{-1}\,sr^{-1}}$).

Wavelength	*25 May*		*26 May*				*27 May*	
[nm]	V_M	τ	V_M	τ	V_S	τ	V_M	τ
381	1.23	0.387	1.48	0.304	179.0	0.280	2.11	0.302
410	1.81	0.314	2.10	0.245	237.0	0.224	3.00	0.246
440	3.61	0.281	3.99	0.185	407.0	0.167	5.65	0.181
488	2.33	0.175	2.53	0.128	232.0	0.122	3.55	0.124
522	1.40	0.202	1.67	0.124	137.0	0.098	2.24	0.103
558	4.10	0.175	4.48	0.110	369.0	0.069	6.19	0.103
611	3.00	0.202	0.320	0.080	26.4	0.041	0.439	0.079
672	4.81	0.147	0.516	0.056	39.1	0.036	0.707	0.053
779	1.24	0.121	1.318	0.036	125.0	0.015	1.75	0.025

(25 May) to 1.0506 (28 May). This variation was taken into account in Φ_M.

Langley plots for each day were generated. The intercept of the fit in these plots is important, since this is $\ln(V_M)$, or in the case of the solar measurement, $\ln(V_S)$. The slope represents the atmospheric attenuation, τ, which is the sum of Rayleigh, aerosols, and other gas extinctions. In most sun photometry studies, τ is the desired quantity. Of note in these Langley plots are the very good regression coefficients obtained on 25 and 26 May, and apparently spurious values for 27 May.

The problem for 27 May appears to be caused by two points. However, no mention of cloud problems is noted in the experimental log. As previously discussed, these observations took place on a difficult night with many clouds moving in and out, so these points could still be suspect. However, neglecting these points makes little difference in the intercept or slope. Their inclusion only seems to strongly effect the R^2 value, so the points were not removed.

Table 14 summarizes the results for the three nights of lunar HHCRM measurements and one day of solar measurements. The interesting thing to note on the values are the consistency of the values for the evenings of 26 and 27 May 1991, and how close these are to the values in the afternoon of 26 May. This is to be contrasted with 25 May, for which the attenuation values obtained were much higher. The regression coefficients for this day were very good which would indicate that these values should be reliable, also the L_M values obtained on this day were fairly consistent with the other days.

Values of ρ were analyzed from the data in Table 14 using a power law. The results of this analysis are presented in Table 15. Interestingly, the exponent of the relationship seems to vary regularly with day, and thus perhaps with the lunar phase. Another measurement, obtained in Miami previous to this set, at a different phase angle (much smaller) showed a power law relation exponent of 1.03. The trend appears to be toward a flattening of the spectral dependence of ρ with increasing phase angle, i.e., toward a full moon.

Table 15. Values of ρ analyzed from the data in Table 14 using a power law.

Wavelength	ρ		
[nm]	*25 May*	*26 May*	*27 May*
381	0.059	0.068	0.098
410	0.059	0.070	0.101
440	0.067	0.074	0.106
488	0.073	0.080	0.113
522	0.073	0.088	0.119
558	0.080	0.088	0.123
611	0.084	0.090	0.125
672	0.097	0.105	0.146
779	0.097	0.104	0.139

The above discussion deals with the average ρ of the lunar surface. The lunar surface has a varied reflectance pattern. To characterize this variation, each night higher resolution imagery was obtained using a charge coupled device (CCD) array camera system. The first data reduction step taken with these data was to integrate the image over the lunar surface. While the camera system could be calibrated absolutely, it was not practical to perform a Langley-type measurement scheme with it. Thus, the atmospheric attenuation was not be determined using the CCD camera system.

The integral values of the lunar surface were used in combination with the HHCRM measurements to perform an empirical calibration. In this manner, the camera counts could be related to ρ easily, without considering the atmosphere. The next step in the image analysis was to subsample the lunar surface at the angular resolution of the SeaWiFS instrument. This step was done by moving a 13×13 pixel grid, or *super pixel*, over the image of the moon. Each super pixel completely on the lunar surface was integrated, and the resulting values were then used to compile histograms. It is important to note that this is the complete set of possible reflectances seen at the SeaWiFS angular resolution. The histograms show that the moon has a bimodal distribution of reflectances in all cases. Also note the wide spread in possible values that can occur.

For the moon to be a good calibration device, it must be possible to consistently predict the ρ of the surface. To test one possibility, the moon was divided into these super pixels and then the maximum super pixel value was determined. The squares were shifted slightly and the maximum determined again. In this way, the variability in the maximum reflectance could be determined. The result of this test is that the average maximum ρ (27 May) was 0.171 ± 0.00623 where the latter number is the standard deviation. It can be shown by analyzing the distribution of maximum values that the distribution of ρ values on 27 May is far from a normal distribution. This is probably caused by a strongly varying bidirectional reflectance in the near normal direction. Many materials exhibit a *back gloss*, an enhancement of the reflectance in the direction of the illumination, i.e., looking at a surface with the illuminating source behind you. For this reason, the reflectance of the lunar surface may be changing rapidly. Because of this phenomenon, it may be better to make use of the moon as a calibration source when the moon is not full. For example, the mean and standard deviations for the 26th and 25th are 0.114 ± 0.00381 and 0.108 ± 0.00242. Not only are the standard deviations lower, but the shape of the function is more normally distributed.

Chapter 3

Preflight Solar-Based Calibration of SeaWiFS

STUART F. BIGGAR
PHILIP N. SLATER
KURTIS J. THOME
University of Arizona, Tucson, Arizona

ALAN W. HOLMES
Santa Barbara Research Center, Goleta, California

ROBERT A. BARNES
ManTech Environmental Technology, Inc.
Wallops Island, Virginia

ABSTRACT

A new method for performing a preflight calibration of an optical remote sensing instrument with an onboard solar diffuser calibration system is presented. The rationale, method, advantages, disadvantages, error sources, and expected accuracies are discussed. The method was applied to the SeaWiFS instrument to be flown on the SeaStar satellite.

3.1 INTRODUCTION

Integrating sphere sources are commonly used for the preflight calibration of sensors† in the solar reflective spectral range. They have the advantage of providing a full aperture, full field, end to end calibration at several different points over the dynamic range of the sensor. However, integrating sphere sources have several disadvantages related to the lamp sources used and the reflective coatings of the spheres.

Tungsten quartz halogen lamps, operated at a color temperature of about 3,000 K, are usually used to illuminate the sphere interior. The output of these lamps peaks at about one micrometer and falls off rapidly at shorter wavelengths. Thus, it is difficult to match the radiance level of solar radiation reflected from the Earth's atmosphere and surface at short wavelengths using an integrating sphere source. Also, the rapid fall-off of the spectral radiance is both difficult to measure, and to account for accurately, in the calibration of the sensor's short wavelength spectral bands. The measurements made by the sensor are of reflected solar radiation; the sun's spectrum contains Fraunhofer lines, whereas lamps do not contain these absorption features. For sensors with narrow spectral bandpasses, e.g., less than 10 nm, the presence of a Fraunhofer line within a bandpass can change the response of the sensor by several percent with respect to its integrating sphere source calibration (Flittner and Slater 1991).

The interior of a large integrating sphere source is usually coated with barium sulfate ($BaSO_4$) paint. The spectral reflectance of the paint is reasonably flat in the visible and near infrared, but exhibits rapid changes in the shortwave infrared that are difficult to account for accurately in a calibration. Integrating sphere sources have some instability associated with them. There are several causes: the instability of the power supplies, the warm-up time required for the lamps to become stable, and the warm-up time required for the $BaSO_4$ paint in the sphere to lose any water vapor it has absorbed. In addition, there are the uncertainties associated with the calibration of the irradiance standard used to calibrate the output radiance of the sphere, the transfer of the lamp scale to the sphere output, and the aging of the sphere lamps and coating. The first is a function of wavelength, being approximately ±1% in the visible, but greater than ±2% in the shortwave infrared. (All uncertainties given in this paper are one standard deviation, or one σ.) When all these sources of uncertainty are considered, it is obvious that to achieve an uncertainty as low as, say, ±3% for the output of an integrating sphere source is very difficult, time consuming,

† This chapter originally appeared as an article in an *SPIE* publication (Biggar et al. 1993) and is being included in this volume with permission of the authors. Minor editorial changes have been made to reflect the style of *The SeaWiFS Technical Report Series*.

and costly. Furthermore, in practice, it will be misleading for spectral bands of the sensor that fall over strong Fraunhofer lines.

The best form of onboard calibration is provided by a solar diffuser, because it is end to end, full aperture and full field, and has the appropriate spectral distribution and radiance levels at all wavelengths. However, one of the main shortcomings of solar diffusers is that no method has been found to calibrate the sensor preflight *via the solar diffuser* without using the aforementioned tungsten lamp. Thus, an assumption has to be made that the in-flight calibration of the sensor *via the solar diffuser* is not subject to systematic errors. This assumption implies that the bidirectional reflectance distribution function (BRDF) of the diffuser, and the irradiance on the diffuser, are both accurately known. Without the use, ideally, of a ratio taking radiometer (Slater and Palmer 1991), or an alternative solar diffuser monitor (Pagano and Durham 1993, Bruegge et al. 1993), questionable assumptions must be made concerning freedom from stray light on, and contamination of, the diffuser. In any case, the results of an onboard diffuser-based calibration can only be approximately related to a preflight integrating sphere source calibration, partly for the reasons given earlier, and partly because of the uncertainty in our knowledge of solar exoatmospheric spectral irradiance.

This paper describes what is believed to be the first attempt at a preflight solar based calibration of a sensor and diffuser system, conducted using the *same* illumination and viewing geometry as will be used during in-flight calibration. The preflight solar based calibration can be directly compared to the preflight integrating sphere and source calibration, thus providing a desirable link between in-flight solar based calibration, which is simply in digital counts (DC), and the preflight absolute calibration in DCs per unit in-band spectral radiance. The link then is directly to national laboratory standards in physical units. In respect to national standards, it is worth emphasizing that the sun's output is the same anywhere on earth, while there are differences in the irradiance and radiance scales between different national standards laboratories.

There are various risks and disadvantages associated with this method of calibrating a sensor. First and foremost is the risk to the sensor associated with the move to an appropriate site outside. There is also a chance of contamination of the optics when actually doing the experiment. Clear sky conditions are required, and a very low aerosol loading is best. Accurate transmittance measurements are required. High accuracy solar exoatmospheric spectral data are needed to provide an accurate comparison with national laboratory standards. The currently available solar data are not sufficiently accurate, nor of high enough spectral resolution, for such a comparison.

The calibration procedure necessitates illuminating the diffuser on the flight sensor with direct solar irradiation. Heath (pers. comm.) has described a similar procedure, not for sensor calibration purposes, but to provide a measure of the relative ozone columnar concentration from the various Solar Backscatter Ultraviolet (SBUV) instrument spectral bands.

In order to calibrate SeaWiFS via the diffuser, the unit had to be taken outside. (In the case of the SBUV instrument, the laboratory roof was opened.) The possibility of taking a flight unit sensor outside was not anticipated by the University of Arizona authors until, at the first SeaWiFS Science Team meeting in January 1993, during a Santa Barbara Research Center (SBRC) presentation, A. Holmes remarked that this had been done to check that the appropriate gain settings had been selected for diffuser and lunar viewing. This prompted P. Slater to propose to the Science Team that a solar based preflight calibration be attempted. Such an approach was approved by the Science Team and the Project Managers from SBRC and GSFC. The hour-long calibration, described here, was conducted at SBRC on 8 March 1993 by S. Biggar, K. Thome, A. Holmes, and other SBRC staff.

3.2 CONCEPT

The concept is simple. An attempt is made to duplicate, on the ground, the solar illumination conditions seen by the sensor in orbit. This simulation requires *just* the direct solar beam, and it must illuminate the diffuser at the incidence angle used during in-flight calibrations. The requirement for *just* the direct solar beam is the difficult one. At ground level, there is substantial scattering of the direct beam by the molecules of the atmosphere, as well as the aerosols distributed in the lower part of the atmosphere. This scattering is strongly wavelength dependent, and causes a variable amount of diffuse light, which illuminates the diffuser from angles other than the solar incidence angle.

The atmosphere also attenuates the direct beam, as compared to the beam at the top of the atmosphere. Therefore, the simulation must compensate for the lower-than-unity atmospheric transmittance. Part of the transmittance loss is caused by absorption by gases such as ozone, oxygen, and water vapor. Another cause of lower transmittance is the loss due to scattering of light out of the direct beam into the diffuse field. In order to make the calibration, corrections are made both for the transmittance and for the diffuse light that illuminates the diffuser.

3.3 METHOD

The method described in this section is generic to any sensor with a solar diffuser. The procedure is to situate the sensor such that the solar diffuser is illuminated in the same geometry as the in orbit geometry during calibration. The mount for the instrument must have several angular degrees of freedom in order to correctly align the diffuser and instrument and, hopefully, allow continual

tracking of the sun. When the diffuser is aligned correctly, the digital counts from the sensor while it is viewing the diffuser are recorded for each spectral band. Then the diffuser is shadowed by a small disk that blocks the direct beam and the digital counts are again recorded for each band. The difference, corrected for the atmospheric transmittance and the small component of diffuse light blocked by the disk, corresponds to the in-orbit illumination of the diffuser. The transmittance is measured during the period of diffuser measurements with a solar radiometer. The optimal choice for the solar radiometer wavelengths would be the actual sensor bands if they are sufficiently narrow, but in general this may not be possible. Schematic diagrams of the illumination geometry for the experiment, both fully illuminated (Fig. 12) and shadowed by the disk (Fig. 13) are provided. Figure 14 is a photograph of the experiment as done at SBRC on 8 March 1993.

3.4 ERROR SOURCES

In this experiment, we want to determine the digital counts (DC) that will be measured at the top of the atmosphere (TOA):

$$DC_{TOA}(\lambda) = \frac{DC_{\text{meas}}(\lambda)}{T(\lambda)} - DC_{\text{scat}}(\lambda) \qquad (38)$$

where $T(\lambda)$ is the transmittance along the slant path to the sun, DC_{meas} are the digital counts measured unshadowed, and DC_{scat} are the digital counts due to scattered sunlight for wavelength λ.

There are several error sources that must be carefully considered when doing the experiment. The first error relates to the measured transmittance. The atmospheric transmittance along the slant path from the sun to the diffuser must be known accurately. The transmittance $T(\lambda)$ is defined as

$$T(\lambda) = e^{-\sigma(\lambda)/\mu_s} \qquad (39)$$

where $\sigma(\lambda)$ is the spectral optical depth, $\mu_s \approx \cos\theta_s$, and θ_s is the solar zenith angle.

The errors in transmittance must be understood to allow differentiation of the transmittance defined in (39) as a function of the various components, and to determine the fractional error in $T(\lambda)$ as

$$\frac{\Delta T(\lambda)}{T(\lambda)} = -\frac{\Delta\sigma(\lambda)}{\mu_s} + \frac{\sigma(\lambda)\sin\theta_s\Delta\theta_s}{\mu_s^2} \qquad (40)$$

where $\Delta\sigma(\lambda)$ is the absolute error in optical depth ($\sigma(\lambda)$), and $\Delta\theta_s$ is the error (in radians) in the knowledge of θ_s.

Note that for a well designed experiment, the second term in the fractional error equation, (39), will be quite small as compared to the first. The absolute error in optical depth is normally wavelength dependent, being greater at shorter wavelengths where the optical depth is normally greater. A second order error term, not dependent on the transmittance, is caused by the unavoidable blockage of a small part of the diffuse field by the small disk. This error term is expressed as the second term in (38). This blocked diffuse light is the central part of the solar aureole and is the strongest part of the diffuse field, as almost all of this light consists of forward scatter from the direct solar beam. We can make a first order correction for the blocked aureole with very small uncertainty. Another small error source derives from the non-Lambertian characteristic of any real diffuser. These last two errors are difficult to quantify without detailed specifications for the diffuser, diffuser screen (if present, as in SeaWiFS), apertures, and any baffles.

The experiment can be conducted to best minimize the errors. The first and most important goal is to reduce the optical depth uncertainties and hence the uncertainty in the transmittance computations. The solar radiometer used to measure the transmittance should be linear and well calibrated. Filter radiometers based on silicon detectors are linear and stable, and can be calibrated to an uncertainty of a few percent. Reliance on the calibration of the radiometer can be reduced by taking data over an extended period, corresponding to a large variation in solar zenith angle from 75° to as low a value as is available on the calibration day (Biggar et al. 1990). If the atmosphere is stable over that period, a Langley plot can be made from the data for each band. The slope of each plot is equal to the optical depth in that band of the radiometer. A Langley plot requires only a linear instrument and a stable atmosphere.

Another strategy for reducing transmittance errors is to make the measurements on a very clear day with low aerosol loading and low humidity. This strategy will reduce the scattering due to aerosols, and therefore the uncertainty in the aerosol scattering. The low humidity reduces the absorption in any water vapor bands. Similarly, measurements could be best made at high altitude sites with low aerosol loadings, such as good astronomical observatory sites. The high altitude reduces both Rayleigh and aerosol scattering and reduces absorption due to all gasses present in the atmospheric boundary layer.

Another method for reducing the transmittance uncertainty is to make the actual solar diffuser measurements at the lowest possible solar zenith angle. The slant path is then the shortest, and the fractional error equation, (39), shows a secant of solar zenith angle dependence. Hence, weather permitting, the measurements should be made at solar noon. Every effort should be made to ensure that all angles are known and set to the appropriate values.

In order to reduce the uncertainties in the correction for the diffuse light, several precautions should be taken. The shadower disk should be as small as possible to reduce the blocked aureole. As the disk will probably be at the end of a 5 m long pole, however, the disk must be large enough to still completely cover the full diffuser aperture while allowing for small errors in positioning. The disk used in the

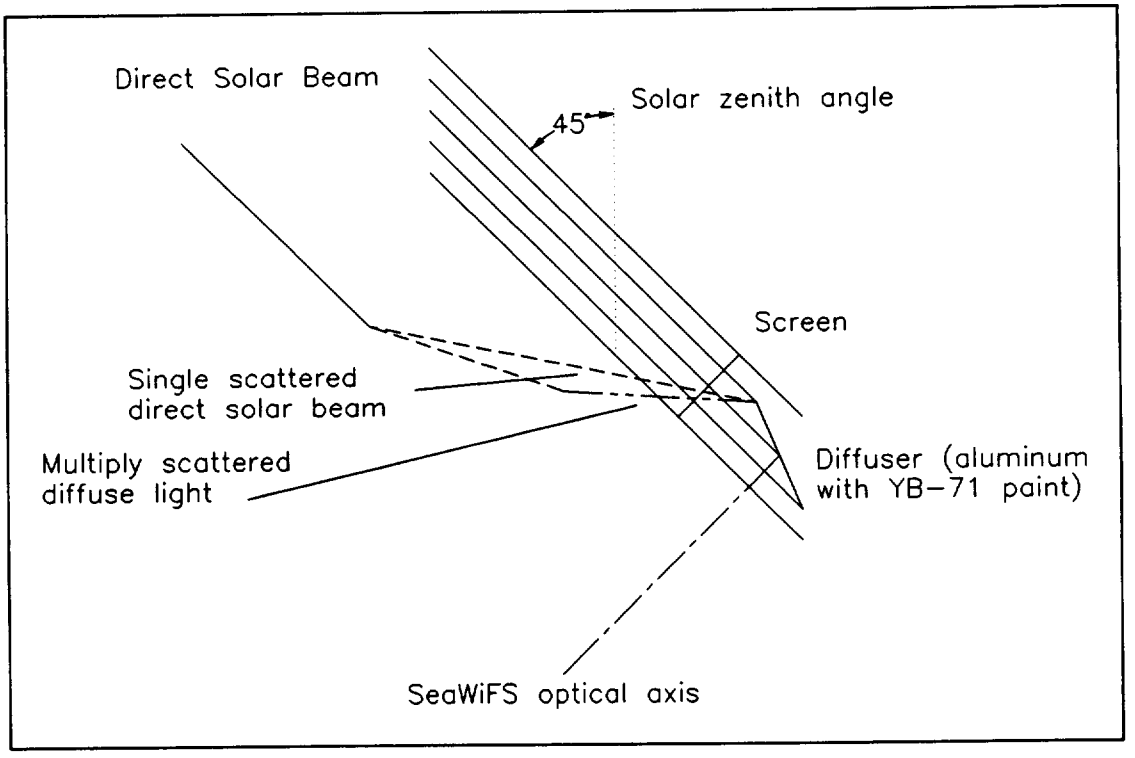

Fig. 12. Experiment illumination geometry—unshadowed.

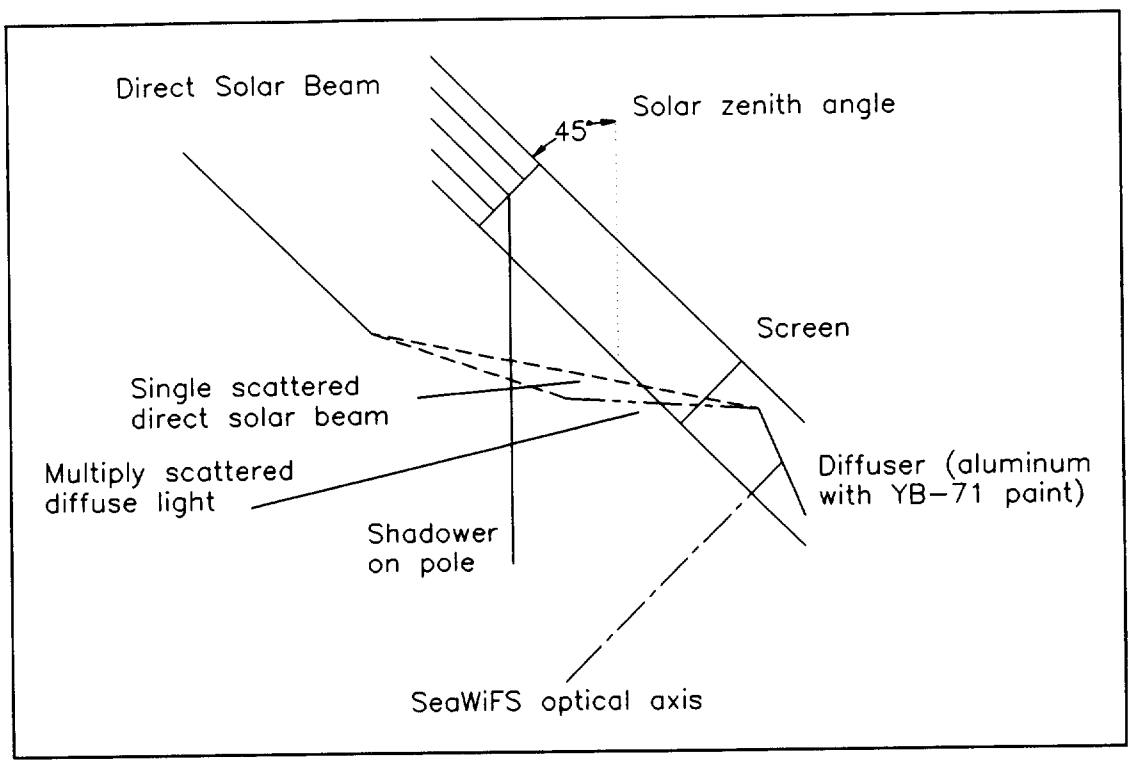

Fig. 13. Experiment illumination geometry—shadowed.

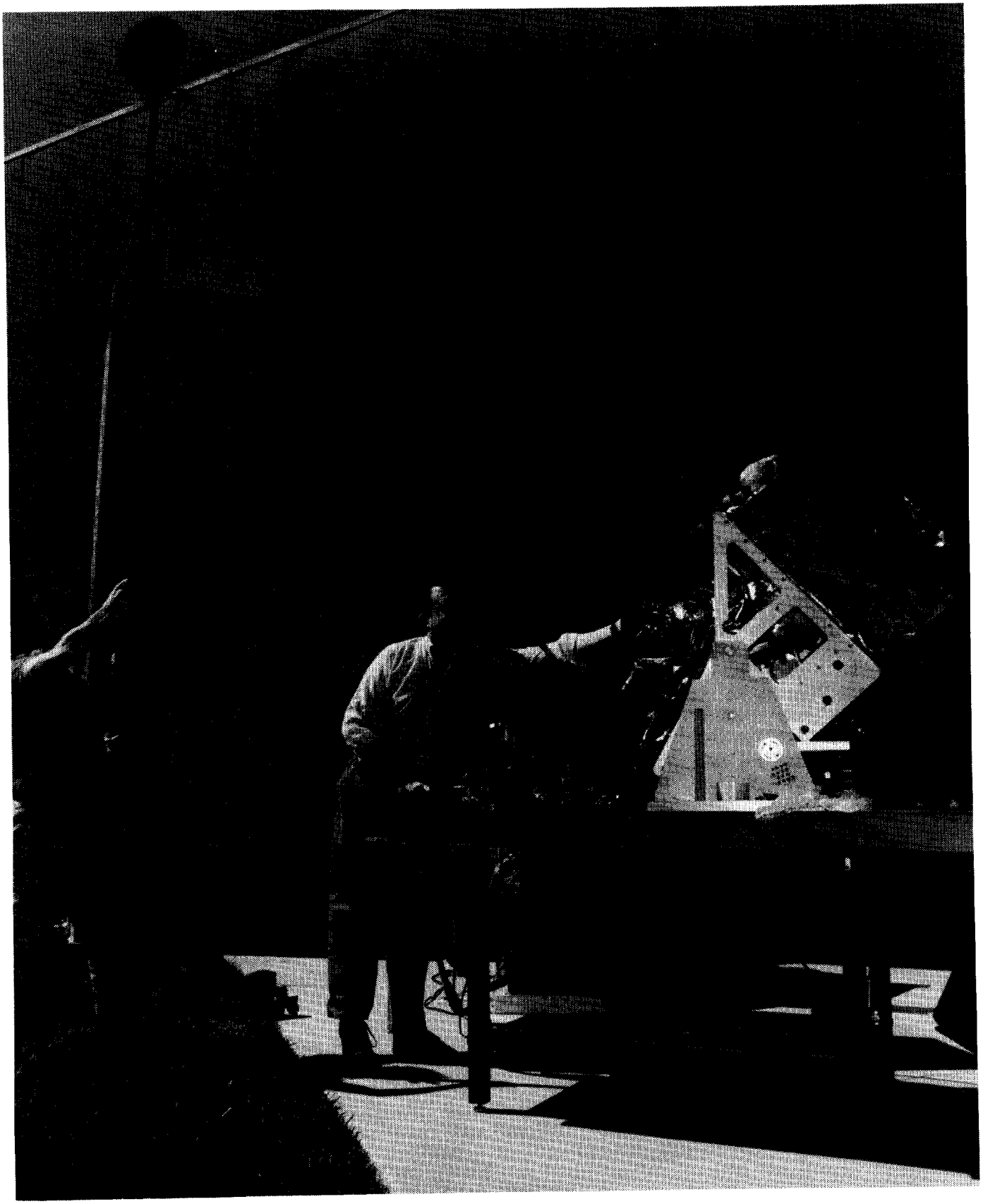

Fig. 14. SeaWiFS solar based calibration experiment, 8 March 1993 at SBRC in the "Rock Garden."

Table 16. Solar-based calibration results.

Band No.	*Gain Setting*	*Transmittance*	*Unshaded DCs*	*Shaded DCs*	*Forward Scatter DCs*	*Predicted In-Flight DCs*	*Sphere-Derived DCs*
1	2	0.567	420	21	1	701	708
2	3	0.634	355	17	1	532	546
3	3	0.708	484	19	1	655	670
4	4	0.728	737	28	2	972	1,004
5	1	0.763	618	23	1	778	808
6	4	0.836	625	22	1	720	730
7	4	0.799	581	21	1	699	729
8	4	0.895	664	26	1	712	772

SeaWiFS experiment was 30 cm in diameter and was at the end of a 5 pole. The diffuser aperture, about 80 mm in diameter, was about 1.7 m above the ground. The blocked solid angle was small, but a correction was still necessary. Knowing the precise geometry of the disk/diffuser assembly and the sun also reduces uncertainty in the correction computation. In a similar vein, the measurements are best made on a very clear day, as the scattering is reduced, the diffuse signal is smaller, and the uncertainty in the direct beam computation is then reduced.

3.5 ACCURACY

In order to simulated the signals expected in this type of calibration, a nominal 23 km visibility US standard atmosphere was used. The extinction optical depth, which is measured during the experiment, is comprised of various components: those due to Rayleigh scattering, aerosol scattering, ozone absorption, water vapor absorption, and also including absorption due to other gases such as oxygen, carbon dioxide, and nitrogen dioxide. The Rayleigh optical depth can be known accurately from the barometric pressure, which is measured for each optical depth data point.

The error in the optical depth is due to the aerosol optical depth and extinction due to absorption. This error should be less than 3% of the difference between the extinction and Rayleigh optical depths. For a standard atmosphere, this corresponds to a transmittance uncertainty of ±2.7% to ±1.1% for the shortest to longest wavelength SeaWiFS bands, at a solar zenith angle of about 60°. This uncertainty could be reduced by making the measurements at a higher solar elevation (the error would be lower by a factor of 1.65 if the measurements were taken at noon in early March with a solar zenith angle of 39°).

The errors in the calibration which are attributable to the small disk are smaller than the transmittance uncertainties, yet are much more difficult to quantify. The uncertainty in the *global minus diffuse* measurement was estimated to be about ±0.8%, after correction for the blocked component of the aureole. There is another 0.4% uncertainty due to the inaccuracies in measuring the various angles. The total uncertainty is therefore estimated to be from ±2.8% to ±1.4%, depending on wavelength, for a solar zenith angle of 60°. The uncertainty could be as low as ±1.9% to ±1.1% for a noon measurement in early March at SBRC. These uncertainties are one σ with respect to the solar output.

3.6 RESULTS

The calibration experiment was done in early March 1993. In conjunction with the 8 March 1993 experiment, Kurtis Thome measured the atmospheric transmittance during the afternoon of 7 March 1993. This measurement was to be used to infer the transmittance during an attempt to view the full moon during moon rise that evening. The conditions were good during the afternoon. An example of the Langley plots is given in Fig. 15. The zero airmass intercepts from these data agree well (within 2%) to historical and other data taken later in March in Arizona. The good intercept agreement allows the use of the radiometer to make *instantaneous* optical depth measurements if the atmosphere is changing during the measurement period (Biggar et al. 1990).

On 8 March, the atmospheric conditions were not as good as the day before. There is some instability, which is shown in Fig. 16. The SeaWiFS calibration data were collected around 11:30 AM Pacific Standard Time (PST). The error bars are the uncertainty in transmittance due to the uncertainty in the zero airmass intercept.

The measurements of transmittance during the data collection period were successful. The optical depth due to Rayleigh scattering, aerosol scattering, and ozone absorption in the solar radiometer bands were determined. The optical depths for the same components in the SeaWiFS bands were then computed. A correction was also made for oxygen absorption in band 7 using `MODTRAN` (Berk et al. 1989). The results are presented in Table 16. The unshaded and shaded DC columns are the data collected by SeaWiFS while viewing the solar diffuser. The forward scatter DC is the correction needed due to the blocking of the forward scatter part of the aureole. The predicted in-flight DCs column is the calibration result expected in space from the solar diffuser.

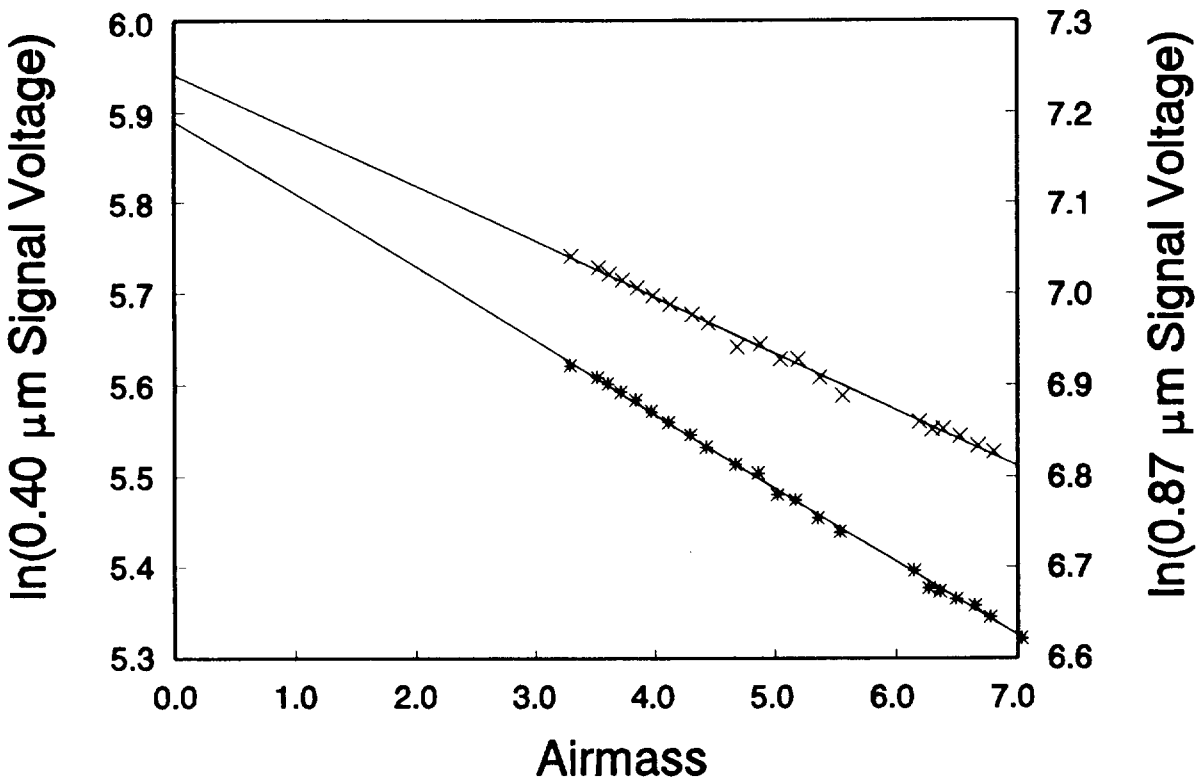

Fig. 15. Langley plot for 7 March 1993 at SBRC.

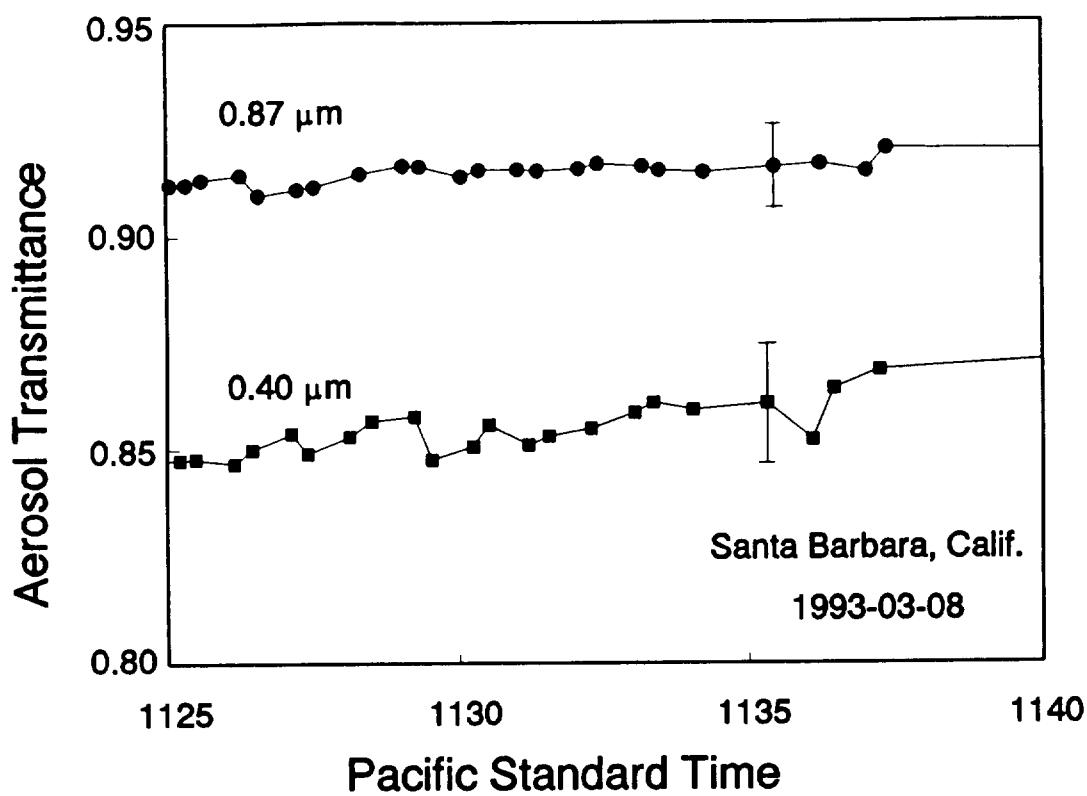

Fig. 16. Aerosol transmittance.

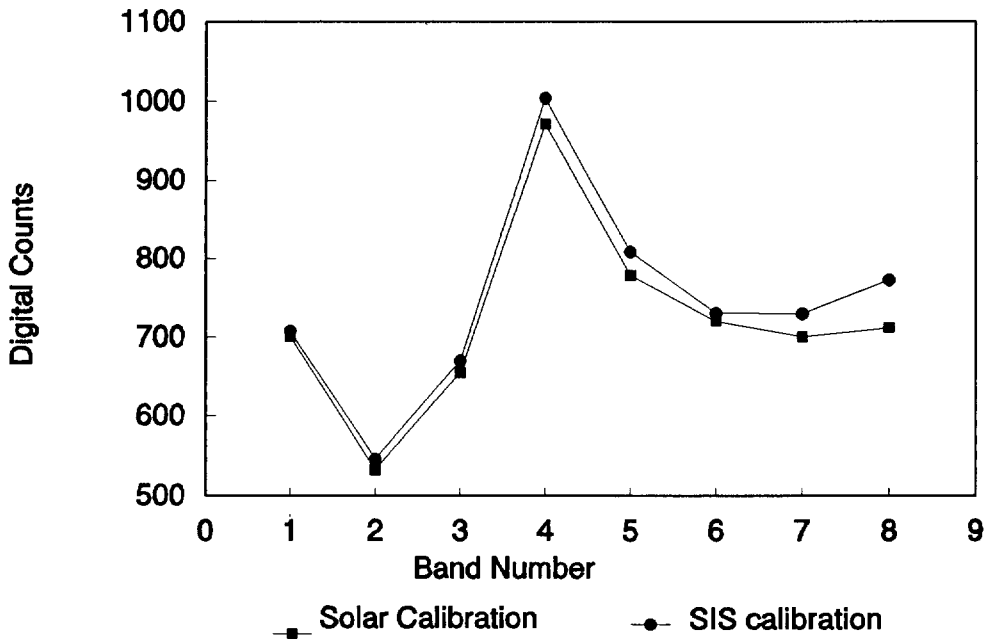

Fig. 17. Calibration comparison.

A preliminary attempt has been made to compare the solar diffuser calibration done with the sun to the laboratory calibration using the SBRC 100 cm integrating sphere. The solar spectrum from Iqbal (1983) was numerically integrated over the SeaWiFS bands, followed by application of the transmittance correction. The solar diffuser bidirectional reflectance distribution function and the laboratory counts per unit radiance calibration was then used to compute the last column in Table 16, the sphere-derived DCs. Figure 17 shows plots of the two calibrations where the sphere derived data have been corrected to correspond to the Earth-to-sun distance on 8 March 1993. The results are quite encouraging, as the difference is less than 4% for all bands except for band 8. The 7.7% difference in band 8 requires further analysis in order to determine the cause of this difference. (The presence of two Fraunhofer calcium lines are accounted for in the Iqbal (1983) data and residual water vapor is estimated to be less than a 1% effect.)

In reviewing these results, it should be realized that there are many error sources associated with both the predicted in-flight DCs and the sphere derived DCs. The former were addressed under error sources (Section 3.4) and the latter were addressed in the introduction. The two uncertainties that are the hardest to define are those of the solar exo-atmospheric spectral irradiance, as published by Iqbal (1983) from Neckel and Labs (1984) data, and those of the reference lamp used to calibrate the sphere. The results also depend strongly on the calibration of the diffuser and screen assembly—any uncertainties increase the uncertainty in the sphere derived results. In addition, the results presented here are from a single set of measurements. Time and weather restrictions prevented repeated measurements that would have provided a useful indication of the precision of the predicted in-flight DC data.

3.7 CONCLUSIONS

In this experiment, the SeaWiFS solar diffuser was calibrated using the sun. The results agree well with calibration results from the 100 cm spherical integrating source at SBRC. The sum of the uncertainties from each method is less than the difference in results for all bands except for band 8. The method appears promising for any sensor which uses a solar diffuser for calibration. The most interesting result, the actual DCs when the diffuser is illuminated by the sun while in orbit, will have to wait until after launch.

Acknowledgments

The authors from the University of Arizona wish to thank the SeaWiFS Project Office for support of this calibration work. R. Barnes was supported under National Aeronautics and Space Administration contract number NAS5-31540. The SeaWiFS instrument is being built by SBRC for Orbital Sciences Corporation in Virginia for a 1994 launch on the Pegasus booster.

Chapter 4

Spectral Radiance of the GSFC Integrating Sphere Using a Trap Detector

JAMES T. MCLEAN
NASA Goddard Space Flight Center, Greenbelt, Maryland

ABSTRACT

The GSFC 42 in (107 cm) diameter spherical integrator source is used to provide traceability in the optical *in situ* measurements made by different researchers who support the SeaWiFS program. The sphere's spectral radiance calibration is based on the irradiance standard lamp scale. The purpose of this study is to verify the radiance calibration of the sphere by using an absolute detector based scale which would be independent of the irradiance lamp scale. The experiment described herein shows that filtered absolute silicon photodetectors in a trap configuration can be used to verify the scale of spectral radiance of an integration sphere source.

4.1 INTRODUCTION

GSFC maintains a 42 in (107 cm) diameter spherical integrator source as a reference for the SeaWiFS calibration and validation radiation scale. This source is used to provide traceability in the optical *in situ* measurements made by different researchers who support the SeaWiFS program. This integrating sphere's spectral radiance calibration is based on the irradiance standard lamp scale. The procedure used to transfer the irradiance standard to the sphere output in terms of spectral radiance is described elsewhere (McLean and Guenther 1989). The purpose of this study is to verify the radiance calibration of the sphere by using an absolute detector based scale, which would be independent of the irradiance lamp scale.

A number of investigators have used filtered radiometers for radiometric measurements of lamps (Hughes 1982, Walker et al. 1991, and Corredera et al. 1990). Bruening (1987) used filtered absolute silicon photodetectors, the so-called quantum efficient device (QED), in a trap configuration (Zalewski and Duda 1983) to realize a scale of spectral irradiance. Techniques similar to the ones described by Bruening are followed.

4.2 EXPERIMENT DESCRIPTION

The laboratory setup is shown in Fig. 18. When making measurements with the equipment as shown, the signal produced by the detector package is a function of the filter transmittance, the response of the detector, and the optical power of the source (Bruening 1987). That is, $I(\lambda)$ is proportional to the power incident on the detector, or

$$d(I(\lambda)) = A_d\, E(\lambda)\, T(\lambda)\, R(\lambda)\, d(\lambda). \tag{41}$$

The irradiance, $E(\lambda)$, from the sphere is given by

$$E(\lambda) = \frac{\pi r_1^2}{r_1^2 + r_2^2 + d^2} L(\lambda), \tag{42}$$

Using these conventions, the detector current may be expressed as

$$I(\lambda) = \frac{A_d \pi r_1^2}{r_1^2 + r_2^2 + d^2} \int_{\lambda_1}^{\lambda_2} T(\lambda) R(\lambda)\, d\lambda, \tag{43}$$

which may be rewritten as,

$$L(\lambda_m) = \frac{I(\lambda_m)}{\kappa \int_{\lambda_1}^{\lambda_2} \frac{L(\lambda)}{L(\lambda_m)} T(\lambda) R(\lambda)\, d\lambda}, \tag{44}$$

where $L(\lambda_m)$ is the radiance of the sphere at the nominal peak wavelength of the filter. And,

$$\kappa = \frac{A_d \pi r_1^2}{r_1^2 + r_2^2 + d^2} \tag{45}$$

where A_d is the detector aperture area ($0.1\,\mathrm{cm}^2$), r_1 is the radius of the sphere aperture, r_2 is the radius of the receiving aperture (same as the detector aperture), d is the distance between the sphere aperture and the detector aperture, and λ_1 to λ_2 is the wavelength interval over which the filter transmits.

The ratio $L(\lambda)/L(\lambda_m)$ is a weighting function to account for the spectral variation of the source over the filter

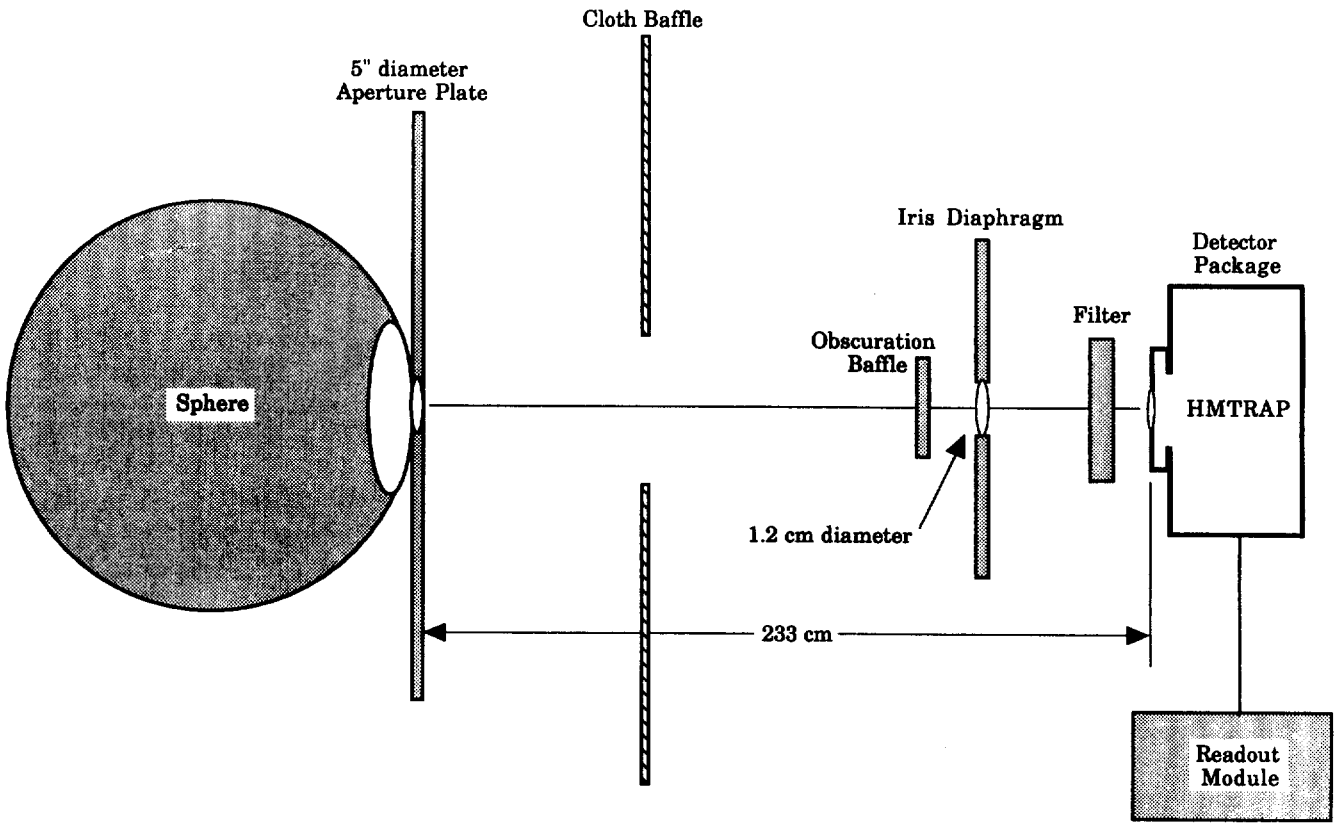

Fig. 18. Laboratory setup for making spectral radiance measurements of the GSFC integrating sphere.

passband where λ_m represent the nominal center wavelength of the filter. The effective center wavelength of each filter was calculated using:

$$E_{\text{eff}} = \frac{\int T(\lambda)\, d\lambda}{\int \lambda T(\lambda)\, d\lambda}. \tag{46}$$

However, the nominal values as specified by the manufacturer were used for this experiment.

The experimental procedure consisted of using an obscuration baffle to block the direct light from the sphere source and then record a background reading for a given filter-detector combination. The obscuration baffle was removed and the detector signal was recorded. This procedure was repeated for all 13 filters spanning the spectral range from 400–1,100 nm. The nominal passband for each filter is 25 nm. The data obtained is given in Table 17. Note, the integrated values in Table 14 are computed using the following formulation: $\sum \left(L(\lambda)/L_(\lambda_m)\right) T(\lambda)R(\lambda)\Delta\lambda$.

Table 17. The experimental procedure data obtained by using an obscuration baffle.

Filter	*Detector*	*Integrated*	*Radiance*	
[nm]	*Signal*	*Value*	*Calculated*	*Measured*
400	0.0026	4.63846	2.404	2.89
450	0.0090	6.07838	6.392	6.83
500	0.0179	6.33059	12.166	12.03
550	0.0277	6.51905	18.221	18.31
600	0.0521	9.01097	24.793	24.63
650	0.0458	6.39953	30.689	30.53
700	0.0537	6.44112	35.751	35.70
750	0.0805	8.62166	40.038	39.86
800	0.0977	10.00564	41.872	42.70
850	0.0850	8.23934	44.238	44.20
900	0.1280	12.48152	43.976	44.65
950	0.0855	8.47733	43.249	43.92
1000	0.0595	5.80379	43.962	43.76

4.3 CONCLUSIONS

The measured values in Table 17 are one of the data sets obtained for the sphere during the comparisons at SBRC. The data in Table 17 shows agreement better than 2% at all filter wavelengths except 400 nm and 450 nm. Further evaluation of the measurements at these two wavelengths showed that a rotation of the filters about an optical axis normal to the geometric center produced detector readings that varied as much as 6%. This effect, attributable to filter orientation, was discernible in all of the filters used in this experiment. However, the effect was much less than 1% in filters with wavelengths greater than 500 nm.

Polarization of the sphere source was ruled out by the introduction of a polarizing sheet in the optical path. Rotation of the polarizer produced minimum effect on the detector output. Non-uniformity of the filter is thought to contribute to this effect. This experiment shows that filtered absolute silicon photodetectors in a trap configuration can be used to verify the scale of spectral radiance of an integration sphere source.

The filters used were measured in October 1992 on a Perkin Elmer model Lambda 19 spectrophotometer.

Chapter 5

Evaluation of the Standard Data Formats HDF, netCDF, and CDF for SeaWiFS Operational Products

MICHAEL DARZI
FREDERICK S. PATT
JAMES K. FIRESTONE
BRIAN D. SCHIEBER
General Sciences Corporation, Laurel, Maryland

CHARLES R. MCCLAIN
NASA Goddard Space Flight Center, Greenbelt, Maryland

ABSTRACT

Three standard data formats have been evaluated for possible use in archiving and distributing SeaWiFS operational products. The three formats are HDF, netCDF, and CDF. Major technical criteria that were considered include machine independence, platforms supported, self description, subsampling, high-level specification language, and computer language interfaces. Practical considerations included acceptance by the scientific community, user support, cost, available tools, and availability of SeaWiFS related data and software. Although each format has certain strengths and deficiencies, CDF was found to hold significant overall advantages over the other two formats for SeaWiFS. Specific reasons and tradeoffs are discussed in this report which was submitted to the SeaWiFS Project in September 1992.

5.1 INTRODUCTION

The SeaWiFS Project would like to define a standard data format for its operational distribution products. The following report, submitted to the SeaWiFS Project in September 1992, describes the three formats that have been evaluated. A standard format permits the applications programmers and the data users to use the data without requiring knowledge of the actual physical storage format—a set of software routines associated with the format used to read or write the data in the standard's form. The technical and practical considerations of such a format include:

1. Technical considerations:
   a) machine independence,
   b) support of platform-native (i.e., a platform's internal data representation) formats,
   c) translation of foreign formats on input and output (I/O),
   d) platforms supported,
   e) self-describing,
   f) subsampling on input,
   g) support of multi-dimensional data,
   h) high-level specification of data structure,
   i) computer language interfaces,
   j) storage requirements, and
   k) availability of convenient library routines.
2. Practical considerations:
   a) acceptance by the scientific community,
   b) development and user support,
   c) documentation,
   d) cost,
   e) accompanying tools, and
   f) available data and software for SeaWiFS.

It should be noted that none of these items are absolutely required to permit distribution of data, but they are important in ensuring a certain level of convenience for the users of SeaWiFS products and in facilitating the Project's efforts in software development and data validation.

Three formats have been considered: HDF, developed by the University of Illinois's National Center for Supercomputer Applications (NCSA); netCDF, developed by the University Consortium for Atmospheric Research (UCAR) Unidata Project; and CDF, developed at GSFC. NetCDF is a derivative of an earlier version of CDF and therefore, these two formats possess many similarities.

5.2 RECOMMENDATIONS

Of the three formats evaluated, CDF offers the clearest advantages and no technical disadvantages with respect to its application to SeaWiFS products. Important advantages of CDF include:

1) translation of native formats across platforms on I/O,
2) current or planned availability on all platforms of interest to SeaWiFS,
3) capability to subsample on input,
4) data structure specification language,
5) good support and documentation, and
6) large amounts of data and software available for use by the Project.

The only negative with respect to CDF is the fact that it is not currently planned to be supported by the EOS Project directly, as for HDF, or indirectly, as for netCDF (Section 5.4.1).

HDF, on the other hand, suffers from serious disadvantages including:

a) no translation of native formats across platforms on I/O,
b) no port to NeXT computers,
c) awkward in terms of programming and suitability for SeaWiFS product contents,
d) no capability to subsample on input,
e) no data structure specification language, and
f) no integrated documentation manual for current release,

Because of these disadvantages, its use would entail a significant additional burden to the Project in terms of development effort, its ability to coordinate non-GSFC High-Resolution Picture Transmission (HRPT) stations' data, and, ultimately, in convenience to its end users. The only advantage of HDF over CDF is its designation by the EOS Project as the standard prototype format for DAAC products (Section 5.4.1).

NetCDF also suffers from serious disadvantages relative to CDF with respect to its applicability to SeaWiFS products. These disadvantages include:

- no support of native formats,
- no recognition of native formats across platforms,
- no port to NeXT computers.
- no capability to subsample on input,
- small development group, and
- poor tools.

However, netCDF shares some advantages with CDF over HDF, such as a greater suitability to SeaWiFS product contents (Sections 5.3.5 and 5.3.10) and a similar data structure specification language (5.3.8). Its only advantage over CDF is the fact that the EOS Project is funding a netCDF and HDF merger (Section 5.4.1), currently in progress. Such a merger, of course, does not eliminate the shared disadvantages from either of the merged formats.

5.3 TECHNICAL CONSIDERATIONS

5.3.1 Machine Independence

Machine independence implies that a data file created and used on one platform may be copied and used directly on another platform whose binary storage format is different. HDF, netCDF, and CDF all provide this capability by using a binary format based on External Data Representation (XDR). Some platforms, e.g., Sun, use XDR as their native format. However, on platforms whose binary format is not this machine independent form, the software automatically converts the data into the native form during read operations for processing; and it converts the data into the machine independent form during write operations for storage. The applications programmer and the user need not concern themselves with the binary format of the data. The extent of *independence* is defined by the platforms for which the format software has been ported (see Section 5.3.4).

The conversion to and from machine independent form results in a significant decrease of I/O speed (Section 5.3.2), but is extremely useful for data meant to be transferred, often across differing platforms. An alternative to *machine independence* is to provide utilities that convert data from one binary form to another, for use when data files are transferred to different platform types. This is not a convenient option when data are transferred often, since it is a time consuming process and may result in serious errors if the user neglects to do a conversion.

5.3.2 Support of Platform-Native Formats

As stated in the previous section, the conversion to and from machine independent form results in a significant decrease of I/O speed. This *overhead* may be avoided if the format software provides options for creating the data files in native formats. If the data files are stored on the platform on which they will be primarily used, it would obviously be most efficient to create them in that platform's native format. When transferred to a new platform type, they could then be converted to the machine independent format or to the native binary format of the new platform. Thus, this capability permits data to be distributed in machine independent form and be converted to native format for storage and use on users' individual machines.

This capability is especially important to the SeaWiFS Project since it would permit HRPT receiving stations around the world to rely on various platforms, including less expensive, but slower, International Business Machines

Table 18. Platforms and operating systems supported by each data format (as of this review).

Data Format	*Operating System*	*Computer Platform*
HDF	UNIX	SGI‡, Sun, DECstation, Cray, Alliant
	Other	PC, Macintosh, VAX†
netCDF	UNIX	SGI, Sun, DECstation, IBM RS/6000, HP 9000, Cray
	Other	VAX, PC, and OS/2, IBM mainframes, Macintosh
CDF	UNIX	SGI, Sun, DECstation, IBM RS/6000, HP 9000, Cray†
	Other	VAX, PC, NeXT, Macintosh†

† In progress or planned for next release.
‡ Silicon Graphics, Inc.

Personal Computer (IBM-PC) compatible computers for data capture and processing. Thus, it is important to have a standard format that performs reasonably well on such slower platforms when dealing with SeaWiFS' very large image files. The savings (20–50%, depending on data types, structure, and access speed) of this overhead is significant and may be essential to permit the effective use of slower platforms.

HDF and CDF support the use of native formats on all their platforms. The new version of HDF allows native formats for its Science Data Sets (SDS) as well as its *Vsets* (V is for *vertices*) construct. (*Vsets* allow relationships among SDS and other data types to be specified.) NetCDF provides no native format capability. As stated above, certain platforms use a native format based on XDR.

5.3.3 Translation of Foreign Formats

In addition to its native format capabilities, CDF software can also recognize the native formats of platforms other than the host platform, i.e., foreign formats, and convert them to that of the host for processing. This capability is again especially useful to the Project, since all non-GSFC HRPT stations which obtain SeaWiFS research licenses will be required to deliver data to the SeaWiFS Project or to other authorized users in the specified machine independent format upon request. Only CDF would allow them to store and efficiently use their data in native formats and also deliver those data without having to convert them on those stations' possibly slower machines. In essence, this capability makes the native format the machine independent format.

Users receiving those data would also not have to convert them to their respective native formats for storage unless choosing to do so for the sake of efficiency. The conversion of large amounts of data can be very time consuming and would not be worthwhile for data that are only to be used occasionally.

HDF software recognizes when data are stored in a different native format. The software issues an error in such cases but does not allow translation of the data. Since netCDF uses only XDR, even detection of foreign formats is not necessary.

5.3.4 Platforms Supported

The extent to which the software of each standard is supported at any one time on different platforms is difficult to ascertain. In theory, the software should be tested, and possibly modified, for each new version of each operating system. Moreover, different models from the same computer manufacturer may not be completely binary compatible, so that the inclusion of a manufacturer should not imply that the software has been validated on all its platform models. Given these caveats, the platforms claimed to be supported by the formats are listed in Table 18. In Table 18, VAX for HDF, and Cray and Macintosh for CDF, are in parentheses to indicate that those ports are in progress or are planned for the next release.

Platforms that are of special interest to the SeaWiFS project should be noted:

SGI is used by various elements of the Project and for the operational generation of SeaWiFS products;

NeXT is used by the field data processing system and by the CVT;

VAX is used by the field data processing system, the University of Miami group, the GSFC Laboratory for Hydrospheric Processes Ocean Color Group, and, to a lesser extent, by the SDPS element;

PCs are used by the field data processing system and by individual Project investigators, and are supported by SEAPAK, the oceanographic satellite and environmental data analysis package developed by the Ocean Color Group;

Macintosh is used by the field data processing system and by individual Project investigators; and

Cray is used by the Mission Operations and CVT elements.

In addition, personal computers, workstations, and minicomputers are all potential platforms for the HRPT receiving stations and therefore, are also of interest (see Sections 5.3.2 and 5.3.3).

Support for a variety of platforms, as is indicated for platform-independent formats, requires almost continual attention by the development group. Because of problems often encountered when using software with new operating system versions, the availability of development support (see Section 5.4.2 below) will be very important for SeaWiFS programmers over the life of the Project.

5.3.5 Self-Describing Data Formats

Data formats are considered self-describing when the files contain explicit information which allows their contents to be interpreted. This information includes details, such as the number of variables, the size of arrays, and data types, which permit the software to correctly access the data values. In addition, self-describing information includes metadata or information about the data contents that is more useful to the user. Metadata includes descriptive names, units, and comments.

Although all three candidate formats provide this self-description capability, the HDF provisions for such information are not nearly as convenient as those of netCDF or CDF. SeaWiFS products will require metadata in the form of characters, integers, real numbers, scalars, and arrays, as well as on a per-record basis. HDF requires attributes to be associated with their variables via pointers. Array metadata would have to be declared as separate SDS associated implicitly with their corresponding variables in a SDS file, or use Vsets to make this association explicit, since they allow additional relational information to be defined. (See also Sections 5.3.2 and 5.3.10). Of course, metadata can always be written as American Standard Code for Information Interchange (ASCII) strings within HDF annotation fields. However, this is not a satisfactory solution since ingest software would have to parse the string in order to find the labels and read in the values.

5.3.6 Subsampling on Input

CDF is the only format that allows a programmer to specify a pixel subsampling rate upon input. This capability is particularly useful for SeaWiFS' very large image files (100 Mbytes or more) in that it allows, for example, the direct display of an entire image at lower resolution. The less convenient, and also less efficient, alternative would be to read the file in small sections in order to accommodate a computer's memory constraints while subsampling into smaller arrays to effect the lower resolution.

5.3.7 Support of Multidimensional Data

All three formats allow variables of differing dimensions to be represented in the same data set. That is, HDF, netCDF, and CDF support this type of multi-dimensional data representation.

5.3.8 High-Level Data Structure

CDF and netCDF support a high-level *language* that can describe a data set's structure and list its metadata. CDF and netCDF provide utilities that can generate the specifications for a given data set and can create a data set skeleton from a given specification. This capability provides, for example, a convenient way for a user to create a data set structure and input its metadata by writing the specifications in the proper syntax, or by editing the specifications of an existing data set. Moreover, it allows the specifications of a data set (its *layout*) to be communicated among users in a concise and unambiguous manner.

HDF does not support this type of data set specification. For a large development effort such as the SDPS, the lack of this capability is a serious handicap.

5.3.9 Computer Language Interfaces

All three formats support an interface for C to their library routines. HDF, netCDF, and CDF also support a FORTRAN interface to their library routines.

5.3.10 Convenient Library Routines

Based on prior programming experience with all three formats, CDF appears to have the most convenient set of library routines for programming, followed closely by netCDF. HDF tends to require, for example, many more calls to various subroutines in order to perform a similar task than CDF or netCDF. Moreover, HDF requires additional HDF-specific *tags* for explicitly defining variable types.

The ease-of-use of HDF suffers from the fact that the format was originally designed to represent only raster images in 8- and 24-bit pixels. The SDS and Vsets constructs were added subsequently to support other data types, such as real numbers, and other data structures. As examples, the SeaWiFS requirements to store multiple data types in level-3 products, and multiple bands or parameter fields within the same data sets for all its products, can best be handled in HDF via its Vsets construct. This representation is more awkward and tedious than for CDF and netCDF, in that the user must explicitly specify the relationships of the bands to the underlying grid or the geocoordinate lattice.

The complexity of the various HDF data structures is of additional concern to SeaWiFS because of the HRPT stations. These stations may not have the resources, in terms of expertise in data formats or personnel, for software development. As a result, there may be a reluctance on their part to use a format that is less directly suited to their data requirements. Because the SeaWiFS Project is responsible for providing support to these stations, any

additional support required by these stations for development of software to input, output, or transfer data translates into greater demands on the resources available to the Project.

5.3.11 Storage Requirements

The storage space overhead associated with each of the formats is essentially the same and is usually trivial. The amount of overhead depends on the amount of metadata and the type and amount of actual data. For SeaWiFS products, this overhead will be about two percent of the total data storage requirements.

Although none of the formats provide a data compression capability, such a capability could be very useful for large data set files, such as SeaWiFS products. Of interest, therefore, are the plans of the HDF and CDF development teams to implement this capability. Depending on the exact methodology, data compression would be useful to SeaWiFS for distribution purposes, and for the added convenience of storing occasionally used data in compressed form.

5.4 PRACTICAL CONSIDERATIONS

5.4.1 Acceptance of a Standard

The acceptance of a standard data format by the scientific community is important for several reasons:

1. It helps ensure that political and financial support for the format and its development effort will continue, evolving with new features and supporting new platforms and operating systems.
2. It increases convenience for users who are familiar with the standard and have obtained or developed software based on that standard.
3. It allows relevant data using the same format to be analyzed using essentially the same software, again increasing user convenience.
4. It results in support of that format by commercial companies for their analysis packages, thus greatly increasing the availability of useful software to users of that format.

It should be noted that it is very difficult to gauge the extent to which formats are actively being used by the outside communities and to judge the level of satisfaction of the users. Such a survey would obviously be very useful.

HDF has been selected as the standard format by the EOSDIS for use by the DAACs. The format appears to be widely used by researchers, especially for raster image-type data for which it was originally designed. NetCDF also appears to be widely used, especially by the meteorological community. In addition, NCSA has been funded by the National Science Foundation (NSF) and EOS to incorporate the netCDF library into the HDF library, allowing users who normally use HDF to input netCDF data sets and, presumably, convert them into HDF if desired.

At this time, it is not clear how:

a) all the attributes and other metadata are handled and converted in the merged HDF-netCDF format;

b) whether or not the netCDF data must follow a *standard* structure or, conversely, how *generic* the code must be; and

c) if there is any overhead associated with inputting netCDF versus HDF.

If no overhead is involved, there would be no need to convert them, since there would be no disadvantage to remaining as netCDF data. NCSA is also planning to allow netCDF software to input HDF data, a much more difficult task, as the next part of this effort.

It should be noted here that merging different format standards is not necessarily a good idea, since a desirable attribute of any format is that it be easy to use. The forcing of formats that differ fundamentally in their structure into one *megaformat* may result in a standard that is too big and complicated to understand and use. Also, a merger does not eliminate disadvantages shared by both formats with respect to the SeaWiFS Project, as discussed in this report. Finally, such a merger adds additional constraints on each format development group, forcing them to march in lockstep with respect to their support of new features or operating systems. Thus, a merger may hinder a format's ability to overcome its current disadvantages as well as keep up with the ever changing computing environment. In this sense, the benefits of merging netCDF with HDF remain to be seen.

CDF is also widely used by the meteorological community. The CDF exposure to this group is primarily via the NASA Climate Data System (NCDS), whose users number in the hundreds. Over two thousand compact disk-read only memory (CD-ROM) diskettes containing meteorological and atmospheric constituent data in CDF form were produced and distributed by the Goddard DAAC at the recent world conference on the global environment in Rio de Janeiro, Brazil. CDF has been selected as the standard format for the prototype Tropical Rainfall Measuring Mission (TRMM) data system and for the data generated from the International Solar Terrestrial Program (ISTP) satellites. Although the large ISTP planetary science community is unlikely to be interested in any Earth science data, their selection does help ensure that adequate funding to the CDF group will continue for at least the next decade.

NCSA will also look into the possibility of a merger of CDF and HDF similar to that of netCDF and HDF. The CDF development group has expressed an interest in such an effort although there are no definite plans or funding

for this at this time. Because of the design similarities between CDF and netCDF, the effort required to merge each with HDF would also be expected to be similar.

5.4.2 Development and User Support

Development support is support for the development of the format software. This includes:

i) timely correction and notification of errors;

ii) continued testing for ports to new platforms or new operating systems (see Section 5.3.4);

iii) the continued evolution of the software, especially to incorporate new features found to be desirable or necessary; and

iv) the improvement and updating of documentation.

User support includes response to queries regarding programming with the software and regarding the efficient implementation of unusual data.

A primary indicator of both types of support is the size of the development group for each format. HDF appears to have the largest group, with 4–8 people (including student personnel) working on the project. A substantial portion of this effort involves the development of display, analysis, and data management tools associated with HDF (Section 5.4.5), and another part of this effort involves the merger of netCDF and HDF. The EOS use of the standard ensures that support for DAAC product developers will be adequate. Furthermore, NCSA has expressed, via the EOS Project, a desire to accommodate requirements of such DAAC product developers.

The CDF team is comprised of three to four people. Members of the SeaWiFS Calibration and Validation element and the Laboratory for Hydrospheric Processes' Ocean Color Group have worked with the CDF team for a number of years. The interaction has been the result of an ongoing collaboration with the NCDS which has been funded for the past five years. The Ocean Color Group has found the response to be very fast and the quality of support to be excellent. Moreover, they have already incorporated features suggested by the Ocean Color Group in new versions of their software. A major advantage to the Project of the CDF team in this regard is its physical location at GSFC, permitting person-to-person discussions of problems.

Finally, the netCDF group includes the equivalent of less than one person on their development effort. Of the three format groups, netCDF seems to rely the most on outside users performing ports and providing public domain software. Such use of third-party software increases the likelihood that both the quality of the products and support for these products will not be uniform. NetCDF does, however, have a very active electronic mail group which provides a convenient forum for the exchange of useful information.

5.4.3 Documentation

A comparison of the documentation associated with each format indicates that the current documentation for CDF is the best, followed closely by that for netCDF. The documentation for HDF is outdated, poorly organized, and difficult to follow and understand. The new release of HDF was not accompanied with integrated documentation; its new features are described in a series of updates to the documentation of the previous release (dated 1990).

5.4.4 Cost

All software packages and documentation for the three formats are available at little or no cost. That is, there are minimal charges involved in the acquisition of the HDF, netCDF, and CDF software libraries and associated documents.

5.4.5 Accompanying Tools

HDF appears to have the most comprehensive set of software tools for that format, including graphical display of data, data analysis, and data management. However, most of these do not support Vsets, which, as discussed previously, would be useful to SeaWiFS products (see Sections 5.4.2 and 5.4.10). CDF has a beta version of a graphical display tool, as well as a well developed interactive tool for ASCII examination of the data. The netCDF group has not developed good comparable tools, but again relies on outside users to make such tools available to the community.

It should be noted that, for the SeaWiFS Project, the availability of accompanying tools is not an important consideration since more powerful, customized tools will be developed using the commercial data analysis package called Interactive Data Language (IDL). The current beta version of IDL supports netCDF and CDF as input data formats and will have similar support for HDF within a month. Therefore, the availability of accompanying tools serves mainly as a convenience to SeaWiFS' end users. However, since IDL and a number of other commercial analysis packages support or plan to support these formats, and since these packages are becoming quite popular, many end users are also likely to prefer them for building customized tools.

5.4.6 Availability to the Project

As a result of a March 1992 decision to use netCDF, some effort has been expended by the Project to implement the netCDF software, create test data sets on the SGI and PC platforms, and to develop a simple display program for the SGI. The extent of the effort was on the order of a few man-weeks. This earlier decision to use netCDF was based primarily on the judgement that it was more suitable for SeaWiFS products than either HDF or CDF. At the time, for example, HDF did not support the storage of two-byte

integers, in addition to not having a data structure specification language (Section 5.3.8). For CDF, the available version did not directly support variables of differing dimensionality (Section 5.3.9).

Previous efforts by the Ocean Color Group include about five man-years developing software for using CDF data and another five man-years for the creation of over 15 Gbytes of ocean related, CDF data sets (see Appendix). Some of this software and data are directly applicable to the Calibration and Validation effort. The use of the CDF format by SeaWiFS would eliminate the very resource consuming task of converting these data into another format and modifying the software accordingly for use by the Project.

No effort in development of software or creation of data sets has been expended by the Project for HDF. However, some effort (several man-days) has been spent on evaluating HDF documentation, attending demonstrations, and discussing its capabilities with others who have used the format.

Chapter 6

The Generation of CZCS Ancillary Data Sets for Simulated SeaWiFS Processing

BRIAN D. SCHIEBER
JAMES K. FIRESTONE
General Sciences Corporation, Laurel, Maryland

ABSTRACT

The SeaWiFS development effort includes simulated data processing using CZCS data files for the three-year time period of November 1978 through December 1981. Ancillary meteorological data products of total ozone, and surface values of zonal and meridional wind speed, atmospheric pressure, and relative humidity will be used for producing simulated level-2 CZCS (derived ocean color) products as a test of the SeaWiFS processing system. These data files are provided from the Goddard DAAC and TOMS project archives and converted to the SeaWiFS data format for subsequent processing. The calibration and validation element has developed procedures and software to process the CZCS ancillary data in a manner that simulates the processing which will occur once SeaWiFS is operational. The data are stored as HDF files for each of the ancillary parameters. This chapter describes the methods used for the generation of ancillary files from the CZCS era for use in simulating the SDPS.

6.1 INTRODUCTION

The processing of CZCS data from level-1 (calibrated radiances) to level-2 (derived products) requires five ancillary fields:

a) total ozone;
b) surface values of zonal (east-west) wind speed;
c) surface values of meridional (north-south) wind speed;
d) surface atmospheric pressure; and
e) relative humidity.

All of these fields are incorporated into the atmospheric correction algorithm. This processing will be used to simulate the creation of SeaWiFS data, and will be run for the period 1978–81. The ancillary data was compiled from several sources, all distributed by the Goddard DAAC.

6.2 METEOROLOGICAL DATA

The ancillary meteorological data are currently provided by the DAAC for zonal and meridional wind speed, surface pressure, and relative humidity data sets. The data files are products from several different research projects for the three year time period. The US Navy FNOC provided wind components and surface pressure data. Three data files were used to generate the relative humidity HDF data (University of Illinois 1989 and 1993). These files, obtained from the ECMWF, are described below. For the period 1978–79, a data set from the First Global Atmospheric Research Program (GARP) Global Experiment (FGGE) was used. Years 1980–81 used ECMWF 00 GMT and 12 GMT data files. A description of the data parameters, their ranges, and processing programs is shown in Fig. 19.

6.3 OZONE DATA SET

Total ozone data were provided by the Ozone Processing Team (OPT) at GSFC available on CD-ROM. The data consisted of daily ASCII files representing averaged gridded arrays. The data were derived from the gridded TOMS (GRIDTOMS) orbital data set, and were global, with a resolution of 1.0° in latitude by 1.25° in longitude (i.e., 180 latitude points by 288 longitude points). Since the original grid cells were equal in area, the OPT used an interpolation scheme for latitudes higher than 50° latitude, i.e., poleward, to create an equal-angle grid of constant 1.25° longitude resolution.

6.4 DATA FILE GENERATION

All data processing of meteorological and ozone data were performed on SGI UNIX workstations. NRT meteorological data were downloaded from the DAAC using the electronic File Transfer Protocol (FTP). TOMS ozone data, on CD-ROMs, were requested and received from the TOMS OPT.

Table 19. Software programs and languages written for storing and displaying ancillary data files.

Name	*Language*	*Input*	*Output*
CDFCVT	C	Platform specific CDF	Network compatible CDF§
WPHCZCS	C	Network compatible CDF†§	HDF†
RDGRID	FORTRAN	ASCII TOMS	Ozone array for O3NRT
O3NRT	C	Ozone array from RDGRID	Ozone HDF

† Contents are comprised of zonal and meridional wind speed, pressure, and relative humidity.
§ Note that *Network compatible CDF* is different from *netCDF*.

Data Type	Windspeed	Surface Pressure	Relative Humidity	Ozone
Source	Goddard DAAC	Goddard DAAC	Goddard DAAC	TOMS Project
Temporal Range(s)	Full Range: 12/1/78 - 12/31/81	Full Range: 12/1/78 - 12/31/81	12/01/78 - 12/01/79 FGGE_3B 01/01/80 - 12/31/81 ECMWF_00Z 01/01/80 - 12/31/81 ECMWF_12Z	Full Range: 12/1/78 - 12/31/81
Temporal Resolution	12 hour	12 hour	12 hour	daily
Spatial Range	Global	Global	Global	Global
Spatial Res. (Lat x Lon)	2.5 x 2.5	2.5 x 2.5	1.875 x 1.875 FGGE_3B 2.5 x 2.5 ECMWF_00Z 2.5 x 2.5 ECMWF_12Z	1.0 x 1.25
Format	Vax encoded CDF	Vax encoded CDF	"Network" CDF	TOMS ASCII
Filename(s)	fnoc_anl_glob_sfc_78 fnoc_anl_glob_sfc_79 fnoc_anl_glob_sfc_80 fnoc_anl_glob_sfc_81	fnoc_anl_glob_sfc_78 fnoc_anl_glob_sfc_79 fnoc_anl_glob_sfc_80 fnoc_anl_glob_sfc_81	FGGE_3B ECMWF_00Z_ANLY ECMWF_12Z_ANLY	dYYMMDD.dat
Parameter Name(s)	WIND_U & WIND_V -> WINDSPEED	SURF_PRESS	HUMID_RH	OZONE
Program(s) Used	CDFCVT WPHCZCS	CDFCVT WPHCZCS	CDFREGRID.PRO (regrid FGGE_3B) WPHCZCS	RDGRID.FOR O3NRT

Fig. 19. Specifications developed for storage of ancillary data in SeaWiFS.

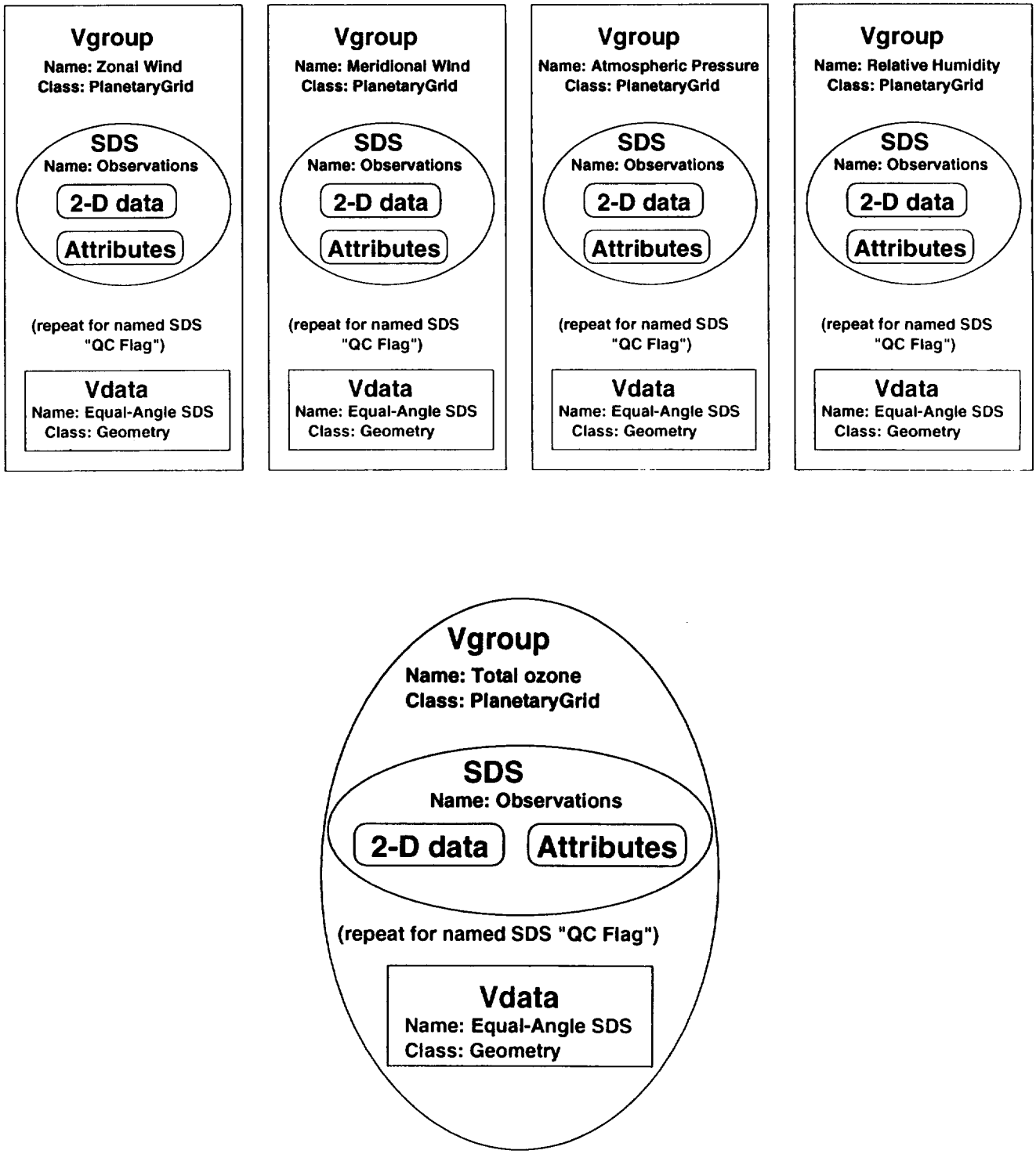

Fig. 20. Specifications for the storage of CZCS era and SeaWiFS near-real time ancillary data in HDF. The top panel displays meteorological data and the bottom panel shows ozone data.

DAAC archive data sets were provided in NASA CDF, and were VAX encoded files (National Space Science Data Center 1991). The UNIX CDF program, `CDFCVT`, converted the data to a *network* UNIX compatible format, and translated the data from FORTRAN *column major* order to C *row major* order. Relative humidity data from the FGGE research project required regridding, using IDL, to match the $2.5° \times 2.5°$ (latitude by longitude) gridding in the rest of the meteorological files.

The C program, `WPHCZCS`, processed the converted CDF files, which contained wind, pressure, and humidity data from 1978–81, to HDF files with the SeaWiFS specifications (Fig. 20 [top]). Metadata to describe the data sets are also included HDF output products. Similarly, the C program, `O3NRT`, produced SeaWiFS HDF files containing ASCII TOMS ozone data, also from 1978–81 (Fig. 20 [bottom]) Note that the Vdata for humidity differs from the others when FGGE data is the source (used for 1978–79), since the grid differs.

The program, `O3NRT`, will be used for NRT production of ozone HDF files by the SeaWiFS Project, since the input format is the same as for the 1978–81 period. A FORTRAN routine, `RDGRID`, was provided by the TOMS Project to produce data arrays used within `O3NRT`. The software processing routines are summarized in Table 19.

Note that the HDF specification is consistent with the recommendations of the GSFC EOSDIS Project, while the HDF file-level annotation conforms to the metadata submission guidelines of the Goddard DAAC (Lynnes et al. 1992).

Chapter 7

The Generation of SeaWiFS Near-Real Time Ancillary Data Files

BRIAN D. SCHIEBER
JAMES K. FIRESTONE
General Sciences Corporation, Laurel, MD

ABSTRACT

In the SDPS, NRT ancillary data files will be used for producing level-2, i.e., derived ocean color, products. In addition to a data file for total column ozone, separate files will contain surface value data for: zonal and meridional wind speeds, atmospheric pressure, and relative humidity. These ancillary data files are obtained from several sources, with additional backup sources identified for each data type should the primary data source become unavailable. The ancillary data files will be an integral part of the SDPS. The Calibration and Validation element for SeaWiFS has developed procedures and software to acquire and format the NRT data. The ancillary parameters will be stored as data in HDF files. This chapter describes the methods used for the generation of NRT files.

7.1 INTRODUCTION

The processing of SeaWiFS data from level-1 to level-2 requires five ancillary data fields:

a) total column ozone,
b) surface values of zonal (east-west) wind speed,
c) surface values of meridional (north-south) wind speed,
d) surface atmospheric pressure, and
e) relative humidity.

All five atmospheric variables are incorporated into the atmospheric correction algorithm. Generation of SeaWiFS refined products involves a process of data acquisition, storage, and quality control (QC) of NRT data. For generation of the Performance Assessment (*quick look*) product, climatological data will be used (Firestone and Schieber 1994).

7.2 METEOROLOGICAL DATA

NRT meteorological data is currently provided by the NOAA NMC. A secondary source for meteorological data is FNOC, should the primary NOAA source be unavailable. The NMC data are provided in 6-hour increments in the gridded binary (GRIB) format (Stackpole 1990). GRIB files are unpacked to simple binary arrays for each of the desired meteorological parameters (zonal and meridional wind speed, surface pressure, and relative humidity). The binary arrays are then processed to produce HDF data products (Fig. 20).

7.3 OZONE DATA SET

Total column ozone is provided by the OPT at GSFC. The data consists of daily ASCII files representing averaged gridded arrays. The data are derived from the GRID-TOMS orbital data set, and are global with a resolution of $1.0° \times 1.25°$ (latitude by longitude). Since the original grid cells were equal in area, the OPT used an interpolation scheme poleward of 50° latitude to create an equal-angle grid of constant 1.25° longitude resolution (National Space Science Data Center 1993). A secondary source for ozone data is the twice-daily set of soundings from the NOAA Television Infrared Observation Satellite (TIROS) Operational Vertical Sounder (TOVS) instrument.

7.4 DATA FILE GENERATION

All data processing of meteorological and ozone data are performed on SGI UNIX workstations. The data are kept in a central repository in the Data Assimilation Office (DAO) of the GSFC Laboratory for Atmospheres, as part of an agreement between NMC and the GSFC Earth Sciences Directorate. NRT meteorological and TOVS ozone data are downloaded from NOAA into the GSFC repository using the electronic FTP in an automated procedure. The meteorological data are stored in GRIB format, and the TOVS ozone data in the National Environmental Satellite Data Information Service (NESDIS) sounding products format (Kidwell 1991). The DAO performs quality control on the TOVS data to remove duplicate soundings, then

Table 20. Software programs and languages written for storing and displaying ancillary data files.

Name	*Language*	*Input*	*Output*
WPHNRT	C	Unpacked GRIB†	HDF†
GRIDTOVS	FORTRAN	NESDIS TOVS profiles	ASCII TOVS grid
O3NRT	C	ASCII TOMS or TOVS	Ozone HDF

† Contents are comprised of zonal and meridional wind speed, pressure, and relative humidity.

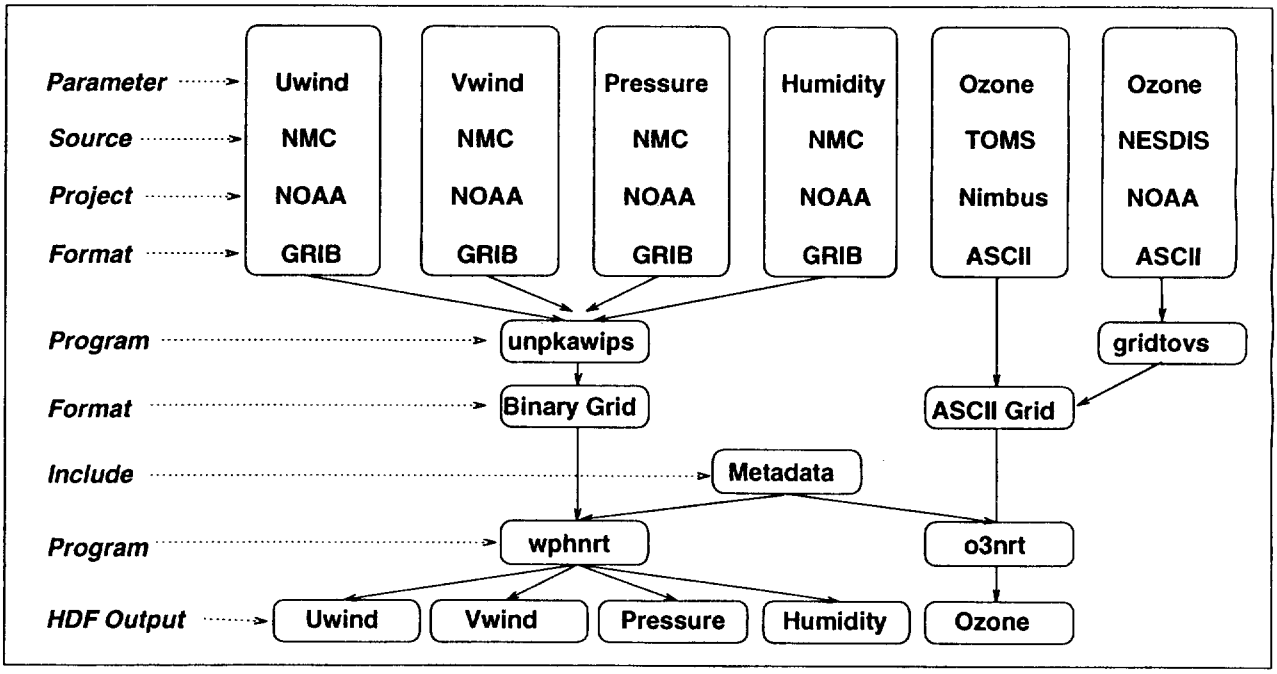

Fig. 21. Schematic for the generation of ancillary data used in the SDPS.

rewrites the files twice daily in the NESDIS format. The repository's disk is made accessible to the SDPS through a remote mount, using the Network File System (NFS). TOMS ozone data are directly downloaded in ASCII format, using FTP, from the OPT.

The FORTRAN program, UNPKAWIPS.X, is provided by NMC to unpack the GRIB meteorological data files to simple gridded binary arrays. The C program, WPHNRT, processed the unpacked GRIB wind, pressure, and humidity data files to generate the SeaWiFS HDF file (Table 20). WPHNRT employed the HDF libraries (University of Illinois 1993) and general specifications (University of Illinois 1989) developed by the NCSA.

The process of unpacking GRIB files, generating HDF files, and cleaning up temporary files is accomplished using a simple UNIX C-Shell command file (Table 20). Within WPHNRT, surface pressure is converted from Pascals to millibars. Metadata describing the data sets are also included in the HDF output products. Similarly, the program O3NRT is used to convert TOMS ozone values or TOVS NRT ozone values from ASCII format to the SeaWiFS HDF format. Note that for the TOVS data, the ASCII ozone values are generated by an additional program, GRIDTOVS, which objectively analyzes two consecutive 12-hour TOVS sounding files to form a representative 24-hour grid every 12 hours. Figure 21 represents the data types and the processing steps involved in the production of the final HDF data products. Table 20 summarizes the inputs and outputs for the programs used in the processing stream.

All generated HDF files conform to the specification de-

veloped by the Project for storage of these ancillary data (Fig. 20). Note that these specifications are consistent with the recommendations of the EOSDIS project, while the HDF global and SDS-level attributes conform to the metadata submission guidelines of the Goddard DAAC (Lynnes et al. 1992). These considerations will allow the quality controlled versions of the NRT data to be made publically available. The HDF files consist of separate *Vgroups* for each data parameter. Each *Vgroup* contains a global latitude-longitude grid stored in an SDS with its associated descriptive attributes. In addition, there are global attributes that describe metadata at the file level, and a geometry *Vdata* which defines the physical characteristics of the data grid. Note that *Vgroup* and *Vdata* are HDF terms for data organization in Vsets (University of Illinois 1990).

Chapter 8

An Evaluation of Surface Wind Products for Use in SeaWiFS

JAMES K. FIRESTONE
ROBERT H. WOODWARD
General Sciences Corporation, Laurel, Maryland

CHARLES R. MCCLAIN
Goddard Space Flight Center
Greenbelt, Maryland

ABSTRACT

This study statistically compared remotely sensed and modelled surface wind speeds from several sources with available ground truth, in order to provide a recommendation for which source to use in the SDPS. Model wind field sources included the FNOC, ECMWF, and NMC. Remotely sensed wind speed fields came from the SSM/I, and ground truth sources included seven fixed moorings provided by NDBC, and the TOGA-TAO Project. A temporal and spatial match between the large scale and *in situ* winds was completed, using input data for the period 1982–90. An additional matchup was run to compare mooring winds with 1,000 mb and boundary layer winds from NMC, for 1990. A suite of software applications for reading and merging the various data sets used in the analysis was developed as part of the Laboratory for Hydrospheric Processes' VAX SEAPAK package. Scatterplots comparing each of the large scale wind sources to the seven moorings were generated, using commercial PC software, and square of the correlation coefficient (R^2) values, slopes and number of points for each plot were noted. This analysis indicated that SSM/I had the highest R^2 values of any of the large scale wind fields. Since they are gridded products, NMC and FNOC are the suggested wind field sources, and mechanisms are in place to automatically transfer them to GSFC automatically. The new versions of these models incorporate SSM/I data in their production.

8.1 INTRODUCTION

The SDPS requires surface wind speed as one of its ancillary parameters, to be used by the atmospheric correction algorithms, in both sun glint flag (McClain and Yeh 1994) and correction schemes, and for surface foam reflectance corrections. In order to select the most accurate wind product possible, a study comparing the statistical correlations of data from several global wind data sets with wind speed and direction data from fixed ocean moorings (as ground truth) was made. The study facilitated the production of software routines for ingesting various types of ocean mooring data, as well as matching the mooring and global wind data temporally and spatially (Woodward et al. 1992). These software routines were included in the VAX version of SEAPAK, a software package consisting of over 200 programs for processing ocean color and related ancillary data, developed for the GSFC Laboratory for Hydrospheric Processes (Darzi et al. 1989, McClain et al. 1991a and 1991b). The end result of the data analysis portion of this study allows for a recommendation to the SeaWiFS Project on which wind product would be the most accurate for incorporation into level-2 algorithms.

8.2 DATA SETS

A combination of four model-generated gridded wind data sets, one remotely sensed wind data set, and data from seven fixed ocean moorings were used in this study. The ocean moorings were located in the northern and equatorial Pacific Ocean, the Gulf of Mexico, and the North Atlantic Ocean (Fig. 22). The sampling period for the global wind data sets commenced in 1982, and was tied to the availability of the NDBC moorings from the National Oceanographic Data Center (NODC) (National Oceanic and Atmospheric Administration 1990, Meindl and Hamilton 1992). All of the gridded global wind data sets were stored in NASA CDF and were originally generated by the staff of NCDS, which is now the Goddard DAAC (Olsen and McClain 1992). The CDF data sets are part of a large archive of ancillary environmental data accessible for analysis by VAX SEAPAK (Firestone et al. 1990).

Table 21. Characteristics of wind data sets used in analysis.

Name	*Level*	*Spatial Coverage*	*Resolution Spatial (Temporal)*
FNOC	Marine layer	Global	2.5°×2.5°(12 hr)
ECMWF	1,000 mb	Global	2.5°×2.5°(12 hr)
TOGA-ECMWF	Surface	Global	2.5°×2.5°(12 hr)
NMC	1,000 mb	Global	2.5°×2.5°(12 hr)
SSM/I	Surface	Global	Non-gridded†
NDBC	Ocean moorings	23°–57° N 69°–180° W	5 buoys‡
TOGA-TAO	Ocean moorings	2° N, 165° E 2° N, 110° W	2 buoys§

† Satellite swath data
‡ Atlantic Ocean, Gulf of Mexico, Pacific Ocean
§ Equatorial Pacific Ocean

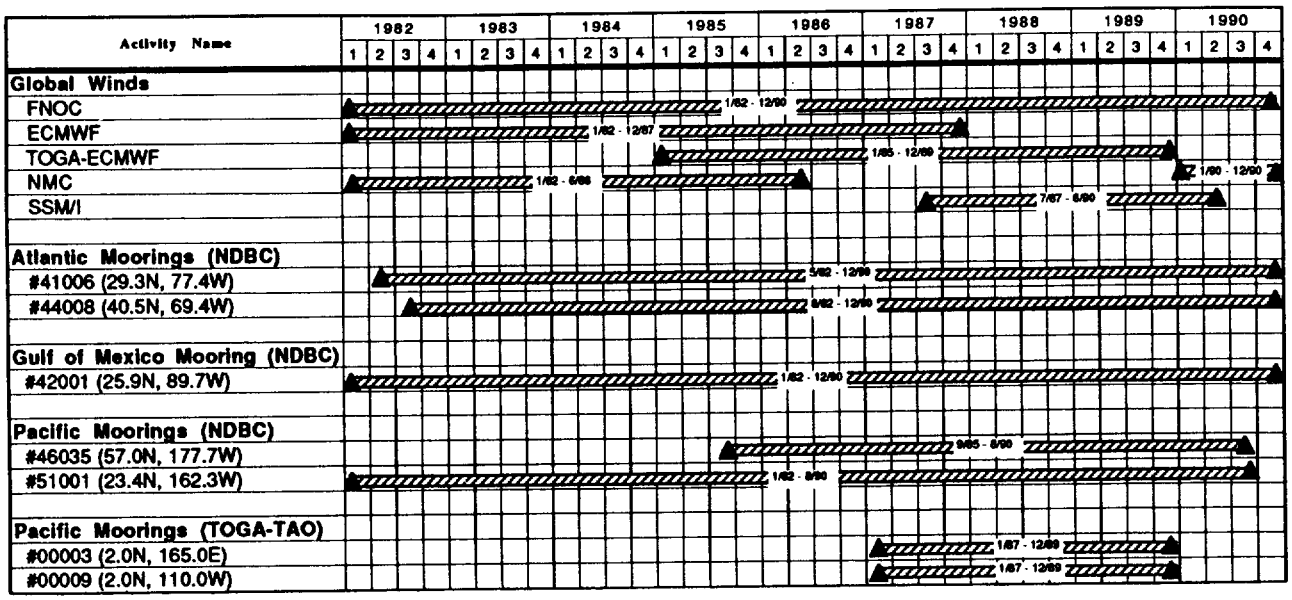

Fig. 22. Temporal coverage of data sets used in the study.

The modeling centers providing the gridded data to NASA were: FNOC, ECMWF, and NMC. The TOGA-ECMWF data set represented special runs of the ECMWF model specifically for the TOGA Experiment (National Research Council 1990). Data from the SSM/I instrument was produced by F. Wentz and the group at Remote Sensing Systems, Inc. (RSS), and provided by the NASA Jet Propulsion Laboratory (JPL) DAAC on 9-track magnetic tapes. Table 21 summarizes the temporal and spatial characteristics of the various global wind data sets.

The mooring data was provided from two sources—NODC and the TOGA-TAO Project (Hayes et al. 1991) at the NOAA Pacific Marine Environmental Laboratory (PMEL). The first group, labeled "Pacific Moorings" in Fig. 22, along with those labeled "Atlantic Moorings," and "Gulf of Mexico," were from NDBC, while the second group of "Pacific Moorings" were from TOGA-TAO. The seven moorings used in the analysis were chosen from an original group of 72 NDBC and 20 TOGA-TAO moorings in this general region (Fig. 23). The seven moorings chosen possessed the longest available time series of data from the clusters of moorings considered. Taken together, the seven moorings encompass a diverse set of climatological wind regimes including tropical, mid-latitude, high latitude, coastal, and mid-ocean regimes.

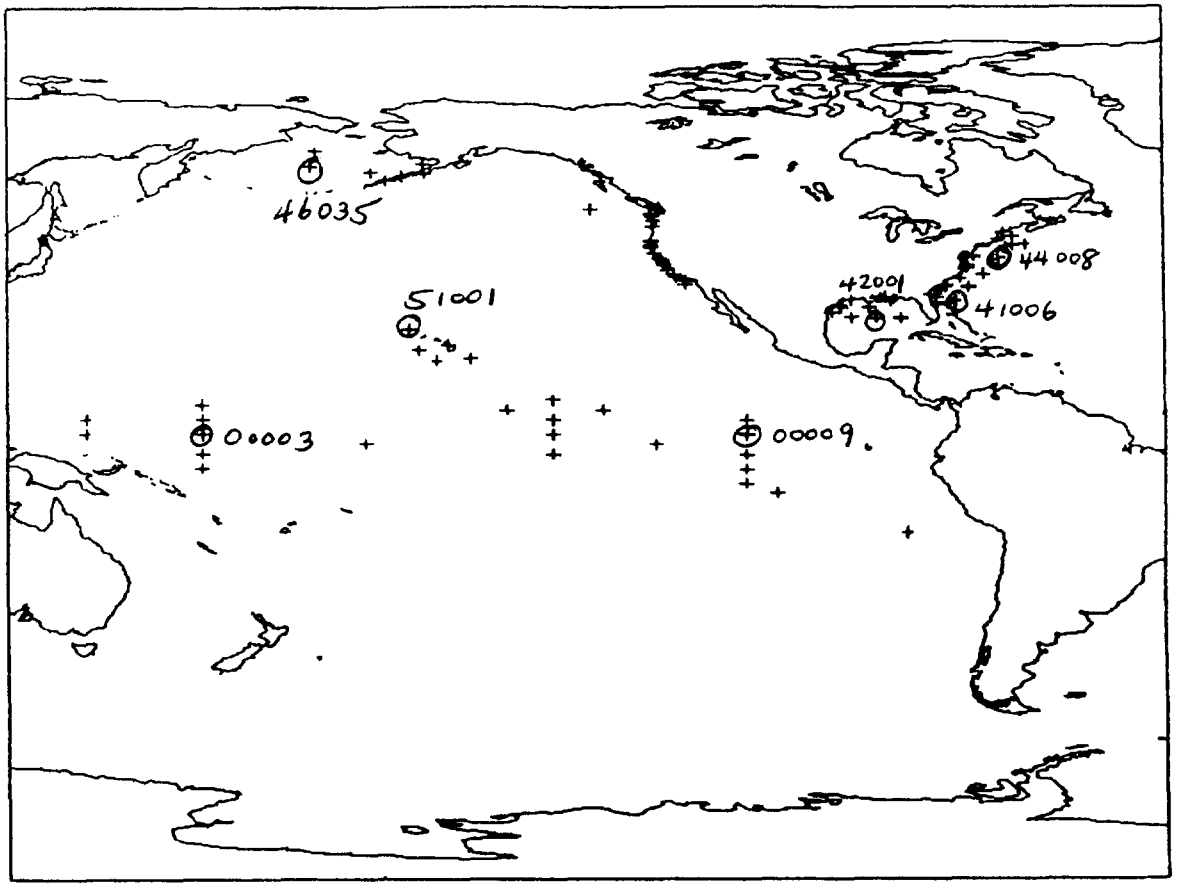

Fig. 23. Geographical location of oceanic moorings which provided data used in the study (Woodward et al. 1992).

8.3 MATCHUP SOFTWARE

Figures 24 and 25 illustrate, respectively, the program logic used to generate wind matchup statistics and the names of the associated SEAPAK software programs. All input data sets were archived in the GSFC Laboratory for Hydrospheric Processes on either 9-track tape (in the case of SSM/I) or write-once read-many (WORM) optical disk platters (for gridded model winds, and NDBC or TOGA-TAO moorings). The data were archived in various binary forms, including NASA CDF.

All applications software were written as part of the ancillary environmental data module in SEAPAK, using the VAX FORTRAN language and the NASA Transportable Applications Executive (TAE) as the user interface. To the best extent possible, batch processing was used to run the VAX software on the Ocean Color Group's two MicroVAX II systems and the Laboratory's VAX 11/750 system with a minimum of user intervention.

In order to generate plots and statistics, separate ASCII formatted files were generated on the VAX. Each ASCII file contained the following:

a) wind data at each of the seven moorings (the program `BUOYREAD` was used to ingest data for the NDBC moorings, and the program `CDF1D2GM` was used for the TOGA-TAO moorings);

b) the grid point closest to each mooring for each global model (`TIMENV` was used); and

c) SSM/I data ranging within 35 km of each mooring (`SSMIMTCH` was used).

Note that for the portion of the study comparing 1990 NMC 1,000 mb and boundary layer winds to mooring winds, the bilinear interpolation option in `TIMENV` was used to create a group of NMC time series interpolated to the exact mooring locations.

The temporal window used for matchup was ±30 minutes for global wind matches to the NDBC moorings, and one day for global wind matches to the TOGA-TAO moorings (Table 22). Therefore, the NDBC matchups tended to be clustered around 0000 Greenwich Mean Time (GMT) and 1200 GMT when comparisons were done with the gridded models. Likewise, the daily mean TOGA-TAO moorings were arbitrarily assigned a time of 0000 GMT, so that

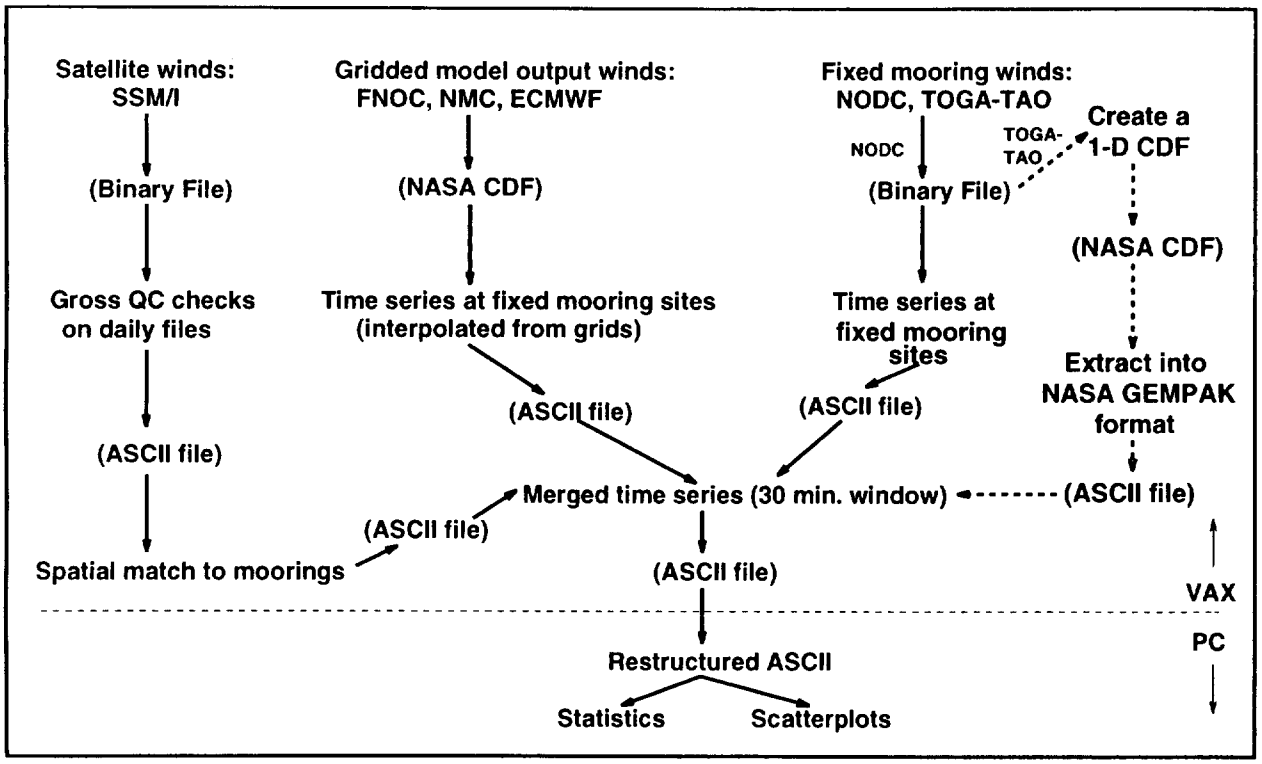

Fig. 24. Schematic diagram of the data path used to generate wind statistics and scatterplots.

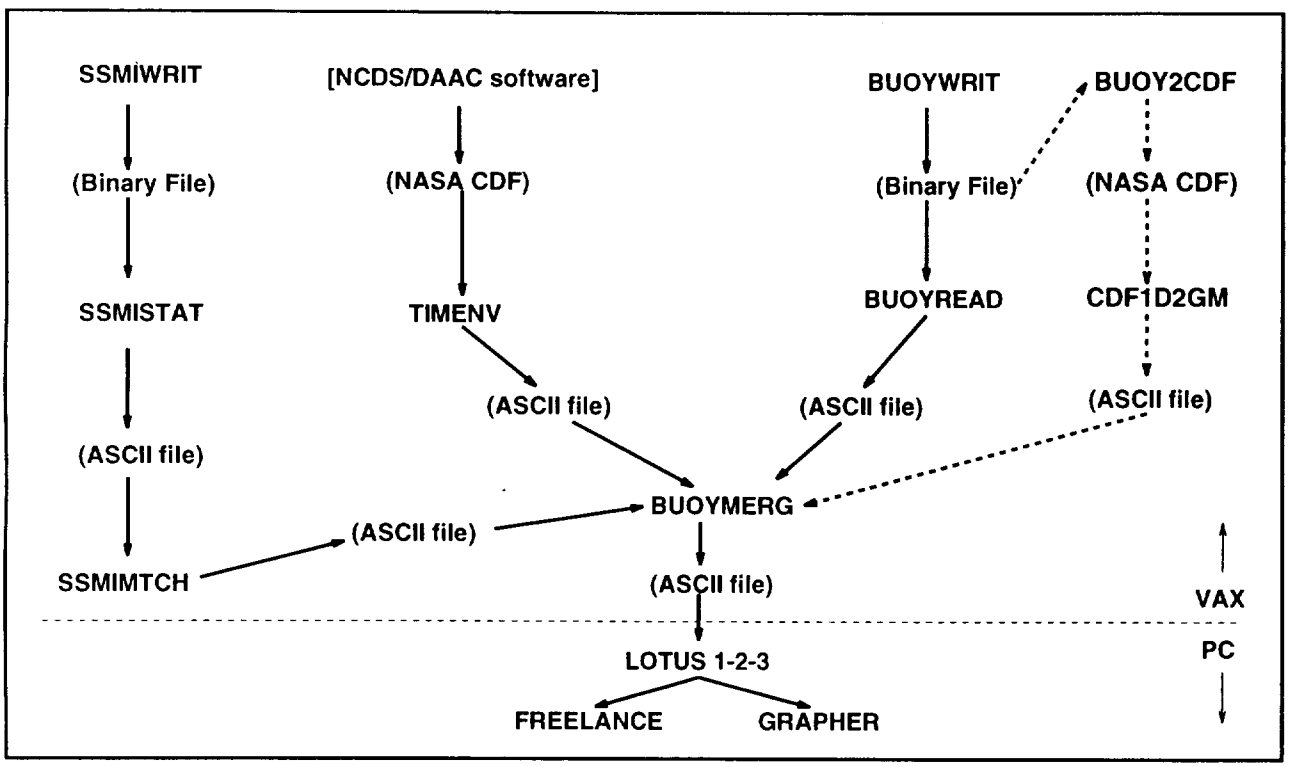

Fig. 25. Software programs for generating wind statistics and scatterplots. (All VAX programs, other than those from NCDS DAAC, are included in SEAPAK from the GSFC Laboratory for Hydrospheric Processes.)

Table 22. Summary of matchup criteria and ingest software used in the study. Each group of descriptors, which are delimited by colons (:), indicates the following (reading left to right): the matchup temporal window, the matchup spatial window, the SEAPAK program used for ingesting the global data, and finally the SEAPAK program used for ingesting the mooring data (np means nearest grid point). Note that for the portion of the study which compared NMC and mooring winds for only the year 1990, a model value interpolated to each mooring location was used rather than the nearest model grid point.

Wind Product Model	*NDBC Moorings*	*TOGA-TAO Moorings*
FNOC, NMC, ECMWF	`30min:np:TIMENV:BUOYREAD`	`daily:np:TIMENV:CDF1D2GM`
SSM/I	`30min:35km:SSMIMTCH:BUOYREAD`	`daily:35km:SSMIMTCH/CDF1D2GM`

global gridded winds and SSM/I winds collected from 0000 GMT of that day to 0000 GMT of the next day were included in the matchups. Each data ingest run of `BUOYREAD`, `CDF1D2GM`, `TIMENV`, or `SSMIMTCH` was executed over the time ranges available for the individual data sets, as depicted in Fig. 22.

The following commercial PC software was used to interface with the output of the VAX software: Lotus 1-2-3 for Windows, Lotus Freelance for Windows, Norton editor (Symantec, Inc.), Grapher (Golden Software, Inc.), and WordPerfect (WordPerfect Corp.). This approach utilizes the particular strengths of each software package—namely their ability to restructure, plot, and generate basic statistics relating to the matchups. Lotus 1-2-3 for Windows was used to eliminate unnecessary, e.g., non-wind, data columns in the merged ASCII file so the merged ASCII file could be easily imported into Freelance for Windows and Grapher.

After processing by Lotus 1-2-3, the two columns of data (global and mooring wind) were saved again as an ASCII file. The file was then edited, using the Norton editor to globally change a numerical code used for denoting missing wind data, `-99`, to an entry of `M` (for *missing*), so plotting would proceed correctly. Freelance for Windows was used to generate statistics, including the square of the correlation coefficient (R^2), slope and intercept, and the number of observations for the matchups stored in each edited ASCII file. Grapher was used to generate x-y scatterplots for the matchups in each edited ASCII file, and to save each plot in Hewlett Packard Graphics Language (HPGL) format. WordPerfect was used to import the HPGL files representing the scatterplots for a particular buoy (five in total) into a document in which the statistics were also written. The documents, with scatterplots included, were printed on an Apple Laserwriter printer.

8.4 RESULTS

Figures 26–32 show the scatterplots generated for each of the seven moorings, and the associated R^2, slope, and intercept statistics, based on data for the entire period 1982–90. The NMC and ECMWF models generated winds at the 1,000 mb pressure level, the TOGA-ECMWF model generated winds at the surface, while FNOC winds were in the near surface marine layer (approximately 10 m above the ocean surface). Figures 33 and 34 represent matchups using 1990 data only, at the NDBC Gulf of Mexico (No. 42001) and mid-Atlantic US coast (No. 44008) moorings. The NMC and FNOC models were used for the 1990-only study, since they were the likeliest candidates for real time reception in SeaWiFS. To facilitate comparisons with the FNOC winds, an additional set of NMC winds were used in the 1990-only study to supplement the 1,000 mb values. This second set contained NMC boundary layer winds obtained from the National Center for Atmospheric Research (NCAR), put into hemispheric CDF files by the Goddard DAAC.

On all of the scatterplots, the solid line represents a linear regression computed for the points plotted, while the dashed line represents the *ideal* slope of 1 and intercept of 0 describing the relationship between the mooring and global data sets. The date range indicated at the top of each scatterplot indicates the actual starting and ending dates for the matches found between a particular global data set and a mooring. Therefore, the range varied from mooring to mooring for comparisons with a given global data set, and across different global data sets for a particular mooring. The number of observations included in each scatterplot varied widely, from minimally in the hundreds of observations, to a maximum of nearly 4,000 over the period 1982–90. Note also that the scale for SSM/I wind speed begins at -10 rather than zero. The reason for this convention is that the SSM/I winds are retrievals based on passive microwave data, and the algorithm allows values slightly less than zero. In addition, removing these negative values would bias the statistics (F. Wentz pers. comm.).

The results for the 1982–90 analyses show, in general, that R^2 values ranged from 0.5–0.7 for the five NDBC moorings (Figs. 28–32) and 0.2–0.3 for the two TOGA-TAO moorings (Figs. 26 and 27). In addition, of the global data sets, the SSM/I exhibited the highest R^2 values at four out of five NDBC moorings, with values in the 0.6–0.7 range. One reason for this difference is the relatively close proximity between SSM/I passes and moorings when matched (35 km was used as the upper limit), as compared

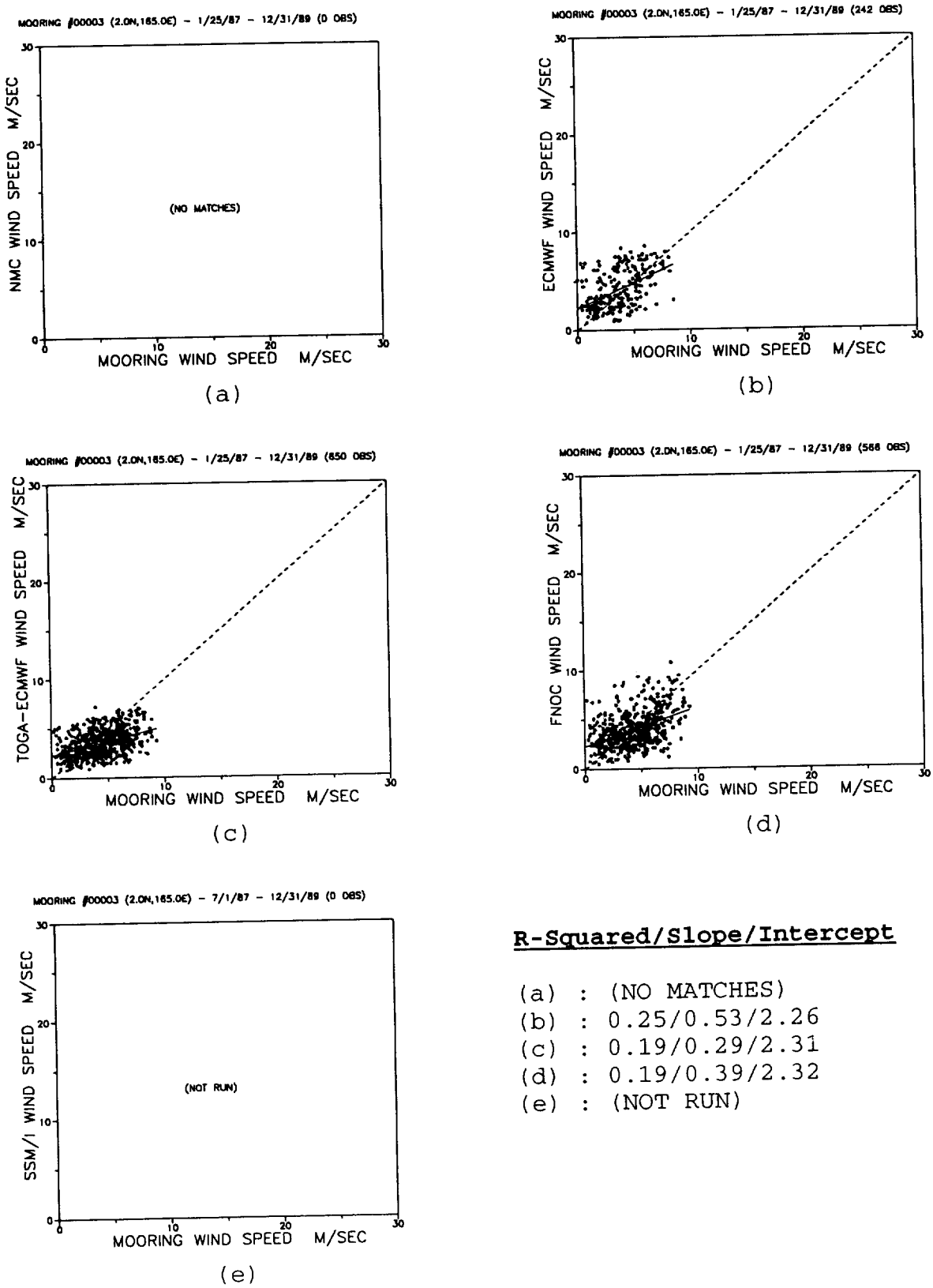

R-Squared/Slope/Intercept

(a) : (NO MATCHES)
(b) : 0.25/0.53/2.26
(c) : 0.19/0.29/2.31
(d) : 0.19/0.39/2.32
(e) : (NOT RUN)

Fig. 26. Scatterplots for ocean mooring 00003, in the west central Pacific Ocean.

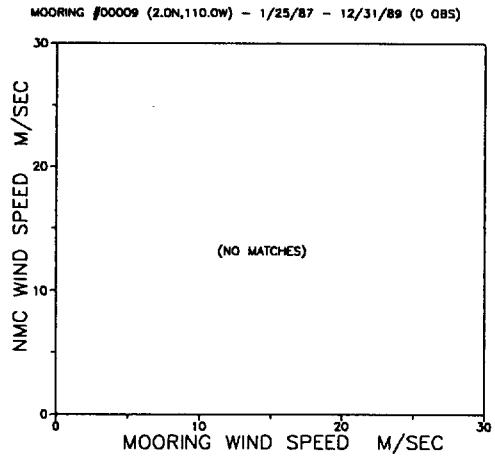

(a)

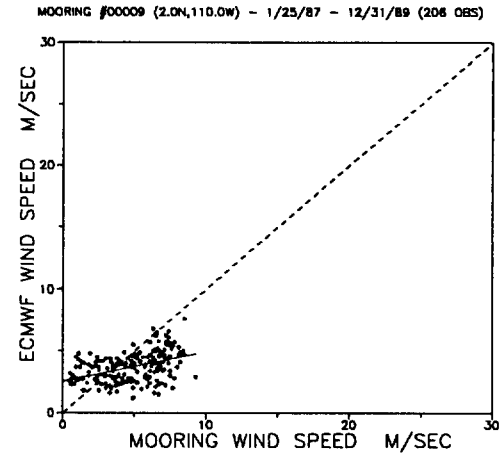

(b)

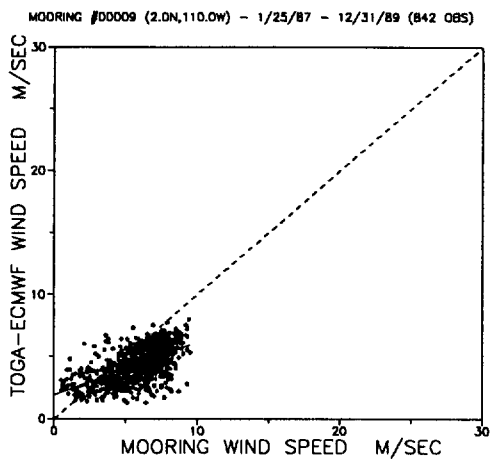

(c)

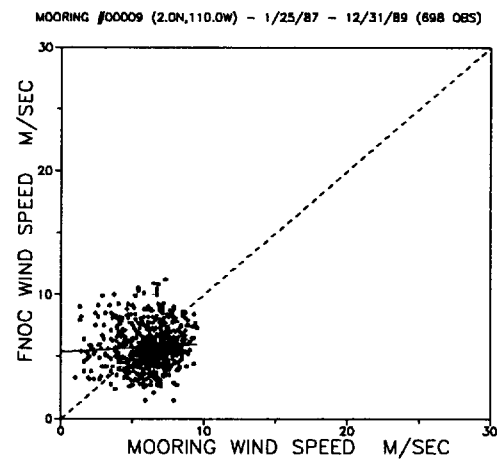

(d)

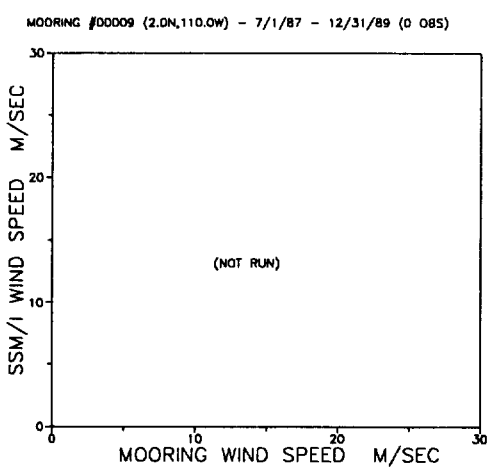

(e)

R-Squared/Slope/Intercept

(a) : (NO MATCHES)
(b) : 0.19/0.24/2.55
(c) : 0.34/0.42/1.94
(d) : 0.004/0.064/5.36
(e) : (NOT RUN)

Fig. 27. Scatterplots for ocean mooring 00009, in the east central Pacific Ocean.

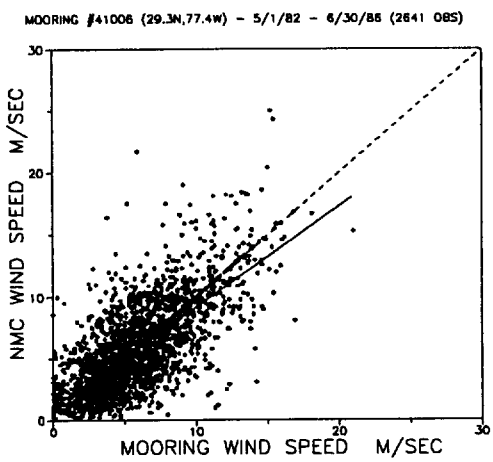

(a)

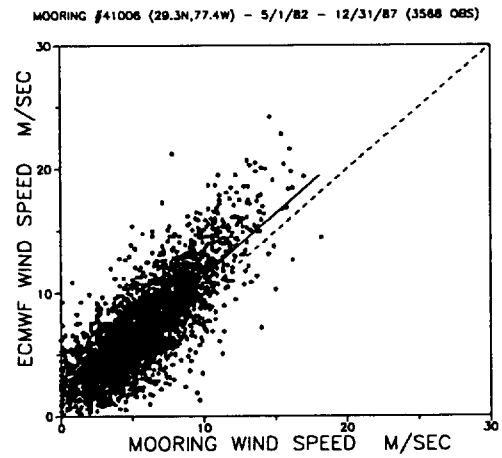

(b)

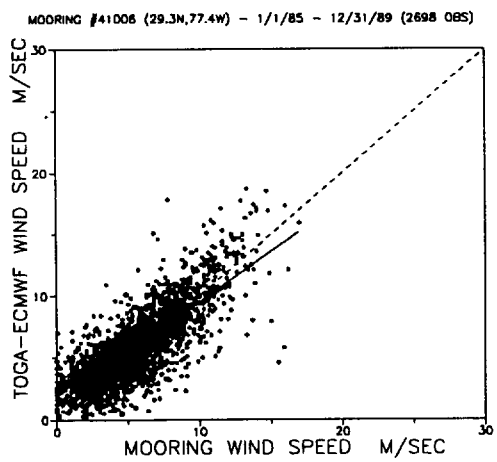

(c)

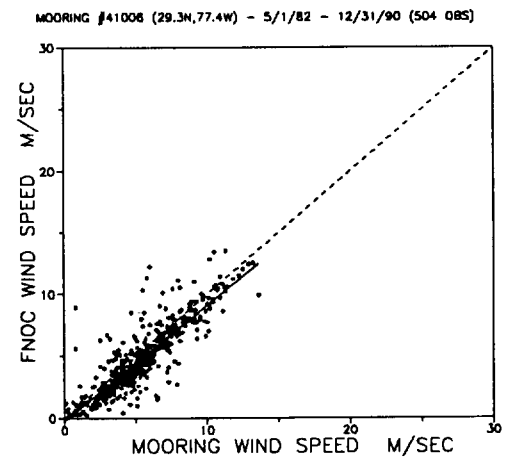

(d)

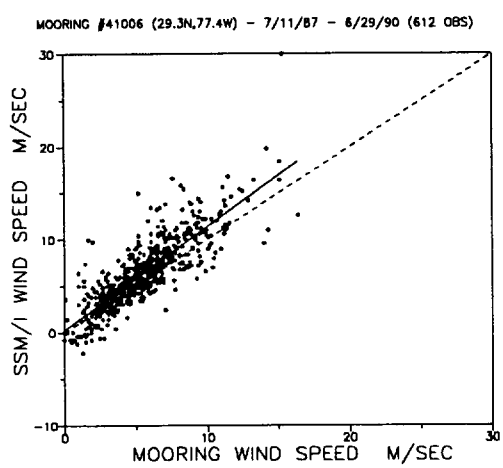

(e)

R-Squared/Slope/Intercept

(a) : 0.59/0.81/1.11
(b) : 0.64/0.99/1.56
(c) : 0.63/0.82/1.31
(d) : 0.75/0.93/-0.21
(e) : 0.70/1.11/0.25

Fig. 28. Scatterplots for ocean mooring 41006, located near the southeastern (Atlantic Ocean) coast of the United States.

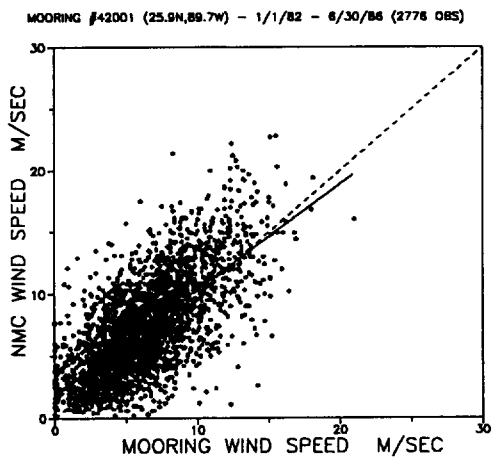

(a)

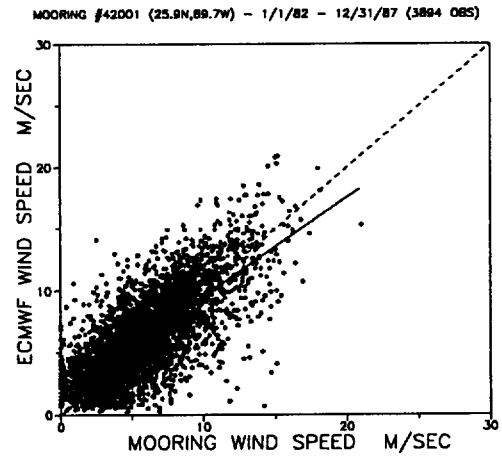

(b)

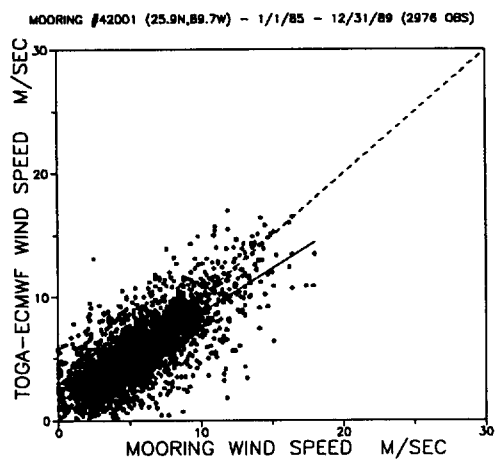

(c)

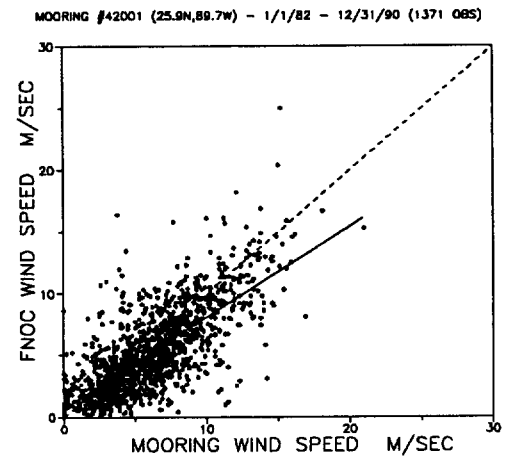

(d)

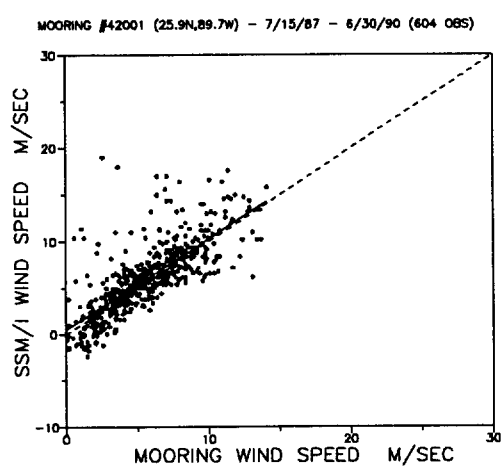

(e)

R-Squared/Slope/Intercept

(a) : 0.48/0.85/1.86
(b) : 0.54/0.80/1.63
(c) : 0.57/0.72/1.52
(d) : 0.53/0.74/0.71
(e) : 0.58/0.98/0.51

Fig. 29. Scatterplots for ocean mooring 42001, located in the Gulf of Mexico.

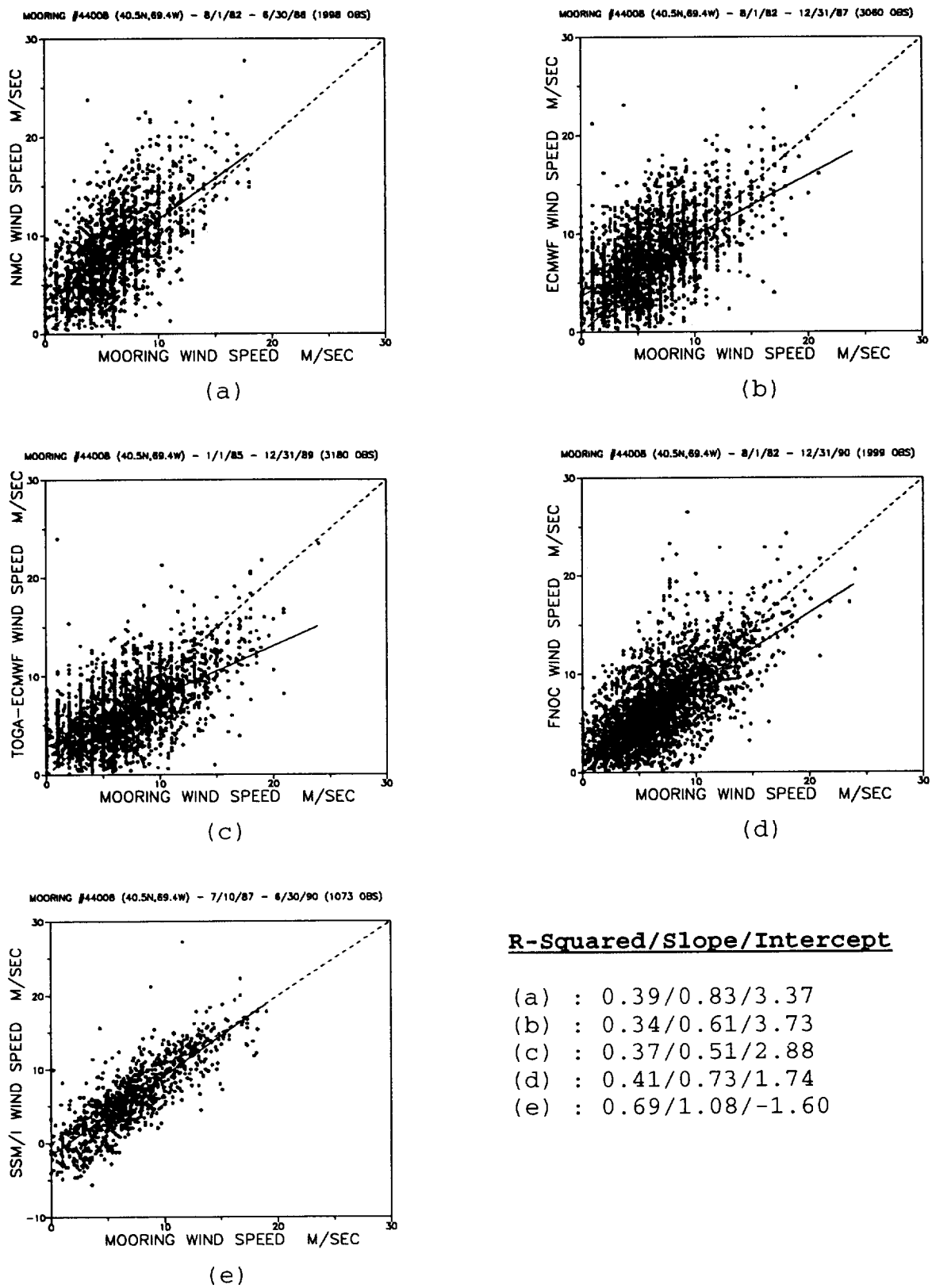

R-Squared/Slope/Intercept

(a) : 0.39/0.83/3.37
(b) : 0.34/0.61/3.73
(c) : 0.37/0.51/2.88
(d) : 0.41/0.73/1.74
(e) : 0.69/1.08/-1.60

Fig. 30. Scatterplots for ocean mooring 44008, located off of the mid-Atlantic coast of the United States.

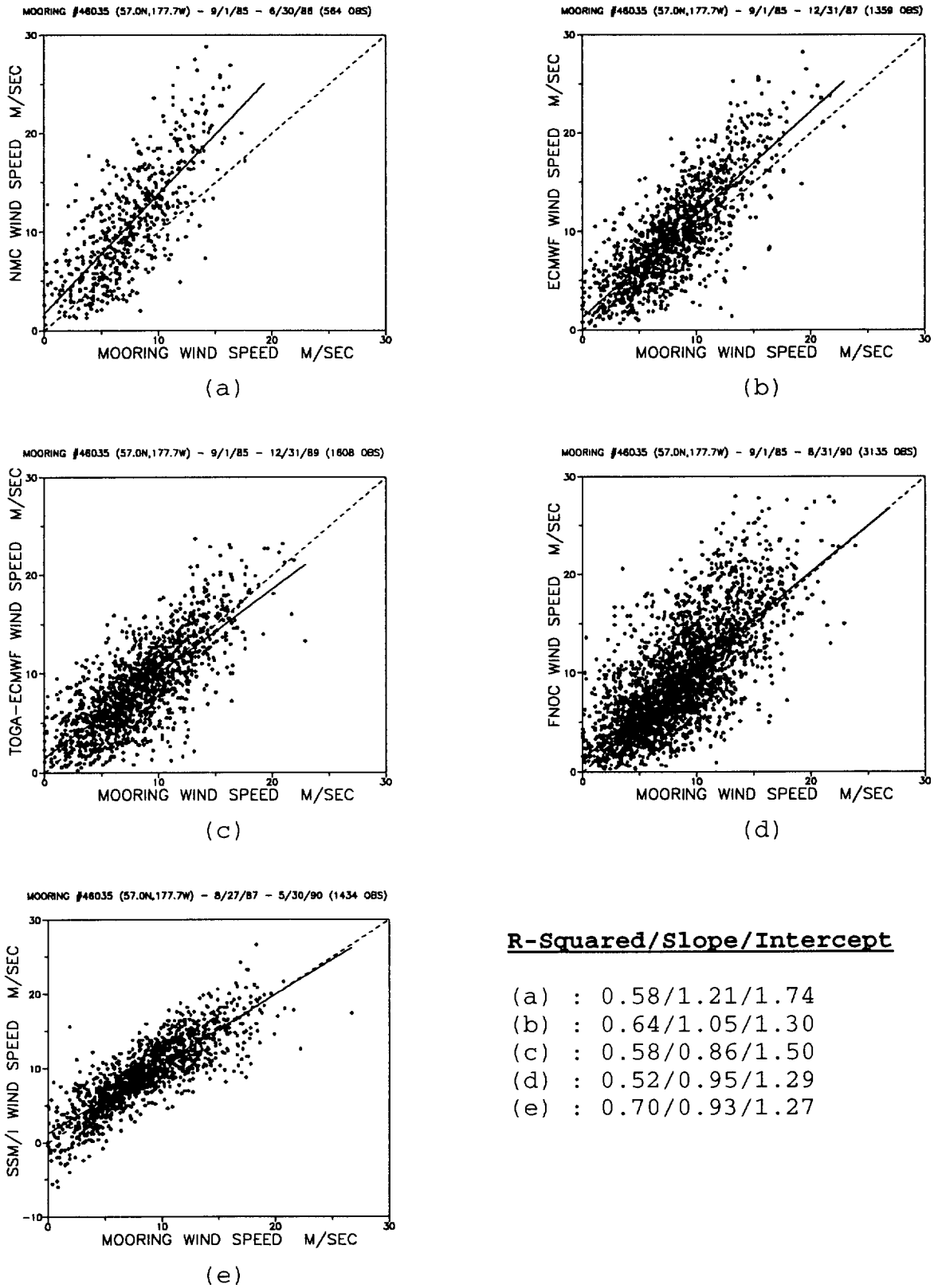

R-Squared/Slope/Intercept

(a) : 0.58/1.21/1.74
(b) : 0.64/1.05/1.30
(c) : 0.58/0.86/1.50
(d) : 0.52/0.95/1.29
(e) : 0.70/0.93/1.27

Fig. 31. Scatterplots for ocean mooring 46035, in the Bering Sea.

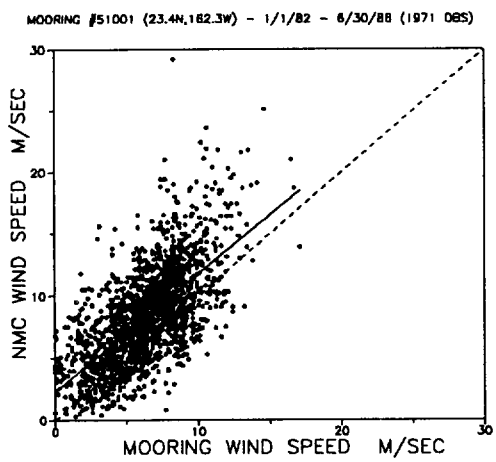

(a)

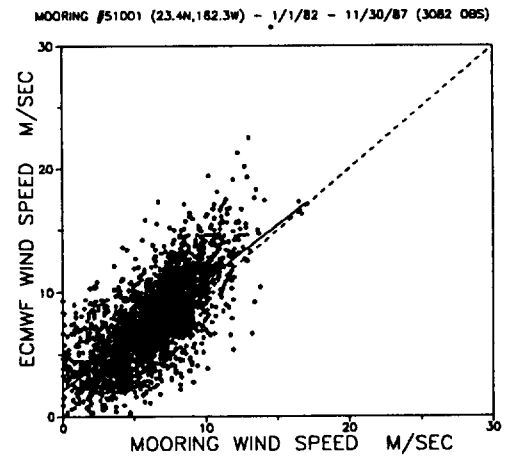

(b)

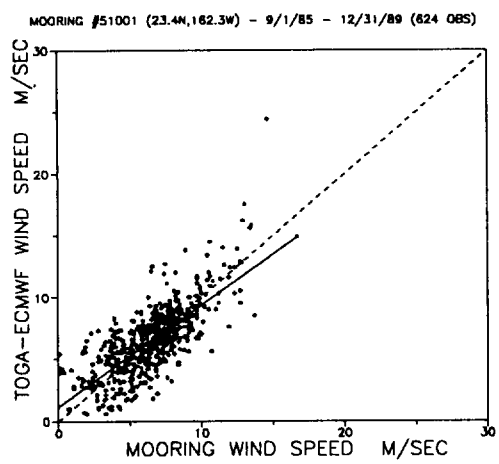

(c)

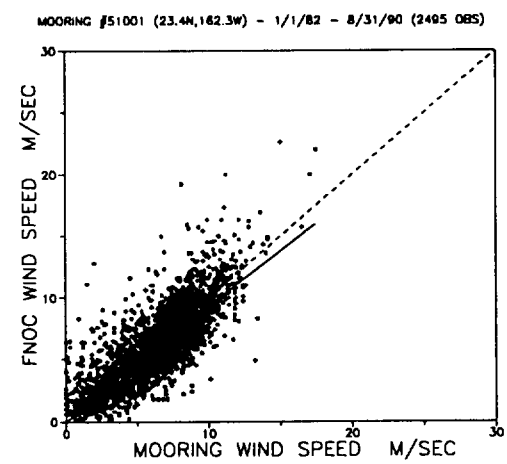

(d)

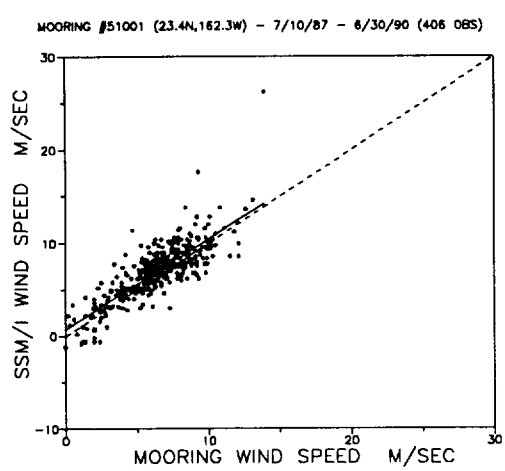

(e)

R-Squared/Slope/Intercept

(a) : 0.44/0.95/2.34
(b) : 0.51/0.88/2.16
(c) : 0.55/0.82/1.18
(d) : 0.61/0.89/0.50
(e) : 0.67/0.97/0.76

Fig. 32. Scatterplots for ocean mooring 51001, near the Hawaiian islands.

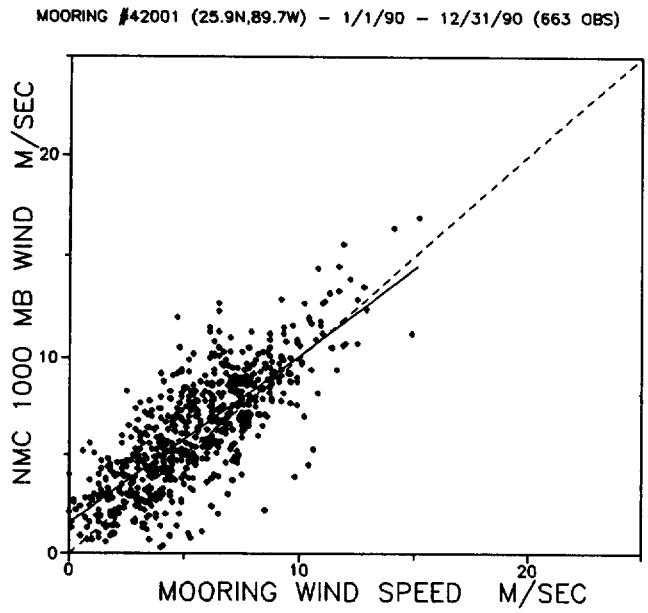

(a)

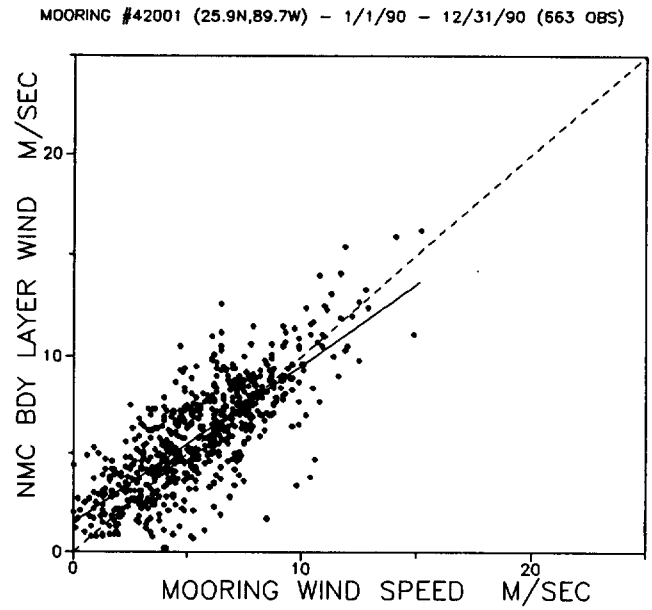

(b)

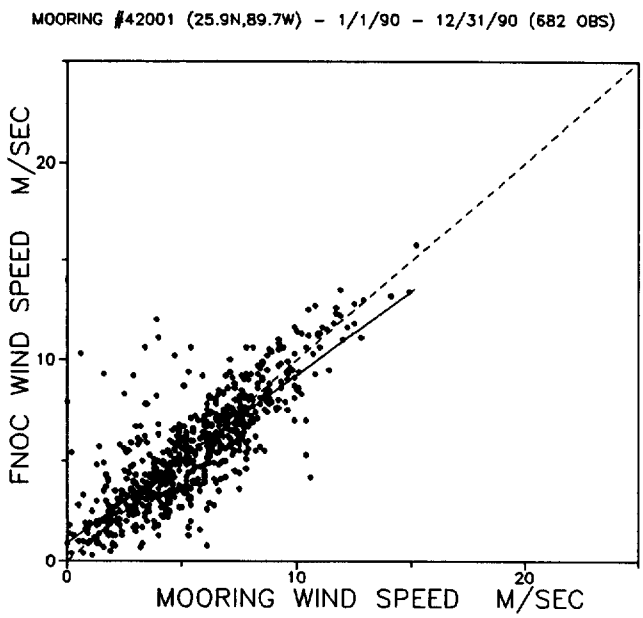

(c)

R-Squared/Slope/Intercept

(a) : 0.61/0.86/1.52
(b) : 0.60/0.81/1.47
(c) : 0.65/0.83/0.91

Fig. 33. Scatterplots for data collected in the year 1990 from ocean mooring 42001, located in the Gulf of Mexico.

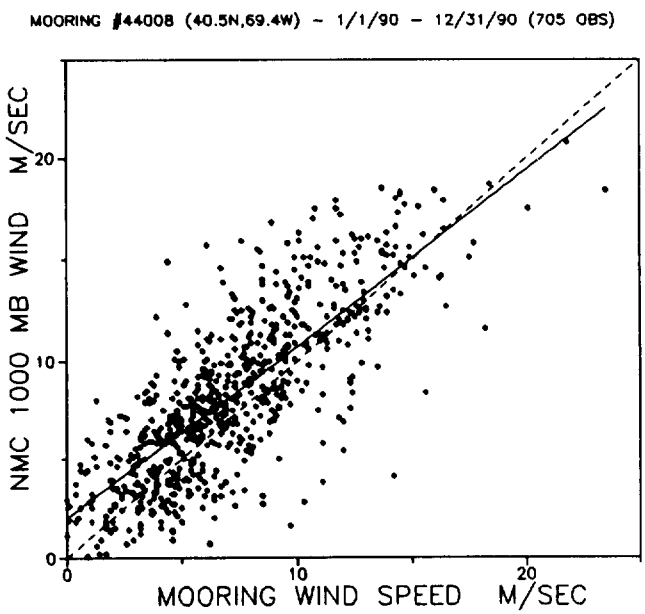

(a)

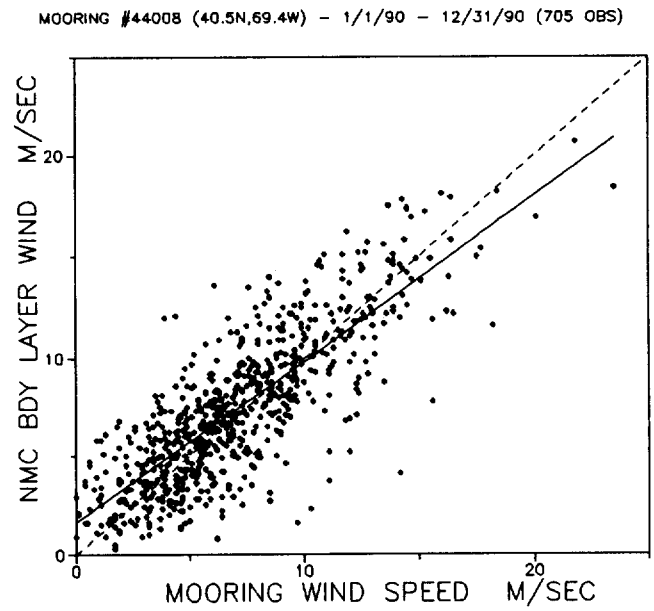

(b)

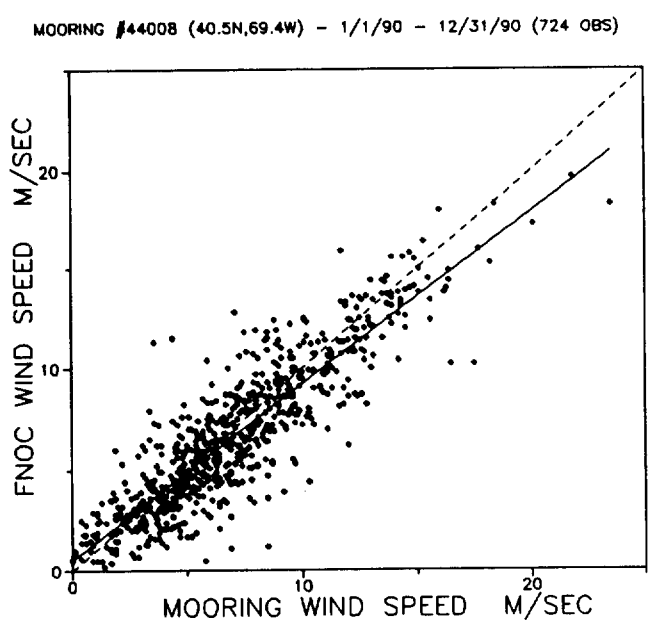

(c)

R-Squared/Slope/Intercept

(a) : 0.61/0.87/1.99
(b) : 0.66/0.82/1.63
(c) : 0.79/0.87/0.54

Fig. 34. Scatterplots for data collected in the year 1990 from ocean mooring 44008, located off of the mid-Atlantic coast of the United States.

with the distance between gridded model points and moorings when matched (as large as half the distance between grid points, or 1.25°, which is approximately 140 km).

The slopes of the regression lines generally varied from 0.7–1.2. Most of the slope values were less than 1.0, indicating that in these cases, the global wind speed was an underestimate of the wind speed measured at the mooring. This is to be expected, since the models tend to be smooth fields, while the ground truth often represents extremes in the data. The tendency for the models to underestimate wind speeds was especially true at the mid-Atlantic coast mooring (No. 44008 in Fig. 30). This observation may be due to the inability of weather models to capture the strength of storms which intensify as they move off shore. The slopes were the smallest of all at the TOGA-TAO moorings, perhaps indicative of the influence of tropical convective elements in strengthening the local wind field, and the shortcomings in convective parameterizations in the global models. The intercept values for both the NDBC and TOGA-TAO moorings were nearly always positive. This shows that the global fields rarely, if ever, include totally calm winds at a grid point, even though an individual mooring might measure calm winds.

In looking at the results for just 1990 (Figs. 33 and 34), it is clear they do not differ significantly from the 1982–90 results (Figs. 29 and 30) for the two moorings studied. The only difference is both the R^2 and slope values are slightly higher for 1990. The improvement in R^2 may be attributable to the interpolation of NMC model winds to the mooring locations, thus reducing scatter about the regression line. However, the models still underestimated the *in situ* winds by 15–20%. Differences between the NMC 1,000 mb wind product and the derived boundary layer winds are also slight. This result is consistent with the finding of Trenberth et al. (1990), which is in most cases the 1,000 mb wind closely approximates the boundary layer wind.

Based on these results, all of the global model products exhibited very similar levels of skill. Since mechanisms are already available to the SeaWiFS Project for receiving both FNOC and NMC data in near-real time, they are the suggested sources for ancillary wind data.

Glossary

ASCII American Standard Code for Information Interchange
AU Astronomical Unit

BRDF Bidirectional Reflectance Distribution Function

CCD Charge Coupled Device
CD-ROM Compact Disk-Read Only Memory
CDF (NASA) Common Data Format
CVT Calibration and Validation Team
CZCS Coastal Zone Color Scanner

DAAC Distributed Active Archive Center
DAO Data Assimilation Office
DC Digital Counts
DEC Digital Equipment Corporation
DoD Department of Defense
DOS Disk Operating System
DU Dobson Units

ECMWF European Centre for Medium-Range Weather Forecasts
EOS Earth Observing System
EOSDIS EOS Data Information System

FGGE First GARP Global Experiment
FORTRAN Formula Translation (computer language)
FNOC Fleet Numerical Oceanography Center
FTP File Transfer Protocol

GARP Global Atmospheric Research Program
GMT Greenwich Mean Time
GRIB Gridded Binary
GRIDTOMS Gridded TOMS (data)
GSFC Goddard Space Flight Center

HDF Hierarchical Data Format
HHCRM Hand-Held Contrast Reduction Meter
HPGL Hewlett Packard Graphics Language
HRPT High Resolution Picture Transmission
HST Hawaii Standard Time

IBM International Business Machines
IDL Interface Design Language
IFOV Instantaneous Field-of-View
I/O Input/Output
ISTP International Solar Terrestrial Program

JPL Jet Propulsion Laboratory

Level-0 Raw data
Level-1 Calibrated radiances
Level-2 Derived products
Level-3 Gridded and averaged derived products

NASA National Aeronautics and Space Administration
NCAR National Center for Atmospheric Research
NCDS NASA Climate Data System
NCSA National Center for Supercomputing Applications
NDBC National Data Buoy Center
NESDIS National Environmental Satellite Data Information Service
netCDF (NASA) Network Common Data Format
NFS Network File System
NMC National Meteorological Center
NOAA National Oceanic and Atmospheric Administration
NODC National Oceanographic Data Center
NRT Near-Real Time
NSF National Science Foundation
NSSDC National Space Science Data Center

OPT Ozone Processing Team

PC (IBM) Personal Computer
PMEL Pacific Marine Environmental Laboratory
PST Pacific Standard Time

QC Quality Control
QED Quantum Efficient Device

RSS Remote Sensing Systems (Inc.)

SBRC (Hughes) Santa Barbara Research Center
SBUV Solar Backscatter Ultraviolet Radiometer
SDPS SeaWiFS Data Processing System
SDS Scientific Data Set
SEAPAK Not an acronym, an image display and analysis package developed at GSFC.
SeaWiFS Sea-viewing Wide Field-of-view Sensor
SGI Silicon Graphics, Inc.
SSM/I Special Sensor for Microwave/Imaging

TAE Transportable Applications Executive
TAO Thermal Array for the Ocean or more recently, Tropical Atmosphere-Ocean
TIROS Television Infrared Observation Satellite
TOA Top of the Atmosphere
TOGA Tropical Ocean Global Atmosphere program
TOMS Total Ozone Mapping Spectrometer
TOVS TIROS Operational Vertical Sounder
TRMM Tropical Rainfall Measuring Mission

UCAR University Consortium for Atmospheric Research

VAX Virtual Address Extension

WORM Write-Once Read-Many (times)

XDR External Data Representation

Symbols

A_d The detector aperture.
A_f The foam reflectance.
a Exponential value in the expression relating the radiance of scattered light to wavelength.

C Chlorophyll concentration.
C_{ext} Average total extinction cross-section of a particle.
C_F The calibration factor.

d The distance between the sphere aperture and the detector aperture.
$d(I(\lambda))$ An increment in detector current.
$d\lambda$ An increment in wavelength.
DC Digital counts.
DC_{meas} The digital counts measured unshadowed.
DC_{scat} The digital counts due to scattered sunlight.
DC_{TOA} The digital counts measured at the top of the atmosphere.

$E(\lambda)$ Irradiance.
E_{eff} Effective center wavelength.
E_S The irradiance of the sun.

f The fraction of the surface covered by foam.
F_0 The solar spectral irradiance at the top of the atmosphere.
$\mathbb{F}_0$ The scalar value of the solar spectral irradiance at the top of the atmosphere, multiplied by a columnar

matrix of the four Stokes parameters (1/2, 1/2, 0, 0).

F_d The total flux incident on the surface if it did not reflect light.

F'_d The total flux incident on the surface, corrected for surface reflection.

$\mathbb{F}'_d$ The scalar value of the total flux incident on the surface, corrected for surface reflection, multiplied by a columnar matrix of the four Stokes parameters.

H_M The measured moon irradiance.

$I(\lambda)$ Detector current.

$L(\lambda)$ Radiance.

L_0 The radiance of the atmosphere.

L_a The radiance of scattered light.

$\mathbb{L}_d$ A matrix of the four Stokes parameters for radiance incident on the surface.

$L_i(\lambda)$ Radiance, where i may represent any of the following: m for measured; LU for look-up table; 0 for light scattered by the atmosphere; sfc for reflection from the sea surface; and w for water-leaving radiance.

L_{LU} The radiance calculated for the look-up tables.

L_m The radiance of the ocean-atmosphere system measured at a satellite.

L_M The radiance of the moon.

L_{sa} $L_0 + L_{\text{sfc}}$.

L_{sfc} The radiance of the light reflected from the sea surface.

$\mathbb{L}_{\text{up}}$ The columnar matrix of light leaving the surface containing the values $L_{\text{up},1}$, $L_{\text{up},2}$, $L_{\text{up},3}$, and $L_{\text{up},4}$ [(20), (21), (22), and (23), respectively].

$L_{\text{up},i}$ The **RADTRAN** radiance parameters (for $i = 1, 4$).

$\mathbb{L}_{\text{sfc}}$ The columnar matrix of the four Stokes parameters ($L_{u,1}$, $L_{u,2}$, $L_{u,3}$, $L_{u,4}$).

L_W The water-leaving radiance of light scattered from beneath the surface and penetrating it.

$\mathbb{L}_w$ The scalar value of the water-leaving radiance multiplied by a columnar matrix of the four Stokes parameters.

$L_{WN}()$ Normalized water-leaving radiance.

$L(\lambda_m)$ The radiance of a calibration sphere at the nominal peak wavelength of a filter.

n The index of refraction.

N_D The compensation factor for a 4 log neutral density filter.

N Total number density.

N_i Total number density of either the first or second aerosol model when $i = 1$ or 2, respectively.

$p_a/(4\pi)$ Aerosol albedo of the scattering phase function.

r_1 Radius of the sphere aperture.

r_2 Radius of the receiving aperture.

$\mathbb{R}$ The reflection matrix.

$R(\lambda)$ Reflectance.

R^2 The square of the linear correlation coefficient.

r_i The geometric mean radii of either the first or second aerosol model when $i = 1$ or 2, respectively.

s The reflectance of the atmosphere for isotropic radiance incident at its base.

t The transmission of L_{sfc} through the atmosphere.

t' The transmission of L_W through the atmosphere.

t_0 The sum of the direct and diffuse transmission of sunlight through the atmosphere.

$T(\lambda)$ The transmittance along the slant path to the sun.

V_M The radiance detector voltage while viewing the moon.

V_S The irradiance detector voltage while viewing the sun.

W Surface wind speed.

α Exponential value in the expression relating the extinction coefficient to wavelength.

β_i The extinction coefficient of either the first or second aerosol model when $i = 1$ or 2, respectively.

δ The absorption coefficient.

$\Delta L_W(670)$ The error in the water-leaving radiance for the red channel.

$\Delta T(\lambda)$ The error in transmittance.

$\Delta\theta_s$ The error (in radians) in the knowledge of θ_s.

$\Delta\lambda$ A wavelength increment.

$\Delta\rho_w(\lambda)$ The error in the water-leaving reflectance for the red channel.

$\Delta\rho_{LU}(670)$ The error in the look-up radiance.

$\Delta\sigma(\lambda)$ The absolute error in spectral optical depth.

$\Delta\tau_a$ The error in the aerosol optical thickness.

$\gamma(\lambda)$ The ratio of the aerosol optical thickness at wavelength, λ, to the aerosol optical thickness at 670 nm.

κ An integration constant: $\kappa = A_d \pi r_1^2 (r_1^2 + r_2^2 + d^2)^{-1}$.

θ Polar angle of the line-of-sight at a spacecraft.

θ_0 Polar angle of the direct sunlight.

θ_s The solar zenith angle.

λ Wavelength of light.

λ_1 Starting wavelength.

λ_2 Ending wavelength.

λ_m Nominal center wavelength.

μ_s The reciprocal of the effective optical length to the top of the atmosphere, along the line of sight to the sun.

ρ The average reflectance of the sea.

ρ_i The reflectance of the sea of either the first or second aerosol model when $i = 1$ or 2, respectively.

$\rho_i(\lambda)$ The reflectance where i may represent any of the following: m for measured; LU for look-up table; o for light scattered by the atmosphere; sfc for reflection from the sea surface; and w for water-leaving radiance.

$\sigma(\lambda)$ The spectral optical depth.

σ_i^2 $\sigma_i^2 = \langle(\log r - \log r_i)^2\rangle$.

τ_a The aerosol optical thickness.

τ_{oz} The optical thickness of ozone.

τ_r The optical thickness due to scattering by the standard molecular atmosphere.

τ_{wv} The absorption optical thickness of water vapor.

ϕ Azimuth angle of the line-of-sight at a spacecraft.

ϕ_0 Azimuth angle of the direct sunlight.

Φ_D The detector solid angle.

Φ_M The solid angle subtended by the moon at the measuring instrument.

ω_a Aerosol albedo of single scattering.

Ω The amount of ozone (in Dobson units).

References

Ahmad, Z., and R.S. Fraser, 1982: An iterative radiative transfer code for ocean-atmosphere systems. *J. Atmos. Sci.*, **39**, 656–665.

Berk, A., L.S. Bernstein, and D.C. Robertson, 1989: MODTRAN: A moderate resolution model for LOWTRAN 7. *GL-TR-89-0122,* Geophysics Laboratory, Air Force Systems Command, 38 pp.

Biggar, S.F., D.I. Gellman, and P.N. Slater, 1990: Improved evaluation of optical depth components from Langley plot data. *Remote Sens. Environ.*, **32**, 91–101.

——, P.N. Slater, K.J. Thome, A.W. Holmes, and R.A. Barnes, 1993: Preflight solar-based calibration of SeaWiFS. *Proc. SPIE, Vol. 1,939,* 233–242.

Bruegge, C.J., V.G. Duval, N.L. Chrien, and D.J. Diner, 1993: Calibration plans for the Multi-angle Imaging Spectroradiometer (MISR). *Metrologia,* **30(4)**, 213–221.

Bruening, R.J., 1987: Spectral irradiance scales based on filtered absolute silicon photodetectors. *Appl. Opt.*, **26**, 1,051–1,057.

Corredera, P., A. Corróns, A. Pons, and J. Campos, 1990: Absolute spectral Irradiance scale in the 700–2400 nm spectral range. *Appl. Opt.*, **29**, 3,530–3,534.

Cox, C., and W. Munk, 1955: *Some Problems in Optical Oceanography.* Scripps Institution of Oceanography, LaJolla, California, 63–77.

Darzi, M., J. Chen, J. Firestone, and C.R. McClain, 1989: SEAPAK: A satellite image analysis system for oceanographic research. *Proc. Fifth Intl. Conf. Interactive Information Processing Systems for Meteorol., Oceanogr., and Hydrol.*, Am. Meteorol. Soc., Atlanta, Georgia, 26–32.

Dave, J.V., 1972a: Development of programs for computing characteristics of ultraviolet radiation. *Technical Report—Vector Case, Program IV,* FSC-72-0013, IBM Federal Systems Division, Gaithersburg, Maryland, 138 pp.

——, 1972b: Development of programs for computing characteristics of ultraviolet radiation. *Technical Report—Scalar Case, Program II,* FSC-72-0011, IBM Federal Systems Division, Gaithersburg, Maryland, 38 pp.

Evans, R.H., and H.R. Gordon, 1994: CZCS "System calibration:" A retrospective examination. *J. Geophys. Res.*, **99**, 7,293–7,307.

Firestone, J.K., G. Fu, M. Darzi, and C.R. McClain, 1990: NASA's SEAPAK software for oceanographic data analysis: An update. *Proc. Sixth Intl. Conf. Interactive Information Processing Systems for Meteorol., Oceanogr., and Hydrol.*, Am. Meteorol. Soc., Anaheim, California, 260–267.

——, and B.D. Scheiber, 1994: "The Generation of Ancillary Data Climatologies." In: McClain, C.R., K.R. Arrigo, J. Comiso, R. Fraser, M. Darzi, J.K. Firestone, B. Schieber, E-n. Yeh, and C.W. Sullivan, 1994: Case Studies for SeaWiFS Calibration and Validation, Part 1. *NASA Tech. Memo. 104566, Vol. 13,* S.B. Hooker and E.R. Firestone, Eds., NASA Goddard Space Flight Center, Greenbelt, Maryland, 35–42.

Flittner, D.E., and P.N. Slater, 1991: Stability of narrow-band filter radiometers in the solar-reflective range. *Photogramm. Eng. Remote Sens.*, **57**, 165–171.

Fraser, R.S., 1993: Optical thickness of atmospheric dust over Tadjhikistan. *Atmos. Envir.*, **27A**, 2,533–2,538.

Fraser, R.S., R.A. Ferrare, Y.J. Kaufman, B.L. Markham, and S. Mattoo, 1992: Algorithm for atmospheric corrections of aircraft and satellite imagery. *Int. J. Remote Sens.*, **13**, 541–557.

——, D.K. Clark, J.W. Brown, O.B. Brown, R.H. Evans, and W.W. Broenkow, 1983: Phytoplankton pigment concentrations in the middle Atlantic bight: Comparison of ship determination and CZCS estimates. *Appl. Opt.*, **22**, 20–36.

Gordon, H.R., and D.J. Castaño, 1987: Coastal Zone Color Scanner atmospheric correction algorithm: Multiple scattering effects. *Appl. Opt.*, **26**, 2,111–2,122.

Griggs, M., 1968: Absorption coefficients of ozone in the ultraviolet and visible regions. *J. Chem. Phys.*, **49**, 857.

Hayes, S.P., L.J. Mangum, J. Picaut, A. Sumi, and K. Takeuchi, 1991: TOGA-TAO: A moored array for real-time measurements in the tropical Pacific Ocean. *Bull. Am. Meteor. Soc.*, **72**, 339–347.

Hoppel, W.A., J.W. Fitzgerald, G.M. Frick, and R.E. Larson, 1990: Aerosol size distributions and optical properties found in the marine boundary layer over the Atlantic Ocean. *J. Geophys. Res.*, **95**, 3,659–3,686.

Hovis, W.A., D.K. Clark, F. Anderson, R.W. Austin, W.H. Wilson, E.T. Baker, and C.S. Yentsch, 1980: Nimbus-7 Coastal Zone Color Scanner: System description and initial imagery. *Science,* **210**, 63–66.

Hughes, C.G., III, 1982: Silicon photodiode absolute spectral self-calibration using a filtered tungsten source. *Appl. Opt.*, **21**, 2,129–2,132.

Inn, E.C.Y., and Y. Tanaka, 1953: Absorption coefficient of ozone in the ultraviolet and visible regions. *J. Opt. Soc. Amer.*, **43**, 870–873.

Iqbal, M., 1983: *An Introduction to Solar Radiation.* Academic Press, New York, 390 pp.

Jerlov, N.G., 1976: *Marine Optics.* Elsevier Scientific Pub. Co., New York, 231 pp.

Jursa, A.S., 1985: *Handbook of Geophysics and the Space Environment.* Air Force Geophysics Laboratory, 18-11–18-24.

Kidwell, K.B., 1991: *NOAA Polar Orbiter Data User's Guide.* National Oceanic and Atmospheric Administration, National Environmental Satellite Data and Information Service, 294 pp.

Kneizys, F.X., E.P. Shettle, W.O. Gallery, J.H. Chetwynd, L.W. Abreu, J.E.A. Selby, S.A. Clough, and R.W. Fenn, 1983: *Atmospheric transmittance/ radiance: computer code LOWTRAN 6.* AFGL-TR-83-0187, Air Force Geophysics Lab, Hanscom AFB, Massachusetts, 200 pp.

Koepke, P., 1985: The reflectance factors of a rough ocean with foam. Comment on "Remote sensing of sea state using the 0.8–1.1 m spectral band" by L. Wald and M. Monget. *Int. J. Remote Sens.,* **6,** 787–799.

Lynnes, C., B. Vollmer, H. Griffioen, and P. King, 1992: *Metadata Submission Guide, version 0.9.* NASA Goddard Space Flight Center DAAC, Oct. 2, 1992, NASA GSFC, Greenbelt, Maryland, 11 pp.

McClain, C.R., M. Darzi, J. Firestone, E. Yeh, G. Fu, and D. Endres, 1991a: SEAPAK User's Guide, Version 2.0, Vol. I - System Description, *NASA Tech. Memo. 100728,* NASA Goddard Space Flight Center, Greenbelt, Maryland, 158 pp.

——, ——, ——, ——, ——, and ——, 1991b: SEAPAK User's Guide, Version 2.0, Vol. II—Descriptions of Programs, *NASA Tech. Memo. 100728,* NASA Goddard Space Flight Center, Greenbelt, Maryland, 586 pp.

——, and E-n. Yeh, 1994: Sun glint flag sensitivity study. In: C.R. McClain, J.C. Comiso, R.S. Fraser, J.K. Firestone, B.D. Schieber, E-n. Yeh, K.R. Arrigo, and C.W. Sullivan, 1994: Case Studies for SeaWiFS Calibration and Validation, Part 1. *NASA Tech. Memo. 104566, Vol. 13,* S.B. Hooker and E.R. Firestone, Eds., NASA Goddard Space Flight Center, Greenbelt, Maryland, 46–47.

McLean, J.T., and B.W. Guenther, 1989: Radiance calibration of spherical integrators. *SPIE,* **1,109,** 114–121.

Meindl, E.A., and G.D. Hamilton, 1992: Programs of the National Data Buoy Center, *Bull. Am. Meteor. Soc.,* **73,** 985–993.

Morel, A., 1980: In-water and remote measurments of ocean color. *Bound.-Layer Meteorol.,* **18,** 177–201.

National Oceanic and Atmospheric Administration (NOAA), 1990: *NDBC Data Availability Summary,* 1801-24-02 Rev. E, U.S. Dept. of Commerce, National Data Buoy Center, Stennis Space Center, 88 pp.

National Research Council, 1990: *TOGA, A Review of Progress and Future Opportunities.* National Academy Press, Washington, D.C., 66 pp.

National Space Science Data Center, 1993: NODIS (NSSDC's On-line Data and Information Service) [database on-line] Master Directory [cited July 1993] Data Set Information Search; identifier: Multiple Key Word Search—TOMS section.

Neckel, H., and D. Labs, 1984: The solar radiation between 3300 and 12500 Å. *Sol. Phys.,* **90,** 205–258.

Olsen, L.M., and C.R. McClain, 1992: Cooperative efforts in support of ocean research through NASA's Climate Data System. *Proc. Eighth Intl. Conf. Interactive Information Processing Systems for Meteorol., Oceanogr. and Hydrol.,* Am. Meteorol. Soc., Atlanta, Georgia, 206–211.

Pagano, T.S., and R.M. Durham, 1993: Moderate resolution imaging spectroradiometer (MODIS). *Proc. SPIE,* **1,939,** 2–17.

Slater, P.N., and J.M. Palmer, 1991: Solar-diffuser panel and ratioing radiometer approach to satellite sensor on-board calibration. *Proc. SPIE,* **1,493,** 100–105.

Stackpole, J.D., 1990: GRIB and BUFR: The only codes you will ever need. *Sixth Intl. Conf. on Interactive Information and Processing Systems for Meteorol., Oceanogr., and Hydrol.,* Am. Meteorol. Soc., Anaheim, California, 23–30.

Trenberth, K.E., W.G. Large, and J.G. Olson, 1990: The mean annual cycle in global ocean wind stress. *J. Phys. Ocean ogr.,* **20,** 1,742–1,760.

University of Illinois at Urbana-Champaign, 1989: *NCSA HDF Specification,* 43 pp.

——, 1993: *NCSA HDF Calling Interfaces and Utilities, Version 3.2,* 121 pp.

Walker, J.H., C.L. Cromer, and J.T. McLean, 1991: A technique for Improving the calibration of large-area sphere sources. *SPIE Vol. 1,493, Calibration of Passive Remote Optical and Microwave Instrumentation,* 224–230.

Weller, M. and U. Leiterer, 1988: Experimental data on spectral aerosol optical thickness and its global distribution. *Beitr. Phys. Atmosph.,* **61,** 1–9.

Woodward, R.H., J. Firestone, and C.R. McClain, 1992: Prog ress report on AVHRR/Pathfinder activities. Internal document submitted to Pathfinder Project, NASA Goddard Space Flight Center, Greenbelt, Maryland, 14 pp.

Zalewski, E.F., and C.R. Duda, 1983: Silicon photodiode device with 100% external quantum efficiency. *Appl. Opt.,* **22,** 2,867–2,873.

The SeaWiFS Technical Report Series

<u>Vol. 1</u>

Hooker, S.B., W.E. Esaias, G.C. Feldman, W.W. Gregg, and C.R. McClain, 1992: An Overview of SeaWiFS and Ocean Color. *NASA Tech. Memo. 104566, Vol. 1,* S.B. Hooker and E.R. Firestone, Eds., NASA Goddard Space Flight Center, Greenbelt, Maryland, 24 pp., plus color plates.

<u>Vol. 2</u>

Gregg, W.W., 1992: Analysis of Orbit Selection for SeaWiFS: Ascending vs. Descending Node. *NASA Tech. Memo. 104566, Vol. 2,* S.B. Hooker and E.R. Firestone, Eds., NASA Goddard Space Flight Center, Greenbelt, Maryland, 16 pp.

Vol. 3

McClain, C.R., W.E. Esaias, W. Barnes, B. Guenther, D. Endres, S. Hooker, G. Mitchell, and R. Barnes, 1992: Calibration and Validation Plan for SeaWiFS. *NASA Tech. Memo. 104566, Vol. 3,* S.B. Hooker and E.R. Firestone, Eds., NASA Goddard Space Flight Center, Greenbelt, Maryland, 41 pp.

Vol. 4

McClain, C.R., E. Yeh, and G. Fu, 1992: An Analysis of GAC Sampling Algorithms: A Case Study. *NASA Tech. Memo. 104566, Vol. 4,* S.B. Hooker and E.R. Firestone, Eds., NASA Goddard Space Flight Center, Greenbelt, Maryland, 22 pp., plus color plates.

Vol. 5

Mueller, J.L., and R.W. Austin, 1992: Ocean Optics Protocols. *NASA Tech. Memo. 104566, Vol. 5,* S.B. Hooker and E.R. Firestone, Eds., NASA Goddard Space Flight Center, Greenbelt, Maryland, 43 pp.

Vol. 6

Firestone, E.R., and S.B. Hooker, 1992: SeaWiFS Technical Report Series Summary Index: Volumes 1–5. *NASA Tech. Memo. 104566, Vol. 6,* S.B. Hooker and E.R. Firestone, Eds., NASA Goddard Space Flight Center, Greenbelt, Maryland, 9 pp.

Vol. 7

Darzi, M., 1992: Cloud Screening for Polar Orbiting Visible and IR Satellite Sensors. *NASA Tech. Memo. 104566, Vol. 7,* S.B. Hooker and E.R. Firestone, Eds., NASA Goddard Space Flight Center, Greenbelt, Maryland, 7 pp.

Vol. 8

Hooker, S.B., W.E. Esaias, and L.A. Rexrode, 1993: Proceedings of the First SeaWiFS Science Team Meeting. *NASA Tech. Memo. 104566, Vol. 8,* S.B. Hooker and E.R. Firestone, Eds., NASA Goddard Space Flight Center, Greenbelt, Maryland, 61 pp.

Vol. 9

Gregg, W.W., F.C. Chen, A.L. Mezaache, J.D. Chen, J.A. Whiting, 1993: The Simulated SeaWiFS Data Set, Version 1. *NASA Tech. Memo. 104566, Vol. 9,* S.B. Hooker and E.R. Firestone, and A.W. Indest, Eds., NASA Goddard Space Flight Center, Greenbelt, Maryland, 17 pp.

Vol. 10

Woodward, R.H., R.A. Barnes, C.R. McClain, W.E. Esaias, W.L. Barnes, and A.T. Mecherikunnel, 1993: Modeling of the SeaWiFS Solar and Lunar Observations. *NASA Tech. Memo. 104566, Vol. 10,* S.B. Hooker and E.R. Firestone, Eds., NASA Goddard Space Flight Center, Greenbelt, Maryland, 26 pp.

Vol. 11

Patt, F.S., C.M. Hoisington, W.W. Gregg, and P.L. Coronado, 1993: Analysis of Selected Orbit Propagation Models for the SeaWiFS Mission. *NASA Tech. Memo. 104566, Vol. 11,* S.B. Hooker, E.R. Firestone, and A.W. Indest, Eds., NASA Goddard Space Flight Center, Greenbelt, Maryland, 16 pp.

Vol. 12

Firestone, E.R., and S.B. Hooker, 1993: SeaWiFS Technical Report Series Summary Index: Volumes 1–11. *NASA Tech. Memo. 104566, Vol. 12,* S.B. Hooker and E.R. Firestone, Eds., NASA Goddard Space Flight Center, Greenbelt, Maryland, 28 pp.

Vol. 13

McClain, C.R., K.R. Arrigo, J. Comiso, R. Fraser, M. Darzi, J.K. Firestone, B. Schieber, E-n. Yeh, and C.W. Sullivan, 1994: Case Studies for SeaWiFS Calibration and Validation, Part 1. *NASA Tech. Memo. 104566, Vol. 13,* S.B. Hooker and E.R. Firestone, Eds., NASA Goddard Space Flight Center, Greenbelt, Maryland, 52 pp., plus color plates.

Vol. 14

Mueller, J.L., 1993: The First SeaWiFS Intercalibration Round-Robin Experiment, SIRREX-1, July 1992. *NASA Tech. Memo. 104566, Vol. 14,* S.B. Hooker and E.R. Firestone, Eds., NASA Goddard Space Flight Center, Greenbelt, Maryland, 60 pp.

Vol. 15

Gregg, W.W., F.S. Patt, R.H. Woodward, 1994: The Simulated SeaWiFS Data Set, Version 2. *NASA Tech. Memo. 104566, Vol. 15,* S.B. Hooker and E.R. Firestone, Eds., NASA Goddard Space Flight Center, Greenbelt, Maryland, 42 pp., plus color plates.

Vol. 16

Mueller, J.L., B.C. Johnson, C.L. Cromer, J.W. Cooper, J.T. McLean, S.B. Hooker, and T.L. Westphal, 1994: The Second SeaWiFS Intercalibration Round-Robin Experiment, SIRREX-2, June 1993. *NASA Tech. Memo. 104566, Vol. 16,* S.B. Hooker and E.R. Firestone, Eds., NASA Goddard Space Flight Center, Greenbelt, Maryland, 121 pp.

Vol. 17

Abbott, M.R., O.B. Brown, H.R. Gordon, K.L. Carder, R.E. Evans, F.E. Muller-Karger, and W.E. Esaias, 1994: Ocean color in the 21st century: a strategy for a 20-year time series. *NASA Tech. Memo. 104566, Vol. 17,* S.B. Hooker and E.R. Firestone, Eds., NASA Goddard Space Flight Center, Greenbelt, Maryland, 20 pp.

Vol. 18

Firestone, E.R., and S.B. Hooker, 1994: SeaWiFS Technical Report Series Summary Index: Volumes 1–17. *NASA Tech. Memo. 104566, Vol. 18,* S.B. Hooker and E.R. Firestone, Eds., NASA Goddard Space Flight Center, Greenbelt, Maryland, (in press).

Vol. 19

McClain, C.R., R.S. Fraser, J.T. McLean, M. Darzi, J.K. Firestone, F.S. Patt, B.D. Schieber, R.H. Woodward, E-n. Yeh, S. Mattoo, S.F. Biggar, P.N. Slater, K.J. Thome, A.W. Holmes, R.A. Barnes, and K.J. Voss, 1994: Case Studies for SeaWiFS Calibration and Validation, Part 2. *NASA Tech. Memo. 104566, Vol. 19,* S.B. Hooker, E.R. Firestone, and J.G. Acker, Eds., NASA Goddard Space Flight Center, Greenbelt, Maryland, 73 pp.

REPORT DOCUMENTATION PAGE

Form Approved
OMB No. 0704-0188

Public reporting burden for this collection of information is estimated to average 1 hour per response, including the time for reviewing instructions, searching existing data sources, gathering and maintaining the data needed, and completing and reviewing the collection of information. Send comments regarding this burden estimate or any other aspect of this collection of information, including suggestions for reducing this burden, to Washington Headquarters Services, Directorate for Information Operations and Reports, 1215 Jefferson Davis Highway, Suite 1204, Arlington, VA 22202-4302, and to the Office of Management and Budget, Paperwork Reduction Project (0704-0188), Washington, DC 20503.

1. AGENCY USE ONLY *(Leave blank)*

2. REPORT DATE
August 1994

3. REPORT TYPE AND DATES COVERED
Technical Memorandum

4. TITLE AND SUBTITLE
SeaWiFS Technical Report Series
Volume 19—Case Studies for SeaWiFS Calibration and Validation, Part 2

5. FUNDING NUMBERS
970.2

6. AUTHOR(S) C.R. Mc Clain, R.S. Faser, J.T. McLean, M. Darzi, J. K. Firestone, F.S. Patt, B.R. Schieber, R. H. Woodward, E-n Yeh, S. Mattoo, S. F. Biggar, P.N. Slater, K. J. Thome, A.W. Holmes, R. A. Barnes and K.J. Voss
Technical Editors: Stanford B. Hooker, Elaine R. Firestone and James G. Acker

7. PERFORMING ORGANIZATION NAME(S) AND ADDRESS(ES)
Laboratory for Hydrospheric Processes
Goddard Space Flight Center
Greenbelt, Maryland 20771

8. PERFORMING ORGANIZATION REPORT NUMBER
94B00115

9. SPONSORING/MONITORING AGENCY NAME(S) AND ADDRESS(ES)
National Aeronautics and Space Administration
Washington, D.C. 20546-0001

10. SPONSORING/MONITORING AGENCY REPORT NUMBER
TM-104566, Vol. 19

11. SUPPLEMENTARY NOTES
M. Darzi, E.R.Firestone, J.K. Firestone, F.S. Patt, B.D. Schieber, R.H. Woodward, and E-n. Yeh: General Sciences Corporation, Laurel, MD; S. Mattoo: Applied Research Corporation, Landover, MD; S.F. Biggar, P.N. Slater, and K.J. Thome: University of Arizona, Tucson, AZ; A.W. Holmes: Santa Barbara Research Center, Goleta, CA; R.A. Barnes: ManTech Environmental Technology, Inc.; Wallops Island, VA; K.L. Voss: University of Miami, Coral Gables, FL and J.G. Acker: Hughes STX, Lanham, MD

12a. DISTRIBUTION/AVAILABILITY STATEMENT
Unclassified–Unlimited
Subject Category 48
Report is available from the NASA Center for AeroSpace Information, 800 Elkridge Landing Road, Linthicum Heights, MD 21090; (301) 621-0390.

12b. DISTRIBUTION CODE

13. ABSTRACT *(Maximum 200 words)*

This document provides brief reports, or case studies, on a number of investigations and data set development activities sponsored by the Calibration and Validation Team (CVT) within the Sea-viewing Wide Field-of-view Sensor (SeaWiFS) Project. Chapter 1 is a comparison of the atmospheric correction of Coastal Zone Color Scanner (CZCS) data using two independent radiative transfer formulations. Chapter 2 is a study on lunar reflectance at the SeaWiFS wavelengths which was useful in establishing the SeaWiFS lunar gain. Chapter 3 reports the results of the first ground-based solar calibration of the SeaWiFS instrument. The experiment was repeated in the fall of 1993 after the instrument was modified to reduce stray light; the results from the second experiment will be provided in the next case studies volume. Chapter 4 is a laboratory experiment using trap dectectors which may be useful tools in the calibration round-robin program. Chapter 5 is the original data format evaluation study conducted in 1992 which outlines the technical criteria used in considering three candidate formats, the Hierarchical Data Format (HDF), the Common Data Format (CDF) and the network CDF (netCDF). Chapter 6 summarizes the meteorological data sets accumulated during the first three years of CZCS operation which are being used for initial testing of the operational SeaWiFS algorithms and systems and would be used during a second global processing of the CZCS data set. Chapter 7 describes how near-real time surface meteorological and total ozone data required for the atmospheric correction algorithm will be retrieved and processed. Finally, Chapter 8 is a comparison of surface wind products from various operational meteorological centers and field observations. Surface winds are used in the atmospheric correction scheme to estimate glint and foam radiances.

14. SUBJECT TERMS
SeaWiFS, Oceanography, Calibration, Validation, CZCS, Atmospheric Correction, Radiative Transfer, Lunar Reflectance, Stray Light, Round-Robin, Hierarchical Data Format, HDF, Common Data Format, CDF, netCDF, Operational SeaWiFS Algorithms, Surface Wind Products, Glint, Foam Radiances

15. NUMBER OF PAGES
73

16. PRICE CODE

17. SECURITY CLASSIFICATION OF REPORT	18. SECURITY CLASSIFICATION OF THIS PAGE	19. SECURITY CLASSIFICATION OF ABSTRACT	20. LIMITATION OF ABSTRACT
Unclassified	Unclassified	Unclassified	Unlimited